Sandstone Uranium Deposits of Nebraska and Colorado: A Comparative Study

by

Angela S. Meek

A Thesis submitted to the Faculty of Graduate Studies of the

University of Manitoba

in partial fulfillment of the requirements of the degree of

MASTER OF SCIENCE

Department of Geological Sciences

University of Manitoba

Winnipeg, Manitoba

Abstract

Sandstone-type uranium deposits are among the most economic sources of uranium. Despite their significance, the tabular deposits on the Colorado Plateau and roll-front deposits in Nebraska have not been studied adequately. There are important differences between the tabular Colorado Plateau and Nebraska roll-front deposits, including their ore mineralogy, distribution and habit of ore-bodies, alteration, and mechanisms of ore deposition. The U-Pb ages of uranium minerals from the Colorado deposits indicate four stages of mineralization, spanning from the early Oligocene to late Pliocene. Uranium and V minerals include coffinite, montroseite and carnotite and are associated with both biogenic and non-biogenically precipitated sulphides. Two generations of coffinite mineralization from the Three Crow roll-front deposit in Nebraska were identified. This mineralization precipitated during the early Pliocene and late Miocene. The U-Th activity ratios of U minerals suggest a net accumulation of uranium within the limbs of the roll-front. Evolving oxidation fronts are implied by multiple sulphide generations as indicated by their $\delta^{34}S$ compositions.

Acknowledgments

Firstly I would like to thank my advisor Dr. Mostafa Fayek for his guidance, valuable time and shared expertise throughout the last four years.

I wish to thank the Cameco Corporation for the opportunity and support to work on this project. A special thanks to the Cotter Corporation for their cooperation and access to their sites.

I wish to thank Dr. Ravi Sidhu for her time, patience and assistance in the operation of the EMPA.

Lastly, I would like to thank my wonderful husband Dave, and two beautiful children Ellica and Dawson for their unending patience and understanding. A very special thanks to my mother for her encouragement and support, for without her, I would not have been able to accomplish all I have today.

Table of Contents

Abstract ..... **i**

Acknowledgements ..... **ii**

Table of Contents ..... **iii**

List of Tables ..... **v**

List of Figures ..... **v**

Chapter 1: Introduction **1**

1.1 Tabular Deposits 2
1.1.2 The role of organic matter in the genesis of tabular deposits 4
1.1.3 The role of sulphur and sulphate-reducing bacteria 5
1.2 Roll-Front Deposits of Nebraska and Wyoming 6
1.2.1 Chemical and biogenic models: the role of organic matter, bacteria and sulphides 8
1.3 Objectives 12

Chapter 2: Geological Considerations **13**

2.1 Regional Geology: Central and Southwestern Colorado 13
2.1.2 The Morrison Formation 14
2.2 Local Geology: Uravan, Colorado 15
2.3 Regional Geology: Northwestern Nebraska 19
2.4 Local Geology: Dawes County, Nebraska 24

Chapter 3: Methods **26**

3.1 Sample Selection 26
3.1.1 Colorado sample suite 26
3.1.2 Nebraska sample suite 26
3.2 Methodology 27
3.2.1 Scanning electron microscope (SEM) 27
3.2.2 Electron microprobe (EMP) 27
3.2.2.1 Chemical Pb ages 28
3.2.3 Secondary ion mass spectrometer 28
3.2.3.1 Standards 29
3.2.3.2 Sulphur isotope analysis 30
3.2.3.3 U-Pb isotopic analysis 30

Chapter 4: Results **32**

4.1 Colorado Tabular Uranium Deposits 32
4.1.1 Hand sample descriptions 32
4.1.2 Petrography 33
4.1.2.1 Mineral paragenesis 34
4.1.2.2 Uranium minerals 36
4.1.2.3 Vanadium minerals 41
4.1.2.4 Sulphide minerals 44
4.1.3 Chemical Pb ages 45
4.1.4 U-Th-Pb geochronology 46
4.1.5 Sulphur isotopic analysis of pyrite 47
4.2 Three Crow Roll-Front Uranium Deposit, Nebraska 48
4.2.1 Hand sample descriptions 48
4.2.2 Petrography 49
4.2.2.1 Mineral paragenesis 50
4.2.2.2 Uranium mineralization 51
4.2.2.3 Sulphide and iron oxide minerals 55
4.2.3 Chemical Pb ages and U-Th-Pb geochronology 57
4.2.4 Stable isotopes 58

Chapter 5: Discussion **60**

5.1 Colorado Tabular Uranium-Vanadium Deposits 60
5.1.2 Primary and secondary ore minerals 60
5.1.3 Ages of uranium mineralization 62
5.1.4 Sulphur isotopic analysis 64
5.2 Three Crow Roll-Front, Nebraska 65
5.2.1 Ages of coffinite mineralization 66
5.2.3 Sulphur isotopic analysis 67
5.2.3.1 Biogenic sulphur reduction 67

Chapter 6: Conclusions **74**

References **78**

Appendix A: Hand Sample Descriptions **85**
Appendix B: Thin Section Descriptions **99**
Appendix C: Electron Microprobe Analyses **122**
Appendix D: Secondary Ion Mass Spectrometer Analyses **129**

List of Tables

Table 2-1: Chemical formulae of uranium and vanadium minerals reported within the Uravan mineral belt 19

Table 4-1: Partial EMP analysis of vanadium clays 44

List of Figures

Figure 1-1: Idealized vertical cross-section of a roll-front uranium deposit 8

Figure 2-1: Stratigraphic column showing major units present in southwestern Colorado region 14

Figure 2-2: Map of southwestern Colorado and southeastern Utah showing location of Uravan Mineral Belt ..... 17.

Figure 2-3: Stratigraphic cross-section of units present in Slick Rock district of Uravan Mineral Belt, Colorado 18

Figure 2-4: Photo of tabular sediment-hosted JD-6 uranium-vanadium deposit in underground workings 18

Figure 2-5: Map showing extents of the Crawford sub-basin and major structural features of the Crow Butte deposit and Three Crow study area in Nebraska 22

Figure 2-6: Age, stratigraphy, major lithologies, and depositional environment of the Crawford sub-basin, Nebraska 23

Figure 2-7: Revised lithostratigraphic cross-section of the White River Group 24

Figure 2-8: Photograph of drill cuttings from drill hole T797C 25

Figure 4-1: Paragenetic scheme illustrating the genetic sequence of minerals associated with the Colorado deposits 35

Figure 4-2: BSE images of uranium minerals from Colorado deposits 39

Figure 4-3: BSE images of vanadium and V-clay minerals from Colorado deposits 43

Figure 4-4: Reflected light images of the three morphological types of pyrite analysed by SIMS 45

Figure 4-5: Disequilibrium plot showing effects of rock-water interactions for uranium mineral phases 47

Figure 4-6: Images of important textural features from Three Crow deposit 50

Figure 4-7: Paragenetic scheme associated with Three Crow deposit..... 51

Figure 4-8: BSE images of coffinite mineralization from Three Crow deposit 53

Figure 4-9: Element distribution map of coffinite mineralization from Three Crow deposit..... 53

Figure 4-10: BSE images of coffinite and pyrite mineralization from Three Crow deposit..... 54

Figure 4-11: Element distribution map of coffinite and pyrite mineralization from Three Crow deposit..... 54

Figure 4-12: Reflected light and BSE images of pyrite morphologies from Three Crow deposit..... 56

Figure 4-13: Disequilibrium plot of uranium minerals from Three Crow deposit 58

Figure 5-1: Isotopic sulphur trend of quantitative reconstitution model 71

Figure 5-2: Isotopic sulphur trend of steady state model..... 72

Figure 5-3: Isotopic sulphur trend of pyrite from Three Crow deposit 72

Figure 5-4: $\delta^{34}S$ composition of sulphides across Three Crow roll-front deposit 73

Chapter 1. Introduction

The world's major uranium deposits occur in several distinctly different geological environments. Fifteen principal types of uranium deposits are recognized and more than 40 subtypes and classes can be attributed to the 15 types (Dahlkamp, 1993; Fayek and Kyser, 1999). Sandstone-hosted uranium deposits are widespread and are primarily hosted in Carboniferous to Tertiary age rocks, and constitute approximately 30% of the world's uranium resources (Kyser and Cuney, 2009). They can be broadly defined as low-temperature, epigenetic deposits that likely derive their uranium supply from adjacent, exposed granitic bodies and interbedded or overlying uraniferous tuffaceous sediments (Finch, 1996; Kyser and Cuney, 2009). There are four sub-types:

(a) Tabular deposits consist of ore-zones that form irregularly shaped lenticular masses in reduced sediments (IAEA, 2009). The mineralized zones are largely sub-parallel to bedding and parallel to the paleo-drainage direction. These deposits are generally underlain by evaporite deposits and overlain by mudstone (Goldhaber et al., 1990; Northrop et al, 1990a,b; Sanford, 1994);

(b) Roll-front deposits are characterized by convex ore zones that form down-stream from the hydraulic gradient. Overlying volcanic ash associated with these deposits is a possible source of the uranium (e.g., Moynkum, Inkay and Mynkuduk in Kazakhstan; Crow Butte and Smith Ranch in the U.S.A;

(c) Basal channel deposits form in paleo-drainage systems filled with permeable alluvial-fluvial sediments capped by basalt sheets. Uranium minerals are associated with detrital plant debris and form elongate or ribbon-like ore bodies (e.g., Khiagdinskoye in the Russian Federation).

(d) Tectonic/lithologic deposits form in permeable sandstone areas where uranium is precipitated in open tectonic extensional zones (e.g., Mas Lavayre in France and Mikouloungou in Gabon (IAEA, 2009).

The two highest grade and producing ore types are classified as tabular and roll-front; they are recognized on the basis of the shape of the ore body, and the relationship of the ore bodies to depositional and structural environments.

Historically, the most economic sources and reserves of U in the United States occur in sandstone deposits of two types, the Wyoming-Nebraska roll-front type and the Colorado Plateau peneconcordant (tabular) type deposits. Although the geology and geochemical processes involved in the genesis of these types of U deposits have been described in numerous studies (e.g., Fischer, 1970; Thamm et al., 1981; Goldhaber et al., 1990; Northrop et al., 1990a,b; Sanford, 1994), these deposits have been largely ignored in the past 15 years. The major similarities and differences between these two deposit types and some of the genetic problems relating to these differences have been examined; however, due to the fine-grained nature of mineralization, understanding the key processes involved in the genesis and subsequent alteration of these deposits has been challenging.

1.1 Tabular Deposits

The tabular vanadium-uranium deposits of the Colorado Plateau have been studied in detail since the mid-1950's, and much knowledge has been gained with respect to the genesis and geology of this deposit type (e.g. Wright, 1955; Gruner, 1956;

Granger, 1976; Ludwig, 1978; Thamm et al., 1981; Tyler and Ethridge, 1983; Goldhaber et al., 1987; Goldhaber et al., 1990; Northrop et al.,1990a,b; Finch, 1996; Spirakis, 1996; Cuney, 2009). The majority of deposits occur in fluvial sandstones of the Salt Wash Member of the Jurassic Morrison Formation, and the primary ore is composed of V-clays and low-valent vanadium silicates and oxides, with U minerals accessories. Salt Wash ore bodies typically trend parallel to large-scale sedimentary features, and occur as irregular lenses of originally horizontal, tabular ore layers, ranging in thickness from a few centimeters to several feet. They occur entirely within reduced sediments without adjacent tongues of oxidized sandstone, and are almost universally spatially associated with detrital organic matter. Coffinite [$U(SiO_4)_{0.9}(OH)_{0.4}$] and uraninite [UO_2] are the primary uranium ore minerals throughout the Salt Wash Member sediments of the Plateau. A density-stratified fluid interface is a favoured concept for the genesis of tabular-type deposits of the Colorado Plateau (Nash et al., 1981; Northrop et al., 1990a; Sanford, 1992, 1994). The saline-brine model involves the interaction of dense, saline groundwater chemically derived in part from the underlying evaporite facies, with the down-dip flow of fresh groundwater containing dissolved U. The precipitation of V-clays within host sediments had significant influence on the pH of the brine by removing hydroxide ions from solution; uranyl carbonate complexes carried by meteoric water were destabilized by the significant drop in pH, which was followed by uranium adsorption onto mineral surfaces (e.g., quartz), reduction by biogenic H_2S, and finally precipitation of coffinite (in the presence of sufficient dissolved silica) or uraninite (Goldhaber et al., 1987).

1.1.2 The role of organic matter in the genesis of tabular deposits

Most genetic brine-meteoric models for tabular deposits suggest a spatial relationship between detrital organic matter and mineralized layers. However, the absolute role of organic carbon in the deposition of uranium ores remains controversial. For example, in a comprehensive study of tabular deposits in the Henry Basin, Utah, Northrop et al. (1990a) determined that while the formation of uranium deposits is dependent on the presence of organic material, there is no direct correlation between organic carbon and the abundance of uranium. The brine-meteoric interface model described by Northrop et al. (1990a,b) suggests that uranium minerals precipitated as a result of bacteria-mediated reactions, and that detrital organic material served as an adsorbent and energy source for the bacteria. While amorphous (non-cellular) organic matter is characteristic of the tabular deposits of Grant's Region in the southern Plateau, it is virtually lacking from deposits in the northern Plateau. Hansley and Spirakis (1992) and Spirakis (1996) argue that amorphous organic matter is essential to the genesis of all tabular deposits, functioning as a reductant (with bacteria acting as a catalyst). They suggest that in those deposits where amorphous organic matter is presently poor, lacking, or bears weak spatial relationship to mineralized intervals, it is simply a reflection of the degree of post-ore diagenesis. Organic materials are transformed into humic acids during diagenesis, and are responsible for the alteration of Fe-Ti oxides magnetite and ilmenite. Etched and skeletal Fe-Ti oxides are characteristic of many tabular deposits across the Plateau and have been recognized as the most probable source of vanadium in the tabular deposits (Shawe, 1976; Goldhaber et al., 1990; Hansley and Spirakis, 1992; Spirakis, 1996).

1.1.3 The role of sulphur and sulphate-reducing bacteria

An early study by Jensen (1958) that included sulphur isotope data from tabular uranium deposits in Utah, found that no relationship exists between $\delta^{34}S$ values and sulphide species, ore potential (mineralized versus unmineralized), or presence of organic matter. Northrop et al. (1990a), however, measured the $\delta^{34}S$ values of sulphides from the Henry Basin, Utah, and plotted $\delta^{34}S_{sulphide}$ versus depth; the data revealed significant variation in $\delta^{34}S$ values between mineralized and unmineralized samples. Unmineralized samples average 12.1 ‰, while mineralized samples average -39.6 ‰. Experimental studies (e.g., Mohagheghi et al., 1984) have demonstrated that fluids containing sulphate-reducing bacteria are more efficient at removing uranium from solution than bacteria-free solutions. They suggested that certain bacteria may take up the uranium in cell walls to await a suitable reducing agent such as H_2S or H_2. According to Reynolds and Goldhaber (1983), bacterial sulphate reduction may serve to maintain a relatively high pH, ranging from 6.5 to 8.4. Experimental results have shown that bacteria-mediated processes not only catalyze the redox reactions (Mohagheghi et al., 1984; Johnston et al., 2007; Zerkle et al., 2009), but may reduce U^{6+} independently from organic matter and sulphides present (Lovley and Phillips, 1992; Spirakis, 1996). Experimental studies of the isotope effects of sulphur-utilizing bacteria (e.g., Farquhar et al., 2003; Brunner and Bernasconi, 2005; Johnston et al., 2008; Zerkle et al, 2009), show that cyclical fractionation of S during the dissimilatory reduction of sulphate results in the depletion of ^{34}S characteristic of biologically reduced sulphides.

The source of uranium for the sediment-hosted uranium deposits of the Colorado Plateau remains speculative, but is assumed to have been tuffaceous material within the

Salt Wash Member, or the Brushy Basin shales overlying the Salt Wash Member (Thamm et al., 1981).

Due to their genetic association with the large, economic tabular deposits of the Uravan mineral belt and Henry basin, V-clays of the Jurassic sediments throughout the Colorado Plateau have been studied in detail by Northrop et al. (1990b) and Meunier (1994). The principal vanadium clay minerals in the upper Morrison Formation are V-bearing chlorite and illite, and although the origin and diagenetic history of vanadium clays are poorly understood, these minerals are likely the product of vanadium introduction into detrital clays (Meunier, 1994). The source of vanadium is still uncertain; however, some workers have suggested that this element is derived from the decomposition of detrital magnetite and ilmenite, or leached from the overlying Cretaceous sediments (Thamm et al., 1981; Meunier, 1994).

1.2 Roll-Front Deposits of Nebraska and Wyoming

In Nebraska, which has been described as "one of the most overlooked uranium provinces in the U.S." (Sibray, 2010), the Crow Butte deposit in Dawes County is the first and only operating uranium mine, producing over 13 million pounds U_3O_8 since 1991 using in-situ recovery technology. Since the Crow Butte deposit shows similar physical and chemical characteristics to the Wyoming-type roll-fronts, it is also considered to share a similar genetic history. The Wyoming roll-front deposits constitute the second largest uranium resource in the U.S., and have been geologically and chemically characterized in several studies (e.g., Harshman, 1966, 1972; Warren, 1972;

Dooley et al., 1974; Granger and Warren, 1978; Ludwig, 1978; Leventhal and Santos, 1981; Reynolds and Goldhaber, 1983). The Wyoming roll-fronts occur in fluvial and alluvial-fan deposits, where late Eocene tectonism created a structurally and topographically favourable drainage system for active meteoric recharge. Basin burial followed by uplift during the Oligocene and Miocene resulted in aquifer recharge with mineralized fluids, resulting in the formation of the majority of ore deposits (Hobday and Galloway, 1999). Typical roll-front ore bodies are roughly crescent-shaped in cross section, concave towards the altered tongue. Uranium minerals occur along a redox interface and precipitate where uranium-rich groundwater percolating down gradient through the aquifer encounters sediments containing reduced constituents. Ore zones can be described as long, sinuous bands oriented perpendicular to groundwater flow (Figure 1-1); on the oxidized, up-gradient side the contact is relatively sharp, whereas the reduced, down-gradient side has diffuse boundaries. Ferric iron minerals such as hematite, goethite and other iron oxides typically occur within the altered zone, while pyrite, minor marcasite and variable amounts of organic matter occur in the unoxidized (reduced) zone. Sedimentary controls in the formation of deposits include: 1) the endurance of gently dipping, continuous strata during basin uplift and presence of clay interbeds that form confined aquifers allowing for slow percolation of groundwater and a sustainable reducing environment; 2) the sporadic deposition and rapid burial of organic matter, followed by periods of high water tables thus maintaining an anaerobic environment; 3) the formation of H_2S and pyrite by sulphate-reducing bacteria using organic matter as an energy source. Oxygen content of mineralized fluids and the reducing capacity of host sediments is also a major ore control; uranium precipitation

from ore fluids is directly influenced by a drop in Eh following the formation of significant amounts of reducing, metastable sulphur compounds from the breakdown of host rock sulphide minerals in the presence of free oxygen within percolating fluids (Granger and Warren, 1979).

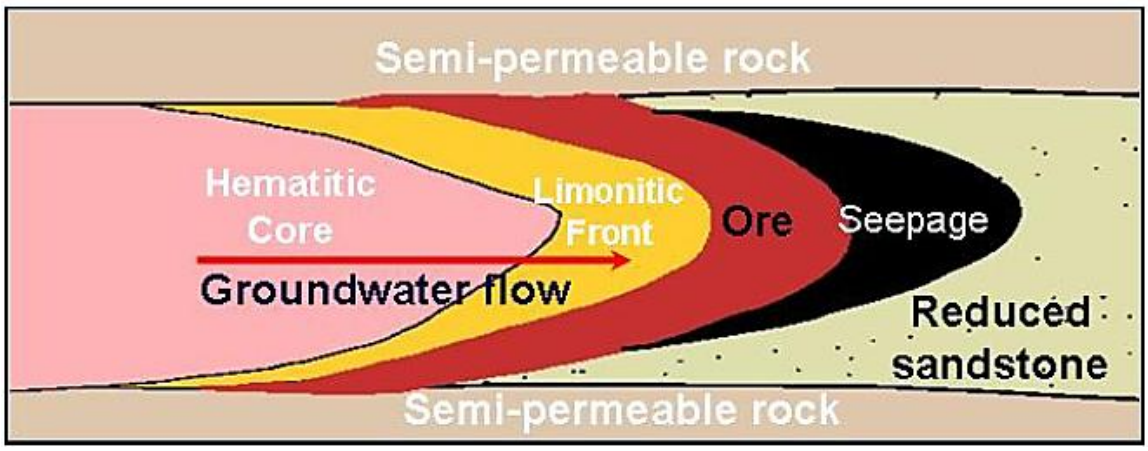

Figure 1-1: Idealized vertical cross-section of a roll-front uranium deposit (from Hanly et al., 2009).

1.2.1 Chemical and biogenic models: the role of organic matter, bacteria and sulphides

Studies of Wyoming-type deposits have shown that, as in tabular deposits, there is no direct chemical correlation between uranium and organic matter (eg., Leventhal and Santos, 1981; Spirakis et al., 1984). An early study by Jenson (1958) of the Powder River and Shirley Basin roll-front deposits in Wyoming suggested that the presence of uranium in an area lacking organic matter could be explained simply by H_2S migration from a locale with an organic food supply used by anaerobic bacteria. Alternatively, the lack of organic matter in mineralized zones may simply reflect the oxidizing nature of the ore fluids (Harshman, 1966). Organic carbon is not considered an essential component in the development of roll-front deposits by many workers, instead organic matter may 1)

act as an energy source for sulphate-reducing bacteria, 2) reduce dissolved sulphate (catalyzed by bacteria) and 3) contribute to oxygen consumption from migrating fluids (Leventhal and Santos, 1981; Reynolds and Goldhaber, 1983; Gjelsteen and Collings, 1988; Spirakis, 1996). According to the chemical genetic model, in deposits lacking organic matter (relatively) large quantities of pre-ore pyrite would need to be oxidized by migrating fluids in order to consume sufficient oxygen to create a redox front (Granger and Warren, 1979). Both chemical and biogenic models for the genesis of roll-front deposits are well described in theoretical terms throughout the literature (e.g., Jensen, 1958; Warren and Granger, 1969; Warren, 1972; Granger and Warren, 1979; Reynolds and Goldhaber, 1983). Amongst other geochemical parameters, both models depend on the uniform distribution of pre-ore iron-sulphide minerals in host sediments, as well as the formation of ore-stage pyrite in the down-gradient, altered zone of the deposit during mineralization. The biogenic model states that groundwater flows down dip through the ore zone, oxidizing pre-existing (pre-ore) iron-sulphides and producing soluble sulphate and iron species. Anaerobic bacteria, using organic matter as a food source, gain energy as they reduce the sulphate to form H_2S, which is then combined with dissolved iron species to form isotopically light pre-ore pyrite (Warren, 1972). Warren (1972) measured the $\delta^{34}S$ values of pyrite from a Shirley Basin deposit which ranged from -33‰ (ore zone) to +18‰ (down dip of mineralized zone), with ore minerals intimately associated with organic matter. Warren (1972) also plotted the isotopic composition of sulphide sulphur versus distance from the ore zone; he concluded that chemical disproportionation is responsible for the formation of the Shirley Basin deposit, mainly because the isotopic values of pyrite down dip of mineralization (i.e. post-ore) exceeded those of the pre-ore

pyrite. However, Harshmann (1966), Austin (1970) and Reynolds and Goldhaber (1983), reclassified the same deposit as being of biogenic origin based on their interpretations of the distribution of $\delta^{34}S$ values from sulphides across the roll-front. An alternative non-biogenic (or chemical) model for deposits that contain little to nil organic matter is discussed by Granger and Warren (1969) and Warren (1972), which states that bacterial metabolic processes are not necessary during the ore-forming stage of roll-front deposits. These authors maintain that the oxidation of pre-existing iron sulphide minerals that were *initially* formed via bacterial sulphate reduction in the presence of organic matter during slow migration of ore-forming fluids can produce both insoluble and soluble sulphur and iron compounds. The reconstitution of pyrite occurs as the dissolved sulphur and iron species migrate from the oxidized zone, forward into the reducing zone of the roll-front deposit already containing pyrite, where they react and form isotopically light pyrite (relative to the pre-ore pyrite). Depending on the pH, either pyrite (alkaline conditions) or marcasite (slightly acidic) can precipitate. However, Granger and Warren (1978) assert that because sulphate and carbonate ions are not effective redox agents, the concentration of free oxygen in the system is the principal control in the formation of roll-front deposits, regardless of whether the deposit is biogenically or non-biogenically formed. Reynolds and Goldhaber (1983) investigated the link between iron sulphide minerals and roll-front genesis and discovered strong associations between sulphur species, organic matter and pH. They concluded that bacterial sulphate reduction during the formation of roll-fronts in host rocks containing organic matter created conditions of high pH and led to the formation of pyrite, while the low pH in sediments lacking intrinsic organic matter favoured the formation of marcasite. Stanton and Goldhaber

(1991) and Reynolds and Goldhaber (1983) found that no apparent link exists between sulphide species and isotopic sulphur composition.

Element zonation within roll-front deposits has been noted in several studies (e.g., Fischer and Stewart, 1961; Harshmann, 1966, 1972, 1974; Spirakis et al., 1984). During ore-forming processes, the oxidation potential of migrating fluids decreases and specific elements begin to precipitate from solution. Spirakis et al. (1984) observed that V, Pb, Ba, Al, and Gd were enriched in mineralized zones (relative to background rocks), while Ca, Y, Ti, and Zr were found to be depleted. Other studies (e.g., Granger and Warren, 1969, 1979; Fischer, 1970) observed anomalously high concentrations of Se within the ore zone, while Mo and Ca are concentrated in zones up to several hundred metres down dip from the ore zone. The correlation of C and S suggests that sulphides in the ore zone are the result of *in situ* (i.e. epigenetic or syngenetic) sulphate reduction; the covariance of carbon and sulphur does not apply to migrated sulphides (H_2S moving up faults). The published results showed a slight increase of both sulphur and organic carbon; although the increase in sulphur is minor, sulphides are capable of reducing approximately 25 times their weight of uranium (from U^{6+} to U^{4+}) when oxidized to sulphate. The reducing power decreases only to 10 times the weight of uranium if the oxidation of sulphide is incomplete (e.g., sulphide to thiosulphate) (Leventhal and Santos, 1981).

1.3 Objectives

Numerous studies on the tabular deposits of Colorado and the roll-front deposits of Wyoming have characterized their mineralogy and geochemical characteristics (e.g., Wright, 1955; Gruner, 1956; Granger and Warren, 1974; Ludwig, 1978; Warren et al., 1980; Thamm et al., 1981; Tyler and Ethridge, 1983; Goldhaber et al., 1987; Goldhaber et al, 1990; Northrop et al., 1990 (a,b); Finch, 1996; Spirakis, 1996; Cuney, 2009). However, little is known about the Three Crow roll-front deposit in Nebraska, and few studies have been published in the past 15 years on the tabular-type deposits of the Colorado Plateau. In addition, there have been no recent geochronological studies of uranium ore minerals from the Colorado tabular-type deposits, and the age of uranium mineralization in the Three Crow deposit is unknown. Therefore, the main objectives of this thesis are: (1) to characterize and establish a chronology for the uranium ore minerals from both the Nebraska and Colorado deposits, and (2) characterize and compare the ore forming processes by comparing their mineral parageneses and sulphur isotopic composition of the sulphide minerals associated with different zones within these deposits. This type of information can be applied to refine exploration models, which can be used by industry to explore for these types of deposits in similar geological environments.

Chapter 2. Geological Considerations

2.1 Regional Geology: Central- and Southwestern Colorado

The Colorado Plateau is situated within the Western Interior and covers almost 210 000 square kilometers of the Four Corners region, which consists of the southwestern corner of Colorado, northwestern corner of New Mexico, northeastern corner of Arizona and southeastern corner of Utah. The Precambrian basement is composed mainly of metamorphic and granitic complexes, with minor late sedimentary packages. The Colorado Plateau was tectonically stable during most of the Palaeozoic era (Cambrian through Mississippian); however, during the early Pennsylvanian, the plateau was affected by repeated broad upheavals, such as the uplifts of the Ancestral Rocky Mountains in central Colorado, including the Uncompahgre uplift, followed by extreme erosion and deposition of clastic sediments in the complementary basins. By the end of the Permian, the Ancestral Rockies had been eroded to a nearly flat plain. In Late Paleozoic time, the northwest-trending Paradox Basin developed in southwestern Colorado and southeastern Utah where thick accumulations of black shales and evaporites accumulated (Tweto, 1980; Thamm et al, 1981). The Jurassic stratigraphic sequence (Figure 2-1) is represented largely by continental sediments; the highlands of central and southwestern Colorado, such as the Transcontinental Arch and Uncompahgre Uplift, likely had great influence on southern and eastern shorelines of invading seas from the north and south. Marine sedimentation during the Cretaceous was more extensive in the east than in the west; throughout Colorado, facies are localized and often marked by numerous disconformities since sedimentation and subsidence rates differed across the Colorado region (Berman et al., 1980). The major mountain topography

present today has been most influenced by the Laramide orogeny, which occurred from the late Cretaceous through mid-Eocene, creating the basins and uplifts which formed the Central Rocky Mountains. However, many of the exposed structural features are products of the reactivated faults and uplifts that were developed during and since the Precambrian time (Tweto, 1980). Epeirogenic uplift during the Pleistocene led to the erosion of softer sediments and downcutting of river and stream valleys which have attributed to the present-day topography (Chenoweth et al., 1981).

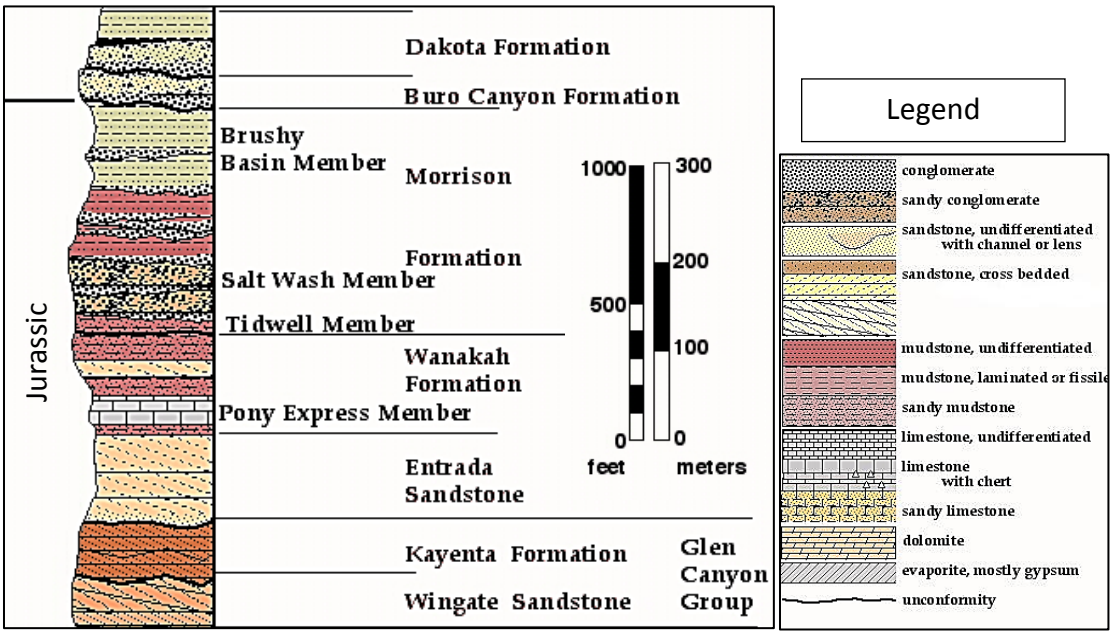

Figure 2-1: Stratigraphic column showing units present in the southwestern Colorado region. All units younger than the Brushy Basin Member of the Morrison Formation were subsequently removed by erosion in the study area. Modified after Blakey (2011).

2.1.2 The Morrison Formation

In western Colorado, the uppermost Jurrassic rocks are represented by the economically important Morrison Formation, which consists of four members: the

Windy Hill, Tidwell, Salt Wash, and the Brushy Basin. In areas of high uranium production in Western Colorado and Eastern Utah (i.e. the Uravan Mineral Belt), the Morrison Formation consists only of the Salt Wash Member and the Brushy Basin Member (Figure 2-1; Thamm et al., 1981). The Salt Wash Member is the principal host to the major U-V deposits throughout the plateau and consists of cross-bedded sandstone facies with interbedded mud- and silt-facies deposited by braided streams in an alluvial fan setting (Thamm et al., 1981; Tyler and Ethridge, 1983; Currie, 1998). Detrital zircons from Salt Wash ash beds were determined to have ages of 151.6 ± 1.1 Ma and 148.5 ± 2.5 Ma (Bradshaw and Kowallis, 2010). The Brushy Basin Member conformably overlies the Salt Wash Member in western Colorado and is composed of three major facies consisting mainly of sandstones, mudstones and minor limestones and they are interpreted to have been deposited in fluvial and alluvial/lacustrine plains (Currie, 1998). Abundant bentonite beds composed of volcanic ashes in the middle part of the Brushy Basin are the most probable source of U in the Salt Wash deposits (Thamm et al., 1981).

2.2 Local Geology: Uravan, Colorado

The SM-18 and Jo Dandy mines are located near Uravan, Montrose County, where the topography is dominated by mesas and deeply incised canyons. A large proportion of uranium deposits in Colorado are concentrated along an arcuate belt called the Uravan Mineral Belt (Figure 2-2). Although large ore bodies are not restricted to this belt, deposits within the Uravan Mineral Belt have been the focus of mining and exploration due to the large size, high grade and close spacing of ore bodies (Fischer and

Hilpert, 1952; Thamm et al, 1981; Tyler and Ethridge, 1983). In the project areas, uranium and vanadium production comes from the upper part of the Salt Wash Member of the Morrison Formation and the highest grade of mineralization occurs in point bar deposits within meandering stream paleo-channels (Tyler and Ethridge, 1983). The deposits are predominantly V deposits and U is considered an accessory element; U-V ratios are approximately 1:5 in the project area, and ratios as high as 1:20 have been reported outside the Belt. The ore deposits in the region follow the north-west trend of the nearby Paradox Basin salt anticlines. Since the formation of the Paradox Valley salt anticlines was concurrent with the deposition of the Salt Wash sediments, these structures likely had a strong influence on channel flow direction and ore concentration (Thamm et al., 1981). Paleocurrent data and sandstone composition indicate a western Cordilleran sediment source for the Salt Wash Member (Currie, 1998).

In the Uravan region, the tabular U-Vore bodies are concordant to bedding and erratic; ore minerals occur within reduced paleo-channel sediments that are proximal and commonly parallel to oxidized sandstones (Figure 2-3; Tyler and Ethridge, 1983). The host sandstones are well consolidated and are characterized by abundant but erratic organic matter and clay interbeds. The reduced sandstones can be identified in hand sample mainly by their colour; sediments are typically shades of light to medium grey, or light brown with limonite spots, depending on the position of the sedimentary bed relative to the water table. Oxidized sediments range in colour from red to rusty brown to pink due to the presence of hematite or limonite that formed in oxidizing conditions during deposition (Thamm et al., 1981). The samples collected from the project areas are host to the primary reduced ore minerals coffinite [$U(SiO_4)_{0.9}(OH)_{0.4}$] and montroseite

[(V,Fe) O(OH)], as well as the secondary ore mineral carnotite [$K_2(UO_2)_2(VO_4)_2*3H_2O$] (Figure 2-4). Although these three minerals are the most economically important, a variety of other primary and secondary ore minerals have been reported within the Uravan mineral belt such as metatyuyamunite, tyuyamunite, rauvite, and corvusite (Table 2-1).

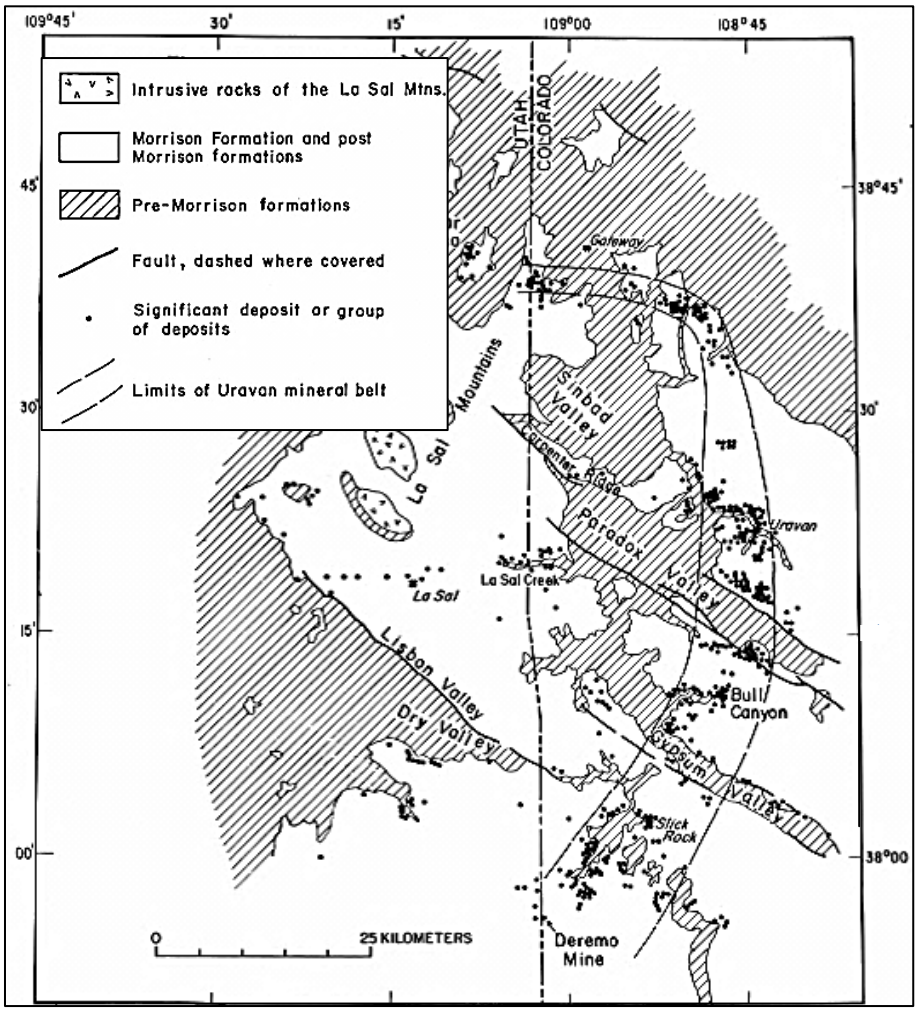

Figure 2-2: Map of southwestern Colorado and southeastern Utah showing location of Uravan mineral belt in the Salt Wash member of the Morrison Formation (after Chenoweth et al., 1981).

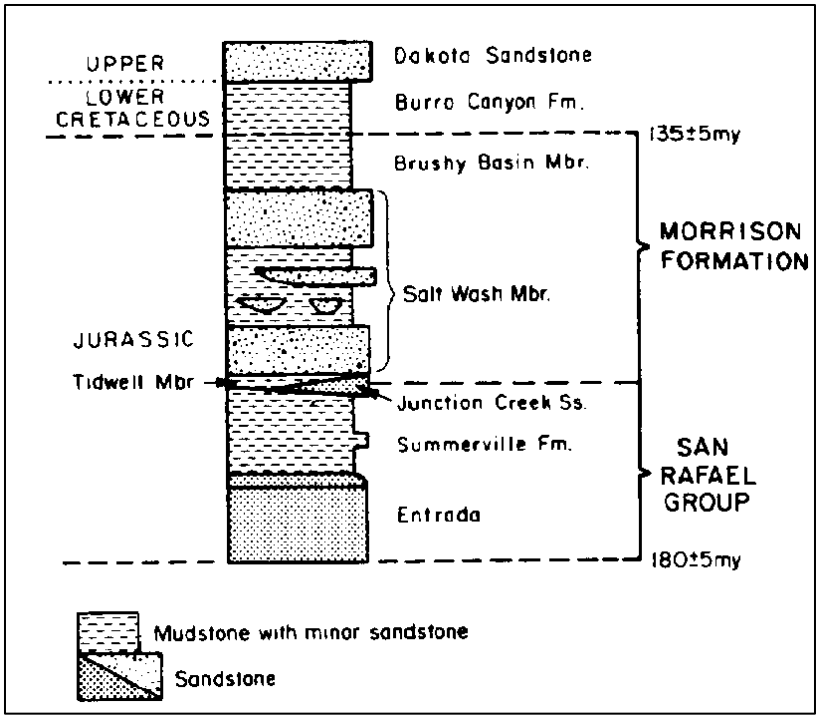

Figure 2-3: Stratigraphic cross-section of units present in Slick Rock District of Uravan Mineral Belt, Colorado (from Tyler and Ethridge, 1983).

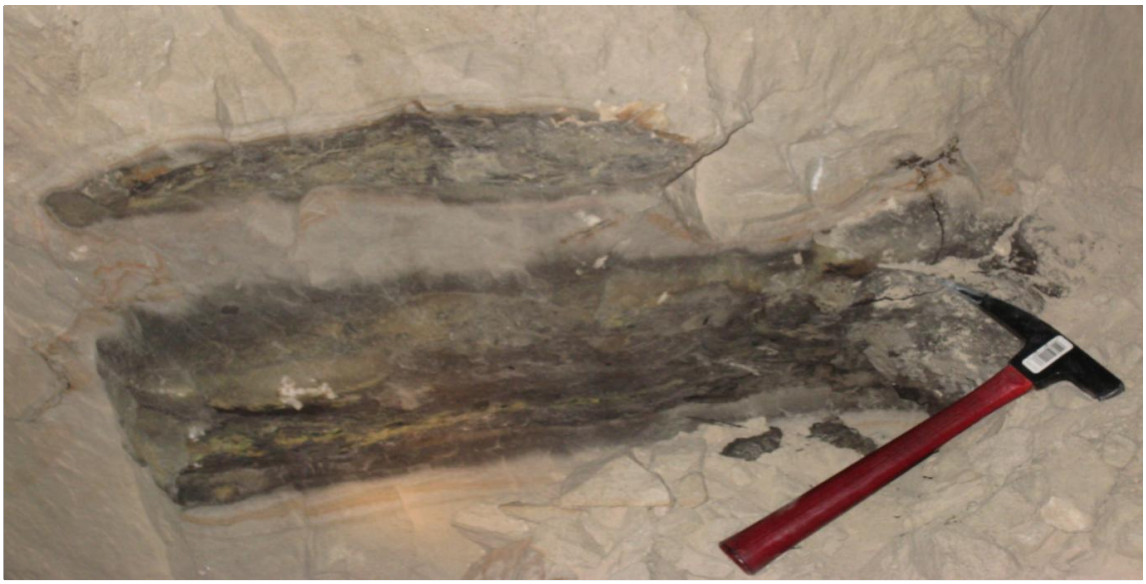

Figure 2-4: Photo of tabular sediment-hosted JD-6 uranium-vanadium deposit in underground workings. Primary minerals (coffinite, montroseite) are dark brown, grey or black. Secondary oxidized mineral carnotite is yellow and visible on working faces.

Table 2-1: Chemical formulae of uranium and vanadium minerals reported within the Uravan mineral belt (Barthelmy, 2014)

corvusite	$(Na_{(0.6)}Ca_{(0.25)}K_{(0.15)})V_8O_{20}*4H_2O$
metatyuyamunite	$Ca(UO_2)_2(VO_4)_2*3\text{-}5H_2O$
rauvite	$Ca(UO_2)_2(V_{10}O_{28})*16H_2O$
tyuyamunite	$Ca(UO_2)_2(VO_4)_2*5\text{-}8H_2O$

2.3 Regional Geology: Northwestern Nebraska

The High Plains region is a vast, nearly flat plateau extending from Nebraska through to the Coastal Plains of Texas and is included in the Great Plains province. The Pine Ridge escarpment surrounding the Crow Butte uranium roll-front deposit in northwestern Nebraska separates the High Plains from the Missouri Plateau to the north (Trimble, 1980; Collings and Knode, 1984). An arch system extending across South Dakota, Nebraska and Kansas has provided a greater understanding of the Precambrian sub-surface; basement rocks have been uplifted and exposed along the Black Hills uplift, as well as the Chadron and Cambridge arches (Figure 2-5). However, the majority of sub-surface information comes from thousands of exploratory oil and gas wells drilled in the region, especially along the arch system. The Chadron-Cambridge Arch system is the most structurally prominent feature in northwestern Nebraska and has strongly affected Oligocene sedimentation by deflecting an east-ward flowing braided river system to the south. Although periodic uplift along the entire arch system occurred throughout the Phanerozoic eon, the tectonic activity of each arch segment is believed to have occurred during separate episodes (Carlson, 1999). The project area is located in northwestern Nebraska within the east-west trending Crawford sub-basin, which is part of the larger

Tertiary Denver-Julesburg basin. The Tertiary sediments of the Crawford sub-basin overlie the Cretaceous Pierre Shale, and are marked by a paleosol up to 3 m thick; although the Pierre Formation is up to 1500 m thick outside of the Crawford sub-basin, it measures between 365 m and 460 m thick in Dawes County due to erosion prior to Oligocene sedimentation (Collings and Knode, 1984). A favourable hydrogeological system developed during the Black Hills Uplift (Tertiary), creating a slight dip of the Crawford basin and providing the means for mobilization, transport, and deposition of U in Nebraska. Groundwater flowed from west to east at the time of U deposition (opposite of present day flow). The White River Fault (Figure 2-5) cuts the Chadron and Brule sediments in the Crow Butte region with about 60m of vertical displacement, and has been dated as post-White River (late Oligocene) but pre-Pleistocene with little to nil water flow occurring across the fault through the Chadron aquifer (Gjelsteen and Collings, 1988). The highly impermeable Pierre Shale unconformably underlies the White River Group which consists of the Chadron and Brule Formations (Figure 2-6). Revised lithostratigraphic divisions have been proposed by Terry (1998) who reclassified and correlated the Chadron sub-units to similar units in South Dakota, as well as distinguished the pedogenically modified Pierre Shale as a separate unit (Figure 2-7). The revisions, however, are not officially recognized by the USGS at the present time and are not included in this study. The Lower Chadron sandstones, host to the Crow Butte deposit, are a braided-river valley-fill deposit, unconsolidated and poorly cemented with up to 20% authigenic clays. The Lower Chadron consists predominantly of arkosic, coarse-grained, cross-bedded sandstone with common clay interbeds and galls, the latter representing flood plain or low velocity deposits. The Lower Chadron is up to 100 m

thick regionally, but in the Crow Butte area is only approximately 12 m thick, and is overlain by brick red clay, often used as a marker bed, from the lower portion of the Middle Chadron which serves as the upper confining unit. The remainder of the Middle Chadron consists of greenish gray claystones formed from the reworking and devitrification of air-fall ash deposits, and the entire unit ranges between 12 m and 30 m in thickness. The Upper Chadron is composed of dark greenish blue and greenish brown siltstones and claystones representing fluvial channel and flood plain deposits and is approximately 30 m thick in the Crow Butte area (Collings and Knode, 1984; Gjelsteen and Collings, 1988; Hanly et al, 2009).

The Brule Formation conformably overlies the Chadron Formation, and is composed of the Orella and the Whitney Members, ranging from 150 m to 200 m in thickness. The Brule Formation consists of eolian and fluvially re-worked silt and claystones with minor sandstone lenses, and is the main outcropping unit within the Crawford sub-basin. The sediments of the Whitney Member contain anomalous amounts of U due to the large proportion of volcanoclastic material derived from volcanic centres to the west, and have been identified as a potential source of U for the underlying Chadron deposits (Collings and Knode, 1984; Gjelsteen and Collings, 1988; Hanly et al, 2009).

The Arikaree Group disconformably overlies the White River Group and is composed of three formations: the Oligocene Gering, the Miocene Monroe Creek and Harrison Formations representing channel and flood plain deposits. Both the Gering and Monroe Creek Formations are composed of buff to brown sandstone and siltstones, but the Monroe Creek is distinguished by the presence of concretions cemented by $CaCO_3$.

The Harrison Formation is a buff to light gray unconsolidated fossiliferous sandstone (Collings and Knode, 1984).

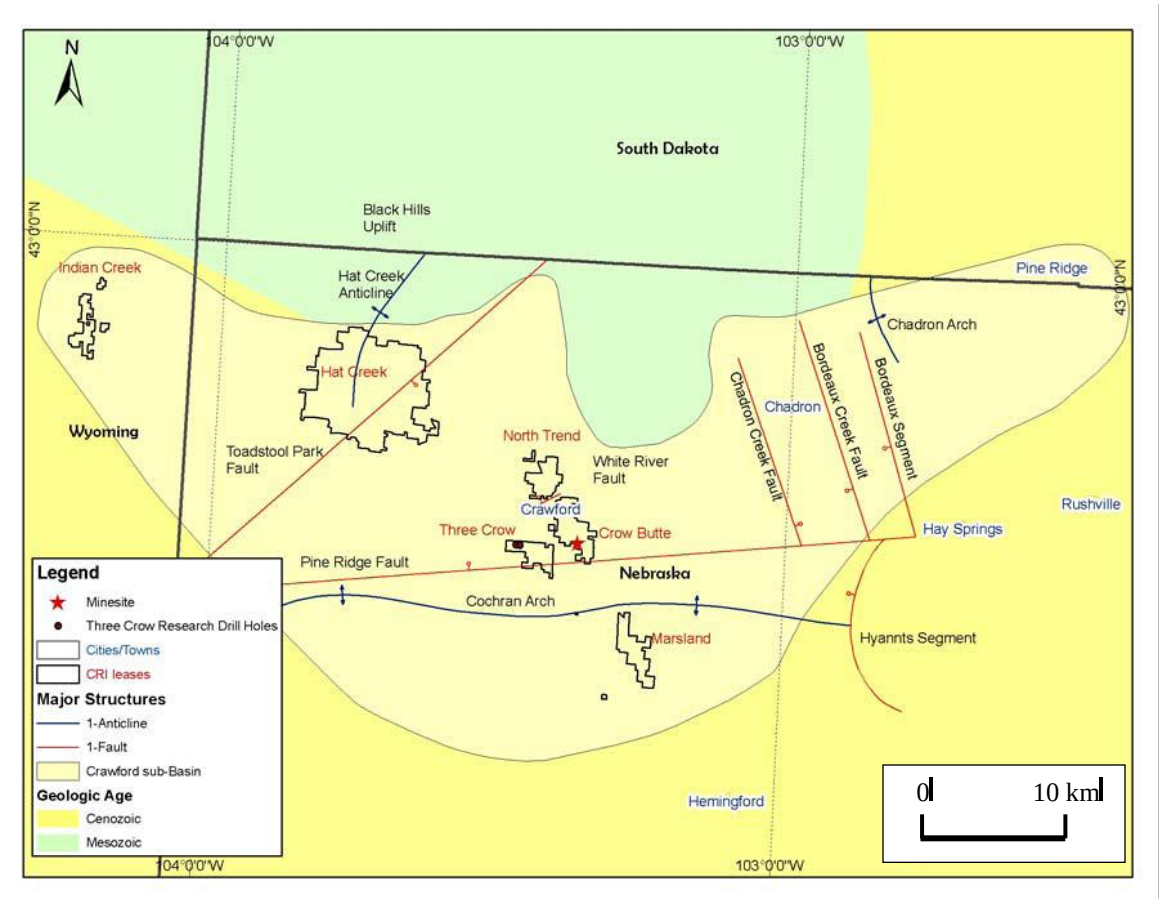

Figure 2-5: Map showing extents of the Crawford sub-basin and major structural features of the Crow Butte deposit and Three Crow study area in Nebraska (from Hanly et al., 2009).

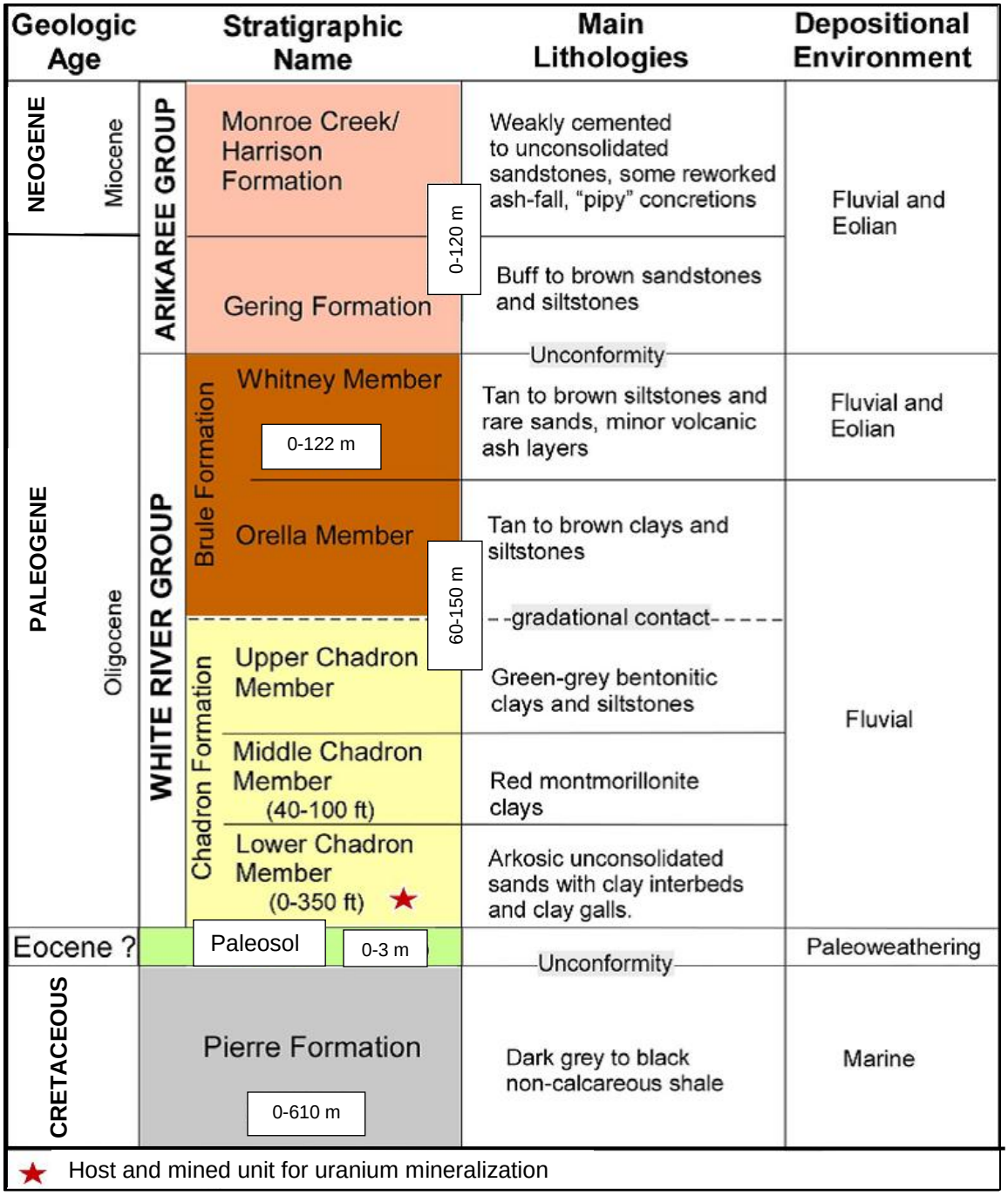

Figure 2-6: Age, stratigraphy, major lithologies, and depositional environment of the Crawford sub-basin, Nebraska (modified from Hanly et al., 2009).

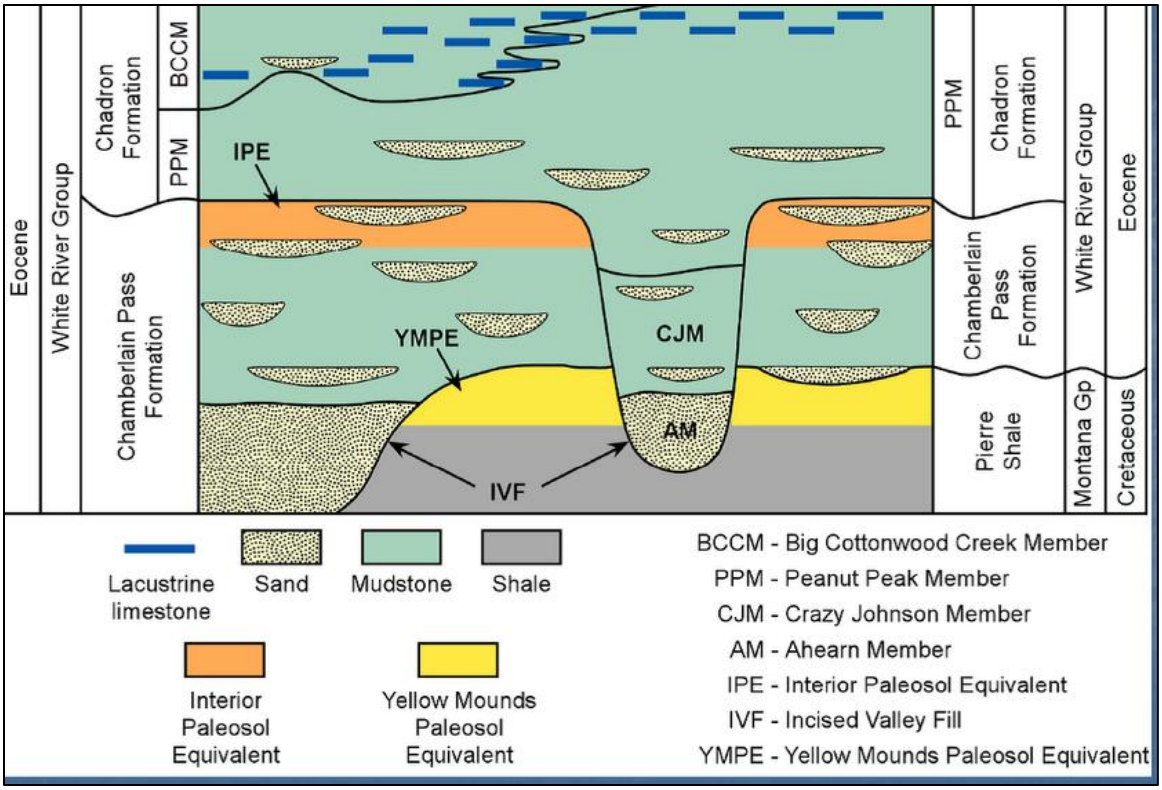

Figure 2-7: Revised lithostragraphic cross-section of the White River Group (from Terry, 1998).

2.4 Local Geology: Dawes County, Nebraska

The Three Crow uranium deposit is located 8 km southwest of Nebraska's first and only operating uranium mine Crow Butte, which is approximately 6 km from the town of Crawford in Dawes County (Figure 2-5). Uranium mineralization in Nebraska occurs within the lacustrine facies of the Brule Formation and the basal Chadron Formation of the Oligocene White River Group, although production has come exclusively from the Lower Chadron sands in the Crow Butte deposit. Uranium from the Crow Butte deposit is most likely derived from the overlying ash-rich beds of the Brule

Formation, and U deposition is believed to have occurred during the early Miocene (Zielinski, 1980; Gjelsteen, 1988).

In the Three Crow project area, the Brule Formation, Upper and Middle Chadron Members are similar to those described above (Figure 2-8). A gradational contact between the tan to brown coloured clays of the Brule Formation separates the greenish clays of the Upper Chadron Member. The Middle Chadron Member is predominantly red coloured clays with minor green coloured clay interbeds. The Lower Chadron Member hosts the most significant U mineralization in the study area; this lithology was initially identified in previous drill holes. A complete summary of gamma logs and detailed lithological descriptions collected during the 2009 drill program were reported by Hanly et al. (2009). The Lower Chadron Member is host to U mineralization in the study area, and is composed of silty to coarse-grained sands with an overall fining upwards sequence; shale and clay interbeds are common and limonite staining is abundant but sporadic.

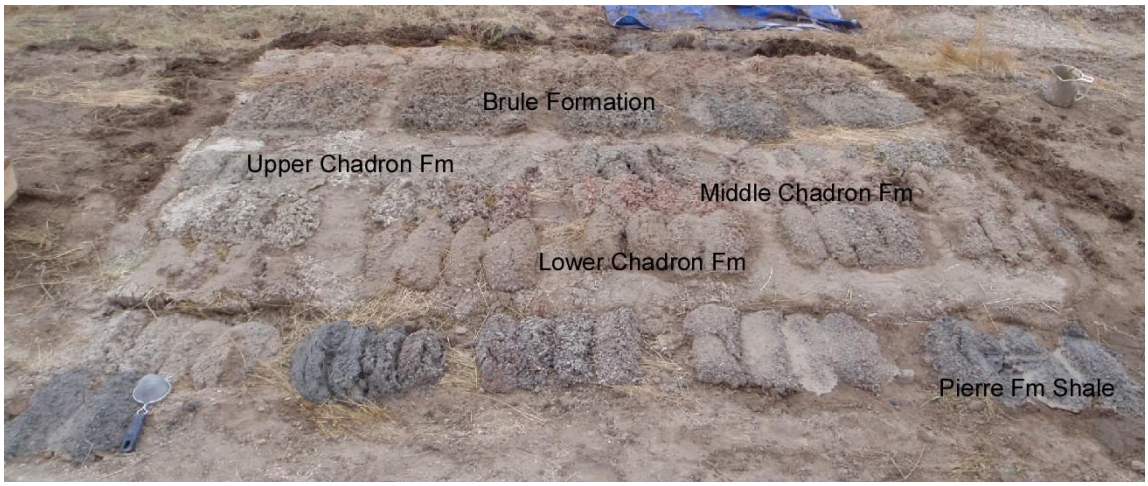

Figure 2-8: Photograph of drill cuttings from drill hole T797C. The cuttings are laid out in groups of four; samples were taken every 1.5 metres during drilling. Top of the hole: top left of photograph (Brule Formation), bottom of hole: bottom right (Pierre Shale). From Hanly et al. (2009).

Chapter 3. Methods

3.1 Sample Selection

3.1.1 Colorado sample suite

Twelve hand samples were collected from the SM-18 and JD-9 mines in Uravan, Colorado in 2005 by Fayek. In 2010, an additional eleven hand specimens were collected from the SM-18, JD-6 and JD-8 mines in the Uravan area by the author. Hand samples representative of both mineralized (oxidized and un-oxidized) and barren sandstones from the Salt Wash Member were sampled based on macroscopic appearance and Geiger counter measurements; samples were then documented and photographed.

3.1.2 Nebraska sample suite

Vacuum-sealed portions of drill core ranging from 0.15 to 0.30 metre (m) lengths from the Three Crow roll-front deposit in Dawes County, Nebraska were provided by Cameco Resources from their summer 2008 drill program; for details, see Hanly et al. (2009). The samples were taken along a 490 m fence across the roll-front, and represent the basal sands of the Lower Chadron Member; they were taken at approximately the same stratigraphic level from five zones of the roll-front. Six samples from the distal altered zone (T797C series) and the distal reduced zone (T810C series) each were taken at depths between 261.0 to 264.7 m and 272.0 to 275.4 m, respectively. Ten samples from the mineralized zone (H161C series) were taken at depths between 264.9 and 268.5 m. Sixteen samples from the proximal altered zone (H150C series) were taken at depths between 260.3 to 265.0 m and nine samples from the proximal reduced zone (T792C) were taken at depths between 267.3 to 271.0 m.

3.2 Methodology

Detailed hand specimen descriptions were recorded and polished thin sections were prepared from each sample from the Three Crow deposit, and from each hand specimen collected from the Colorado deposits. Macro- and micro-scale textures were characterized using optical and scanning electron microscopy (SEM); representative areas were selected for quantitative analysis by electron microprobe and secondary ion mass spectrometry (SIMS). Hand specimens are described in Appendix A.

3.2.1 Scanning electron microscope (SEM)

Preliminary examination was performed on carbon coated thin sections using a Cambridge Stereoscan 120 scanning electron microscope (SEM) equipped with a back scattered electron detector and an energy dispersive X-ray spectroscopy (EDS) detector. Since image brightness is proportional to the atomic weight of an element, BSE is ideal for locating U minerals due to the high atomic number of U. Energy dispersive spectrometry, also used in conjunction with the SEM, characterizes the elemental composition of minerals analysed and is useful in identifying variances in mineral composition. Collectively, these techniques were used to select areas of interest for further analysis.

3.2.2 Electron microprobe (EMP) analysis

Quantitative elemental analyses of U and V minerals were determined using a Cameca SX100 electron microprobe with PGT energy dispersive spectrometer equipped with five wavelength dispersive spectrometers, which offers a spatial resolution of about

1 µm. Operating conditions were 15 kV accelerating voltage with 20 nA beam current. Diopside, UO_2, fayalite, PbTe, andalusite, ThO_2, pyrite, olivine, orthoclase and VP_2O_7 were used as standards for Si, Ca, U, Fe, Pb, Al, Th, S, Mg, K and V, respectively. The limits of detection are 290, 4995, 435, 770, 980, 320, 820, 380, 430 and 200 parts per million (ppm) for elements Si, U, Ca, V, Pb, Al, Fe, Na, Mg and K, respectively. Major elemental analyses of these minerals are provided in Appendix C.

3.2.2.1 Chemical Pb Ages

Chemical lead (Pb) ages of U minerals from both Colorado and Nebraska samples were calculated using the atomic weight percent of Pb, U and Th measured with an electron microprobe (Appendix C) and used in conjunction with the Cameron-Schiman equation in Bowles (1990):

$$T = Pb \times 10^{10} / [(U \times 1.612) + (4.95 \times Th)] \quad [1]$$

3.2.3 Secondary ion mass spectrometry

Stable isotope compositions of sulphides and U-Pb isotopic content of U-bearing minerals from selected samples were measured by SIMS using a Cameca IMS 7F at the University of Manitoba. Areas of interest for U-Pb isotopic analysis were chosen based on petrography and quantitative electron microprobe data. Preparation of thin sections for SIMS analysis for both sulphur and U-Pb isotopic analyses was similar: thin sections were cleaned, polished, and cut into millimetre-sized sample fractions. Multiple fractions were mounted in cold epoxy, left to set overnight, and then coated with a thin layer of gold to create a conductive surface. For U and Pb isotopic measurements, a 10-15 nA primary beam of O^- was used and ions were detected by an electron transport particle

(ETP) electron multiplier coupled with an ion counting system with an overall deadtime of 25 ns. The following species were detected sequentially by switching the magnetic field: ^{204}Pb, ^{206}Pb, ^{207}Pb, ^{208}Pb, ^{230}Th, ^{232}Th, ^{234}U, ^{235}U, and ^{238}U. A typical analysis lasted ~20 minutes and consisted of 50 cycles.

For sulphur isotope analysis, a 1.8 nA primary beam of Cs^- was accelerated (+10 kV) onto the sample surface with a sputtering diameter of 25 μm. The instrument operated at a 200 V sample offset for sulphur, -10 kV secondary accelerating voltage and at a mass resolving power of 350. Ions were detected with an ETP electron multiplier coupled with and ion-counting system and an overall dead time of 34 ns. The sulphur isotopes $^{32}S^-$ and $^{34}S^-$ were detected sequentially by switching the magnetic field. A typical analysis lasted 6 minutes, and comprised 50 cycles.

3.2.3.1 Standards

During the measurement process by SIMS, an intrinsic mass-dependent bias is introduced, which is referred to as instrumental mass fractionation (IMF) and typically favours the low-mass isotope. The greatest contributor to the IMF is the ionization process, which depends most strongly upon sample characteristics (i.e., chemical composition). This is referred to as compositionally dependent fractionation or "matrix effects" (e.g., Riciputi et al., 1998). Therefore, accurate isotopic SIMS analysis requires that IMF be corrected for by using mineral standards that are compositionally similar to the unknown. Results from the SIMS analyses of the standard are compared to its accepted isotopic composition in order to calculate a correction factor that is applied to the unknowns measured during the same analysis session (e.g., Holliger and Cathelineau, 1988).

3.2.3.2 Sulphur isotope analysis

One sulphide sample of suitable size and representation was selected from each of the five zones of the Three Crow roll-front deposit, as well as sulphides from four mineralized samples collected from the JD-9 and JD-6 deposits; $\delta^{34}S$ values were measured using SIMS. The standards used in this analysis were large, homogeneous pyrite grains from the Balmat deposit in Maine, which has an average $\delta^{34}S$ of +15.1‰ (+/-0.3‰). Data are reported in the conventional δ (delta) notation relative to the Vienna-Canyon Diablo Troilite (V-CDT) standard, and is expressed as:

$$\delta^{34}S_{\text{V-CDT}}\ (‰) = \{(^{34}S/^{32}S)_{\text{sample}}/(^{34}S/^{32}S)_{\text{V-CDT}}-1\} \times 1000 \qquad [2]$$

3.2.3.3 U-Pb isotopic analysis

A total of fifteen spot analyses from the four types of U mineralization from the Colorado deposits were measured using SIMS to determine the U-Th-Pb isotopic composition. Activity coefficients of $^{238}U/^{234}U$ for each type of U mineral calculated using SIMS data indicate that all U minerals are in secular equilibrium ($A_{(\text{activity})}\ ^{238}U/^{234}U \approx 1$), therefore the U-Pb dating method was used to calculate the ages of U minerals (. The U-Pb ages of each U mineral type were calculated using the following equation:

$$^{206}Pb/^{238}U = e^{\lambda t}-1 \qquad [3]$$

where $\lambda(^{238}U) = 1.55125 \times 10^{10}$

This equation follows the assumption that the system is closed to U loss and the U minerals are in secular equilibrium (Faure, 1986). The $^{206}Pb/^{238}U$ ages are considered to be more reliable than ages calculated from $^{207}Pb/^{235}U$ principally because sandstone U deposits have been shown to be depleted in ^{235}U (Bopp et al., 2009). A common lead

correction was applied assuming $^{207}Pb/^{207}Pb = 18.954\pm1$ and $^{207}Pb/^{204}Pb = 15.635\pm0.11$ (Faure, 1986). Ages and errors were calculated using Isoplot (Ludwig, 1993) based on the weighted average.

The U-Th-Pb isotopic composition of seven spot analyses representing two types of U minerals from the Three Crow deposit was measured using SIMS. The $^{234}U/^{238}U$ activity coefficients were calculated from SIMS data and indicate that coffinite samples are not in secular equilibrium ($A_{(activity)}$ $^{238}U/^{234}U<1$) and are less than 1 Ma. The $^{230}Th/^{234}U$ method of dating was used in place of the U-Pb dating method due to insufficient accumulation of Pb. Ages for the two types of U minerals were calculated using the following equation:

$$t= (-(1/\lambda_{230}) \times \ln(1 - {}^{230}Th/{}^{234}U) \quad [4]$$

where $\lambda_{230}= 9.19 \times 10^{-6}$

Chapter 4. Results

4.1 Colorado Tabular Uranium Deposits

4.1.1 Hand sample descriptions

Samples from the JD-6 mine consist of dark grey, black and pale green, fine- to medium-grained, oxidized sandstone with common shale laminae. Dark grey, brown and yellow clay galls and laminae locally impart a mottled appearance. The outer, oxidized crust is yellow to orange, medium-crystalline and is approximately 1 to 2 cm thick. Detrital quartz composes the majority of the samples (50-70 vol. %) while lithic fragments, including clay clasts and volcanic rock fragments range from 5 to 10 vol. %, and feldspars are minor (trace to <5 vol. %). The sandstones are generally moderately to well-sorted. Samples from the SM-18 mine consist of light brown, light to dark grey, fine- to medium-grained, massive (reduced) sandstones interbedded with dark grey and green oxidized sandstone. Both oxidized and reduced sandstone beds range from <1 cm to ~15 cm in thickness. Reduced sandstone is composed mainly of quartz (up to 70 vol. %) with minor white feldspars (5 to 10 vol. %) and trace lithic fragments. The sandstone is generally well cemented by clay minerals (10 to 15 vol. %) and pore space-filling calcite (<2 vol. %). Oxidized sandstone is composed mainly of quartz (up to 50 vol. %), with lithic fragments (<10 vol. %) and minor feldspars (<2 vol. %). The oxidized sandstone is characterized by strong yellow alteration of matrix clay minerals. Samples from the JD-8 mine consists predominantly of light to dark grey (reduced), fine to medium-grained sandstones interbedded with discrete thin shale laminae, diffuse clay-rich beds and dark grey clay galls. The sandstones are composed of quartz (up to 70 vol. %), feldspar (5 to 10 vol. %) and minor lithic grains (<5 vol. %). Minor white, irregular,

centimetre-sized white carbonate lenses occur throughout. Exposed surfaces of samples are moderately oxidized and are dark grey and green with increased carbonate cement and yellow clay alteration. See Appendix A, Table 1 for hand sample descriptions and images.

4.1.2 Petrography

Polished thin sections of samples collected from both the SM-18 and Jo Dandy (SM-18, JD-6, JD-8, JD-9) mines were examined by reflected and transmitted light microscopy and thin section descriptions are presented in Appendix B. Accessory minerals from the SM-18 and Jo Dandy samples include pyrite, calcite, and trace amounts of barite, sphalerite, ilmenite, and zircon. Locally, quartz overgrowths fill pore space and commonly contain montroseite needles and clay minerals. Uranium minerals are essentially undistinguishable under transmitted or reflected light microscopy. Therefore U and V minerals were identified and characterized using SEM and EMP.

Organic matter was identified exclusively in JD-8 samples, and is composed of silicified, cellular plant fragments that comprise approximately 1-5% of mineralized samples. The fragments are generally less than 0.5 cm in length, and cell lumens occur as structurally well-preserved, or compacted into thin wavy laminae; both types are associated with V clay mineralization, but U mineralization only occurs within the compacted, ribbony laminae intergrown with V-clays. The following sections will focus on U, V, clay and sulphide minerals and mineral phases associated with the ore-bearing rocks.

4.1.2.1. Mineral paragenesis

The mineral paragenesis of samples from the SM-18, JD-6, JD-8 and JD-9 mines in Colorado is based on textures observed in thin section, SEM, EDS, EMP data and geochronology. The minerals can be subdivided into three formational components: detrital, authigenic, and ore-forming (Figure 4-1). The framework grains consisting of quartz, feldspar, rock fragments, detrital iron-oxides such as ilmenite and organic detritus were deposited in the mid-Jurassic and were cemented by clays, quartz overgrowths and minor calcite. The introduction and incorporation of V into cell lumens of organic matter and matrix clay minerals from the breakdown of V-bearing Fe-Ti oxides resulted in the formation of authigenic V-clay. The precipitation of montroseite from V-clays was followed by further development of quartz overgrowths during the authigenic stage. During ore-stage processes, the precipitation of coffinite, occurring principally through secondary replacement of montroseite, was immediately followed by the development of carnotite mineralization via oxidation of coffinite and montroseite. The precipitation of pyrite likely precedes coffinite mineralization, but is also associated with coffinite precipitation. Uranium mineralization consisting of carnotite and coffinite, occurring within matrix V-clays and disseminated within V-clay cement, continued and likely reflects regional fluctuations of groundwater-table levels.

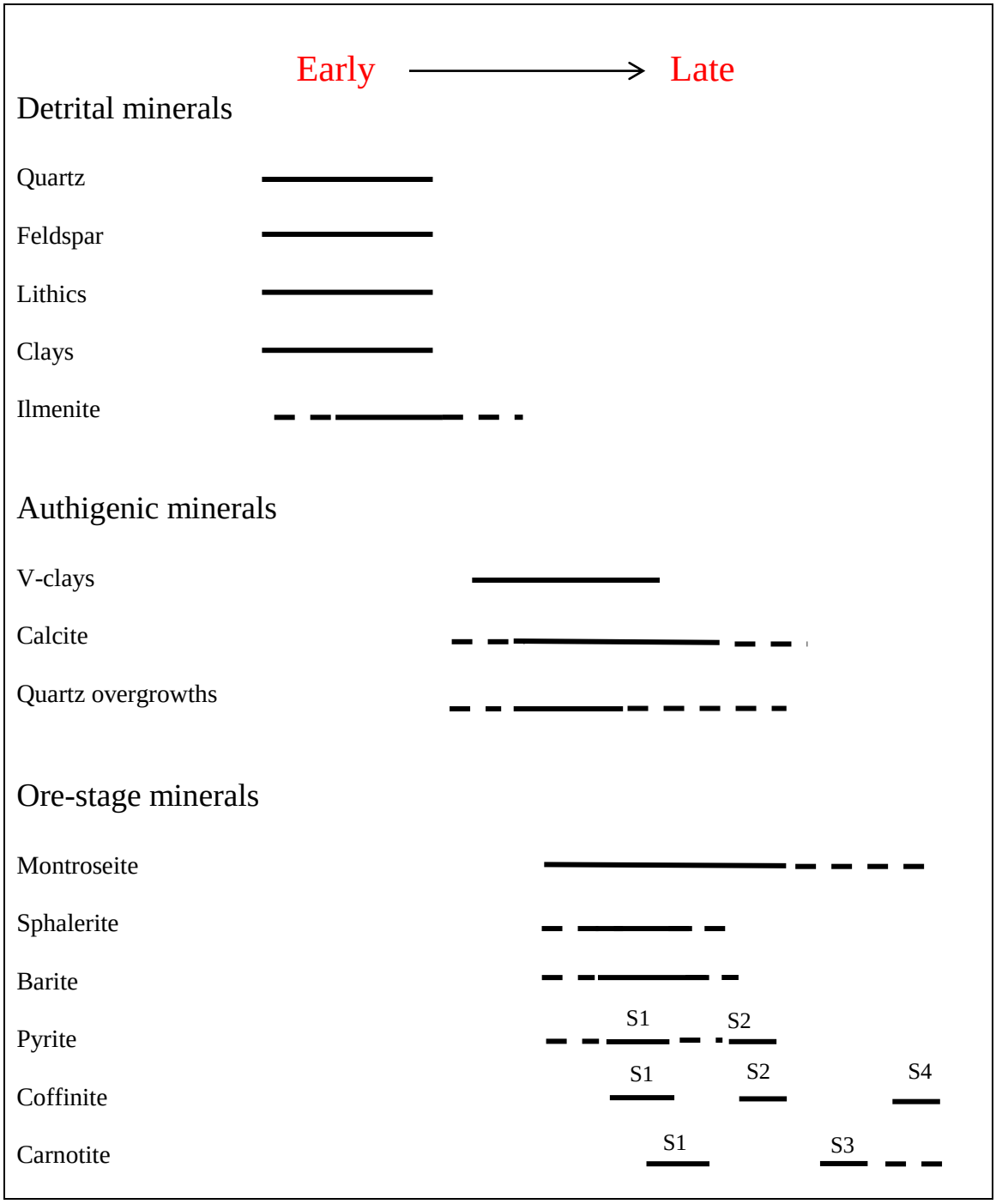

Figure 4-1: Paragenetic scheme illustrating the genetic sequence of minerals associated with the Colorado deposits.

4.1.2.2 Uranium minerals

Four types of U mineralization were identified based on chemical composition and morphology and are designated as S1 to S4 in Figure 4-1. The first type consists of coffinite that replaces montroseite. This particular type was identified in JD-6 and SM-18 samples only, and accounts for <2% of mineralized thin sections. Coffinite crystals are less than 2 μm in size, and replace montroseite along micro-fractures and at grain boundaries (Figures 4-2 A-C). The accurate chemical composition of coffinite from the SM-18 sample suites could not be accurately determined because of the small crystal size and the heterogeneous replacement textures. The analyses invariably include significant concentrations of V and Fe. Coffinite from sample JD-6-2 (Figure 4-2C) is characterized by 8.98 to 15.54 wt % SiO_2 and 63.31 to 78.53 wt % UO_2.

The second type of U mineralization was identified exclusively in the SM-18 sample suite and consists of crystalline carnotite which typically occurs interstitially to framework quartz grains (Figure 4-2D). A typical feature of carnotite is shrinkage cracks that likely developed during alteration (dehydration) of primary ore minerals such as montroseite as first documented by Hess (1927). Carnotite is characterized by 60.59 to 65.25 wt % UO_3, 22.70 to 30.84 wt % V_2O_5 and 3.89 to 7.26 wt % K_2O.

The third type of U mineralization is intimately associated with pyrite, but was documented exclusively in samples from the JD-9 deposit. BSE images of sample JD-9-5 (Figure 4-2E) show coffinite minerals precipitated as spheres and spindles that are intergrown with spheroidal pyrite in V-clay cement, where U minerals are less than 5μm in size. Electron microprobe analysis and data interpretation were difficult due to small crystal size and complex intergrowth texture.

The fourth type of U mineralization is genetically linked with V-clays, where U minerals are an alteration product of V-clay minerals. Several occurrences of this type are observed in SM-18, JD-8 and JD-9 samples, however due to impurities from V-clays, small crystal size of ore minerals, heterogeneous textures and variation in composition among and within the deposits, definitive mineral identification was not possible. Coffinite precipitating as disseminated grains from within V-clay cement was also identified in the JD-9 deposit and is characterized by 9.42 to 18.40 wt % SiO_2, 46.22 to 65.17 wt % UO_2, and 4.64 to 10.28 wt % V_2O_5 (Figure 4-2G,H). In sample SM-18-2-5 (Figure 4-2I), carnotite mineralization occurs within wispy, ribbony laminae of V-clay minerals, the latter constituting up to 70% of matrix minerals locally. The principal chemical components of this matrix mineralization from the SM-18 deposit range from 10.46 to 27.15 wt % SiO_2, 20.70 to 40.03 wt % UO_3, 18.46 to 21.36 wt % V_2O_5, 1.72 to 12.11 wt % Al_2O_3, 1.56 to 9.25 wt % FeO, 4.02 to 6.48 wt % K_2O and 0.47 to 4.67 wt % MgO. In sample SM-18-1-3, carnotite appears to replace detrital quartz (Figure 4-2J), and occurs as aggregates of amorphous blebs, within and surrounded by, V-clay minerals. This mineralization is characterized by 5.21 to 26.14 wt % SiO_2, 30.46 to 56.27 wt % UO_3, 11.87 to 21.03 wt % V_2O_5, 4.42 to 19.33 wt % Al_2O_3 and 4.22 to 7.35 wt % K_2O. In contrast, U-rich V-clay in sample JD-8-2 (Figure 4-2K) is characterized by <0.01% to 37.98 wt % SiO_2, 8.58 to 63.10 wt % UO_2, 20.91 to 50.85 wt % V_2O_3, 3.83 to 10.36 wt % Al_2O_3, 0.06 to 1.64 wt % FeO, 0.97 to 6.33 K_2O and 0.09 to 2.52 wt % MgO. Uranium mineralization associated with V-clays in sample CB-12-8 (JD-9 deposit) occurs disseminated within matrix V-clay (Figure 4-2L); U minerals are characterized by 32.81 to 46.27 wt % SiO_2, 2.11 to 9.37 wt % UO_2, 14.04 to 24.31 wt % V_2O_5, 9.07 to 19.78 wt

% Al_2O_3, 1.58 to 6.47 wt % K_2O, 0.48 to 1.33 wt % CaO, and 1.49 to 5.81 wt % MgO. The significant variation in chemical composition suggests a complex intergrowth of early-stage U minerals.

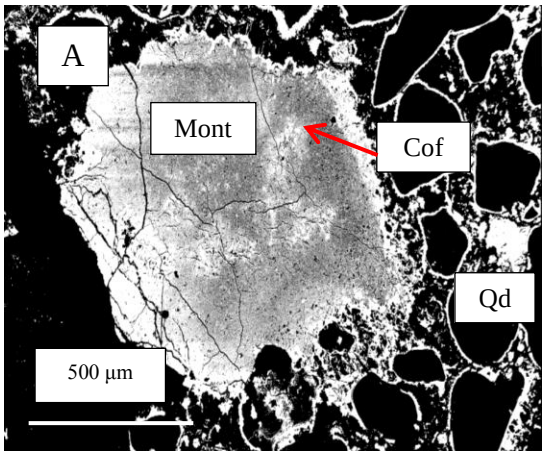
A
Mont
Cof
Qd
500 µm

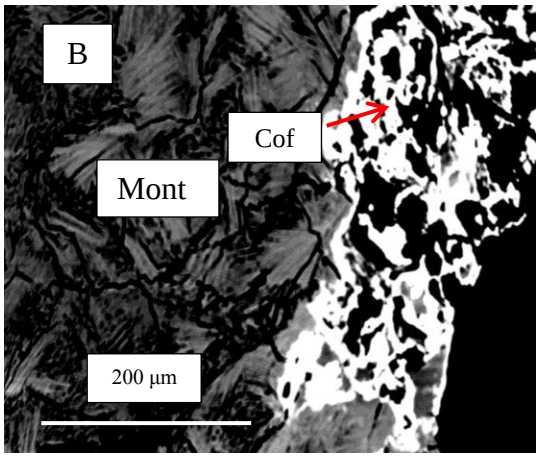
B
Cof
Mont
200 µm

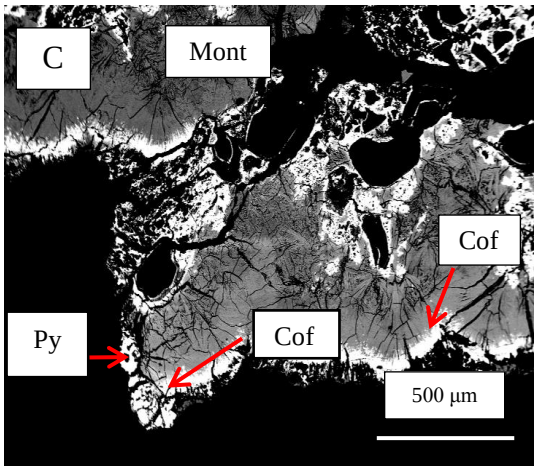
C
Mont
Cof
Py
Cof
500 µm

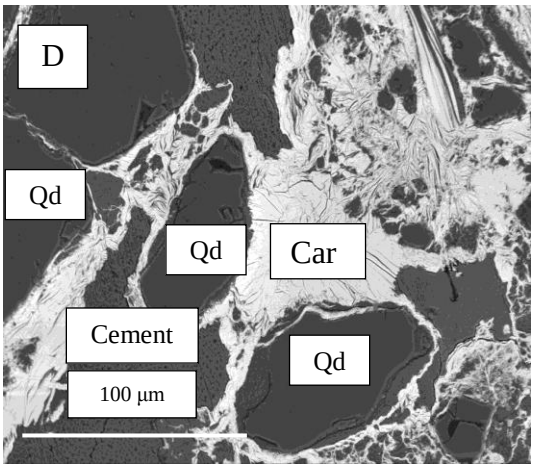
D
Qd
Qd
Car
Cement
Qd
100 µm

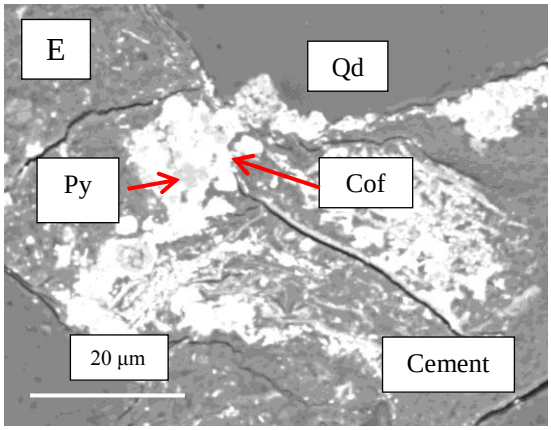
E
Qd
Py
Cof
20 µm
Cement

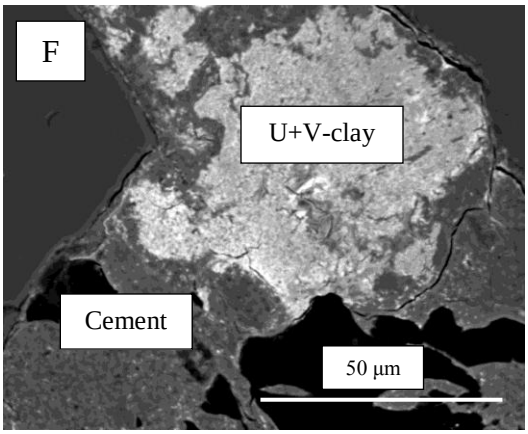
F
U+V-clay
Cement
50 µm

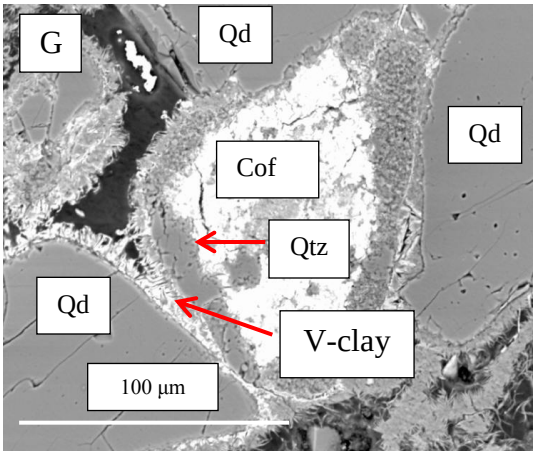
G
Qd
Qd
Cof
Qtz
Qd
V-clay
100 µm

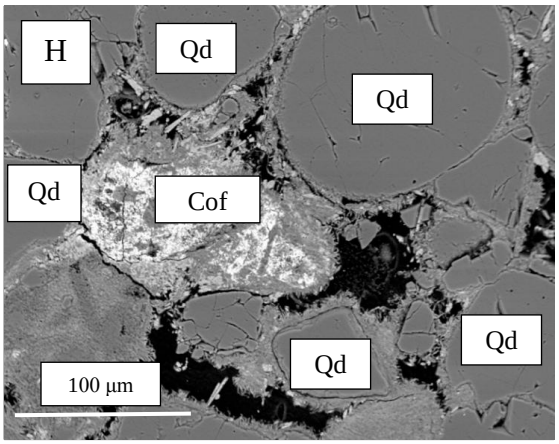
H
Qd
Qd
Qd
Cof
Qd
Qd
100 µm

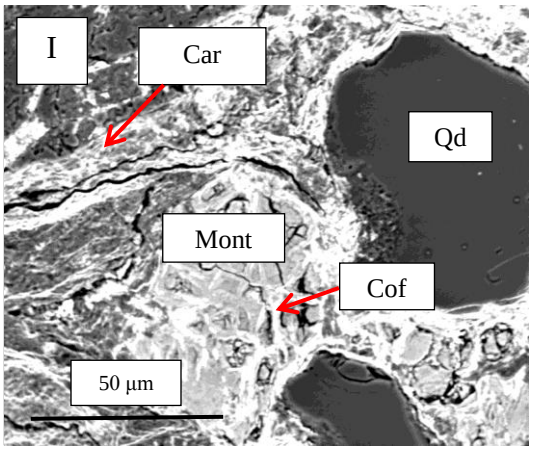
I
Car
Qd
Mont
Cof
50 µm

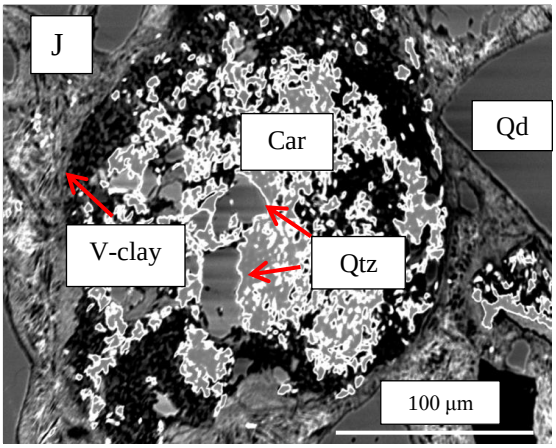
J
Car
Qd
V-clay
Qtz
100 µm

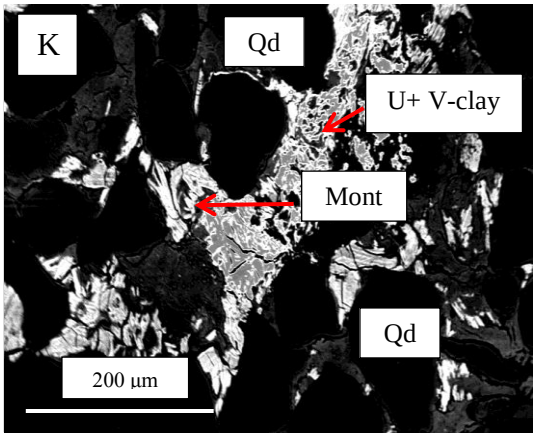
K
Qd
U+ V-clay
Mont
Qd
200 µm

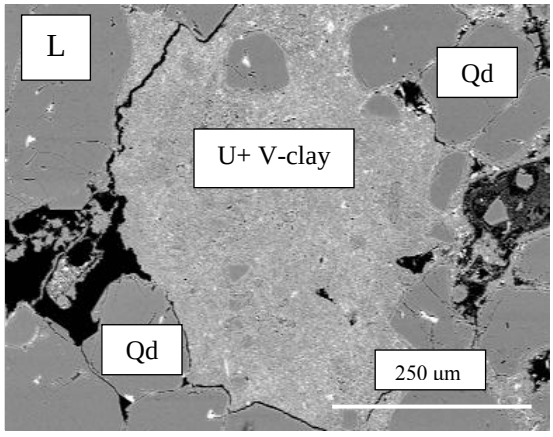
L
Qd
U+ V-clay
Qd
250 um

Figure 4-2 (see pp. 39-40): (A) BSE image of type 1 uranium mineralization: coffinite (bright white) replacing montroseite (dark grey) along grain boundaries and within micro-fractures. Sample JD-6-2. (B) High magnification BSE image of type 1 uranium mineralization: coffinite (bright white) replacing montroseite aggregate (dark grey) along grain boundary. Sample JD-6-2. (C) BSE image of coffinite (bright white) replacing montroseite (grey) along grain boundaries. Bottom: pyrite associated with coffinite. Sample JD-6-2. (D) BSE image of type 2 uranium mineralization showing carnotite interstitial to framework quartz grains. Sample SM-18-1-3. (E) BSE image of type 3 uranium mineralization: coffinite minerals (bright white) occur as spheres and spindles intergrown with spheroidal pyrite (grey). Sample CB-12 (JD-9). (F) BSE image of type 4 uranium mineralization associated with V-clay. Sample CB-12 (JD-9). (G) BSE image of type 4 coffinite minerals precipitating from V-clay cement and proximal to remnant quartz. Sample CB-12 (JD-9). (H) BSE image of type 4 uranium mineralization showing coffinite precipitating from V-rich matrix clays. Sample CB-12 (JD-9). (I) BSE image of montroseite (grey) partially replaced by coffinite (bright white) and texturally continuous with type 4 ribbony, carnotite and-vanadium clay minerals. Sample SM-18-2-5. (J) BSE image of type 4 carnotite minerals replacing quartz. Sample SM-18-1-3 (K) BSE image of type 4 uranium mineralization showing montroseite precipitating from V- clay. Sample JD-8-1-2. (L) BSE image of type 4 uranium minerals disseminated within a matrix of V-clays. Sample CB12-8 (JD-9). Qd: detrital quartz; Cof: coffinite; Mont: montroseite); Py: pyrite; U+V-clay: unidentified uranium minerals associated with V-clay.

4.1.2.3 Vanadium Minerals

Montroseite is a low-valent vanadium oxide mineral that forms principally by alteration of V-clays, and is an important ore-forming mineral in the Jo Dandy deposits. Montroseite was documented from JD-6 samples and typically occurs interstitial to framework grains, along quartz grain boundaries and as inclusions within quartz overgrowths (Figures 4-3 A-C). Montroseite typically occurs as aggregates of microscopic, randomly oriented or fan-shaped, bladed crystals; aggregates are partially replaced by coffinite within micro-fractures and along grain boundaries (Figure 4-2A, B). In sample JD-6-2, montroseite is characterized by <0.01 to 4.74 wt % UO_2, 70.88 to 77.68 wt % V_2O_3, and 6.65 to 17.34 wt % FeO. Montroseite identified in JD-8 samples is in the form of aggregated bladed crystals (Figures 4-3B) and is characterized by 62.90 to 79.22 wt % V_2O_3 and 8.49 to 11.78 wt % FeO.

The partial alteration of Fe-Ti oxides to V-clay is shown in Figure 4-3D where V-clays fill microfractures and partially replace Fe-Ti oxide minerals; this type of secondary replacement was also noted in a previous study by Meunier (1994). The Fe-Ti oxide mineral ilmenite was initially distinguished petrographically as discrete ilmenite lamellae, and was analysed using EDS to verify its chemical composition. In sample JD-8-2, V-clays occur within the cell-lumens of fossil wood, and are texturally associated with montroseite (Figure 4-3E). The V-clays in the JD-8 deposit are a mixture of vanadium-bearing illite and chlorite (Table 4-1) and are similar to the clays described by Meunier (1994) in the Slick Rock district. The occurrence of montroseite crystals within quartz overgrowths indicates that authigenic silica was deposited after vanadium mineralization. In addition, the common spatial association between coffinite and V minerals suggests a genetic link.

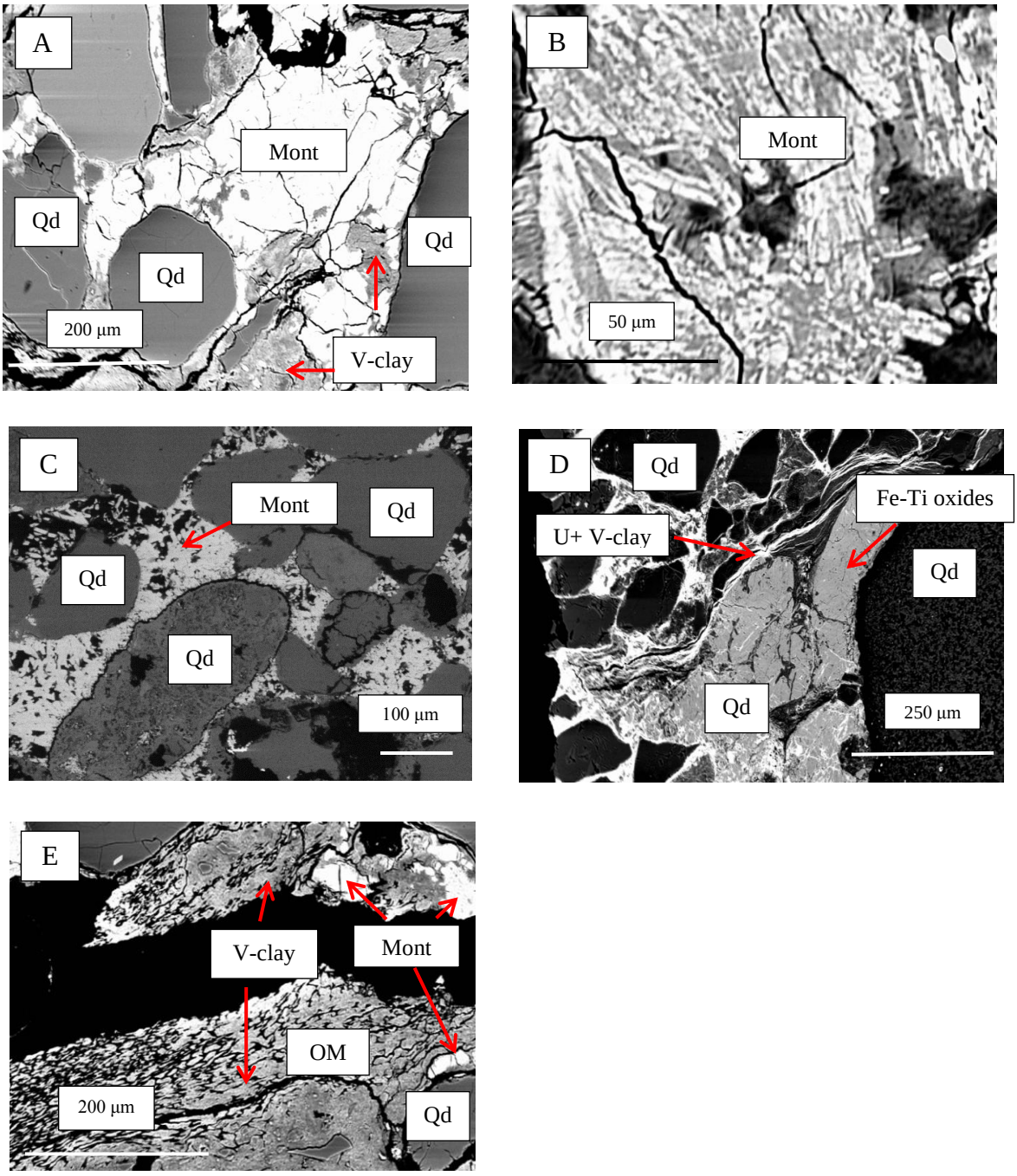

Figure 4-3: (A) BSE image of montroseite precipitating from matrix V-clay. Sample JD-8-1-2. (B) High magnification BSE image of montroseite aggregate with shrinkage cracks. Sample JD-8-1-2. (C) BSE image of montroseite crystals precipitating within pore space. Sample JD-6-1. (D) BSE image of detrital Ti-Fe oxides partially altered by uranium-rich V-clay with proximal carnotite mineralization. Sample SM-18-5. (E) BSE image of vanadium mineralization within cell lumens of fossil wood with proximal montroseite mineralization. Sample JD-8-1-2.

Table 4-1: Partial EMP analysis of vanadium clays (*=averages from Meunier, 1994)

	SiO_2	**Al_2O_3**	**V_2O_3**	**FeO**	**MgO**	**CaO**	**Na_2O**	**K_2O**
Jo-Dandy	47.24	15.76	22.20	1.73	5.16	0.36	0.09	4.52
	46.60	13.67	24.50	1.06	2.82	0.31	0.09	5.74
	43.75	13.05	29.02	0.86	2.62	0.29	0.08	5.98
	34.02	19.92	21.87	2.77	11.81	0.35	0.11	0.27
	43.50	14.90	24.12	1.84	4.79	0.34	0.06	5.36
	37.01	12.75	33.99	1.76	3.97	0.81	0.22	4.85
	38.86	12.89	27.76	1.94	3.80	0.44	0.14	5.46
	31.39	13.87	40.74	3.01	6.40	0.56	0.23	3.01
Slick Rock illite *	42.80	14.10	21.40	1.17	3.57	0.16	0.00	6.35
	40.17	13.26	17.61	2.12	3.00	0.19	0.00	7.31
Slickrock chlorite *	33.95	22.09	11.70	4.31	13.04	0.04	0.00	0.22

4.1.2.4 Sulphide minerals

Sulphide minerals identified in samples from the Jo Dandy (JD-6, JD-8, JD-9) and SM-18 mines consist of pyrite, which composes <1% of thin sections examined with reflected light microscopy. The three main morphological types of pyrite identified in thin section are: 1) framboidal, 2) subhedral, and 3) pyrite texturally associated with U and V mineralization. Type 1 framboidal pyrite occurs as both densely packed aggregates and smaller, more diffuse spheroidal aggregates. Framboids are typically <2 μm in size. Type 2 subhedral pyrite grains have an average grain size of ~10 μm, but range from <3 to 100 μm and are erratically distributed throughout the samples. Type 3 pyrite was identified in sample JD-6-2, where it occurs as subhedral crystals <2 μm in size and is texturally associated with coffinite mineralization along grain boundaries of montroseite.

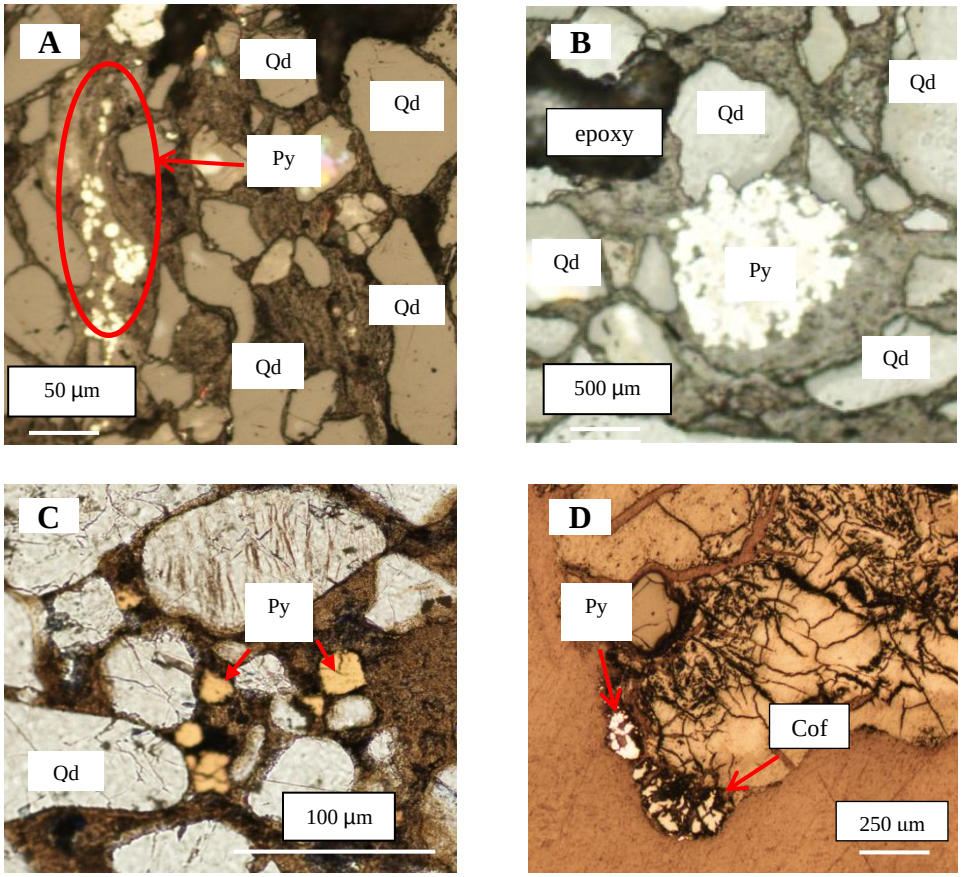

Figure 4-4: Reflected light images of the three morphological types of pyrite analysed by SIMS. (A) framboidal pyrite, (B) framboidal pyrite, (C) subhedral pyrite and (D) pyrite texturally associated with coffinite. Qd: detrital quartz; Cof: coffinite; Mont: montroseite; Py: pyrite.

4.1.3 Chemical Pb ages

Chemical Pb ages were calculated from electron microprobe data (Tables 1-9; Appendix C) for each type of U mineralization identified in JD-6, JD-8, JD-9 and SM-18 samples as described above. Type 1 coffinite from sample JD-6-2 gives chemical Pb ages ranging from 1.1 to 56.6 Ma. Calculated chemical Pb ages of type 2 carnotite from sample SM-18-1-3 range from 0.3 to 5.7 Ma, with one outlier at 71.7 Ma. Type 3 coffinite intergrown with pyrite contains Pb levels below detection limits and therefore chemical Pb ages could not be calculated. Calculated ages for type 4 coffinite mineralization associated with V-clay cement in sample CB-12-8 (JD-9 mine) range

between 0.6 and 5.3 Ma. Three data points representing type 4 mineralization from sample SM-18-2-5 give ages ranging from 93.3 to 132.2 Ma, while the remaining data from the same sample gave mineralization ages older than their host rocks, ~150 Ma (Bradshaw, 2010).

4.1.4 U-Th-Pb geochronology

Data from *in situ* SIMS isotopic analyses were used to calculate U-Pb ages for each type of U mineralization (Appendix D). Stage 1 U mineralization consists of type 1 coffinite (Figure 4-2A) and type 2 carnotite (Figure 4-2D), which give an average age of 34 ±5 Ma (MSWD=2.4; 7 analyses). Stage 2 U mineralization consists of type 3 coffinite from JD-9 (Figure 4-2E), which gives an age of 22 ±3 Ma. Stage 3 U mineralization is the most abundant type of mineralization and consists of type 4 carnotite (Figure 4-2H), which gives an age of 11±3 Ma. Stage 4 coffinite mineralization (Figure 4-2G), which occurs as disseminated grains within V-clay cement, is 3 ±1 Ma old.

Figure 4-5 shows the distribution of activity ratios of U^{234}/U^{238} and Th^{230}/U^{238} reported in Table 2 (Appendix D) with 5 and 10% errors, respectively. With the exception of two analyses, the majority of the U minerals are in secular equilibrium, which suggests that the U-Pb isotopic system was undisturbed.

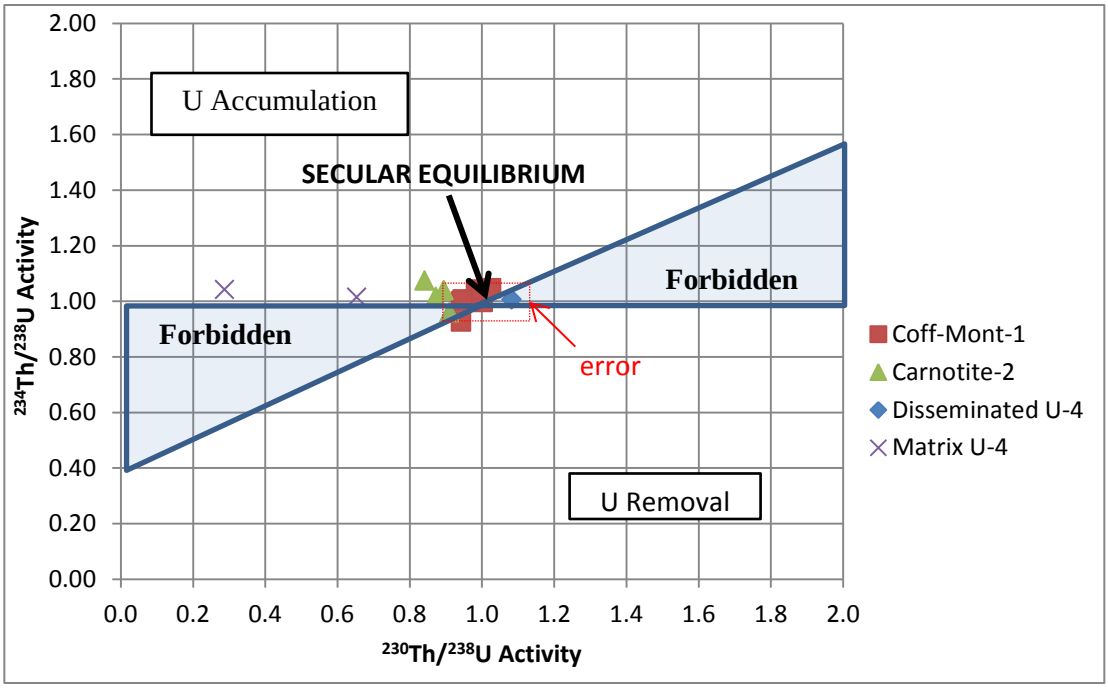

Figure 4-5: Disequilibrium plot showing effects of rock-water interactions for uranium mineral phases; the position of data points indicates the net gain or loss of uranium from deposits. Shaded forbidden zones can only be reached via complex alteration processes. Note: numbers after each phase in legend correspond to uranium mineralization type described in 4-1. Adapted from Scott et al. (1992).

4.1.5 Sulphur isotopic analysis of pyrite

Three distinct morphological types of pyrite from the JD-6 and JD-9 deposits were analyzed using SIMS (Appendix D). Two different occurrences of framboidal pyrite from sample JD-9-5 have $\delta^{34}S$ values ranging from -20.7‰ to -26.3‰ (Figure 4-4A) and -34.9‰ to -35.9‰ (Figure 4-4B). Subhedral pyrite from sample JD-9-4-7 has $\delta^{34}S$ values of -23.1‰ to -51.7‰ (Figure 4-4C). Both the subhedral and framboidal pyrite are enriched in ^{32}S and have isotopic values that are consistent with biological sulphide reduction because sulphate reducing bacteria selectively oxidize low-molecular-weight compounds and reduce the lighter ^{32}S (Southam, 2012). In sample JD-6-2, pyrite that is spatially associated with U mineralization (Figure 4-4D) has $\delta^{34}S$ values ranging

from -5.0‰ to -13.3‰, which suggests that chemical rather than biological processes are responsible for the formation of pyrite from the JD-6 mine. Currently, the original source of sulphur is poorly characterized. However, one potential source of sulphate is the underlying evaporite facies (e.g., Goldhaber et al., 1987)

4.2 Three Crow Roll-Front Uranium Deposit, Nebraska

4.2.1 Hand sample descriptions

Samples from the distal altered (oxidized) zone (T797C) consist of light to medium grey and brown, fine- to very fine-grained to silty sand with common clay interbeds and galls. Common sandstone lenses composed of medium- to coarse-grained sand with dark, rounded cobbles. Local yellow to orange limonite stains impart a mottled appearance to the sand. Samples are moderately to poorly indurated and moderately to poorly sorted. In the proximal altered (oxidized) zone (H150C), samples consist of medium brown, green and yellow, medium-grained to very fine-grained, silty sand. Clay interbeds and galls locally impart a mottled appearance. Sparse dark reddish brown stained laminae are <1 cm thick and minor light pink to dark red stained centimetre-sized lenses occur throughout. Sands are generally poorly indurated and are moderately-sorted. In the mineralized (H161C) zone, samples consist of medium to dark grey, interbedded coarse- to medium to fine sand and conglomerate. Clay interbeds typically range from <1 cm to 2 cm in thickness, but clay content increases towards the base of the sequence. Minor discontinuous, millimetre-thick shale laminae occur throughout the samples. The clay interbeds and galls are locally stained yellow and red. Samples are moderately to

very poorly indurated and poorly sorted. Samples from the proximal altered (reduced) zone (T792C) consist predominantly of medium brown to light grey, very fine- to medium-grained, silty sand, with interbeds composed of coarse to medium-grained sandy lenses and silty clay laminae. Abundant green and reddish orange clay mottling occurs towards the bottom of the interval. The sandstones are generally poorly sorted, moderately to poorly indurated and porous. Samples from the distal altered (reduced) zone (T810C) consist of light to medium grey, green and brown, fine-grained sandstones with minor dark grey, brown and reddish coloured clay galls that locally impart a mottled appearance. Rare centimetre-sized yellow clay lenses occur near the top of the interval. Samples are generally poorly indurated and moderately to well-sorted. See Appendix A (Table 2) for hand sample descriptions and Appendix B for thin section descriptions.

4.2.2 Petrography

Polished thin sections of drill core samples from the five zones of the Three Crow roll-front were examined by reflected and transmitted light microscopy. Accessory minerals include pyrite, hematite and trace calcite and zircon. Due to the scarcity of U mineralization and the overall fine-grained nature of the samples, U minerals are indistinguishable with transmitted or reflected light microscopy. Therefore, U minerals were identified and characterized using SEM and EMP.

Important features such as a mini-roll front and evidence of redox reactions between hematite and pyrite were identified using reflected and transmitted light, and the chemical composition of hematite and pyrite was analyzed using EDS. In thin section H150C-09 from the proximal altered zone (Figure 4-6A), a mini-roll front is apparent at

the sharp contact between oxidized, hematite-rich sediments and light grey, reduced sediments. In thin section T797C-06 from the distal altered zone (Figure 4-6B), medium crystalline hematite occurs with very fine-grained pyrite inclusions, and represents the principal redox reaction that is responsible for the formation of roll-front deposits.

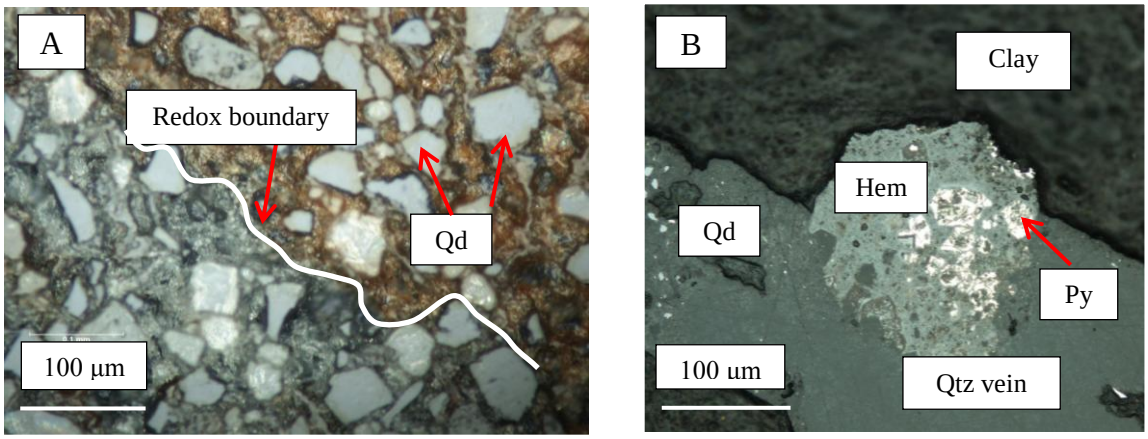

Figure 4-6: (A) Transmitted light image of contact between reduced (grey) sediments and oxidized (red) sediments. Sample H1050C-09 (B) Reflected light image of hematite with pyrite inclusions in quartz vein. Qd: detrital quartz; Hem: hematite; Py: pyrite. Sample T797C-06.

4.2.2.1. Mineral paragenesis

The mineral paragenesis of samples from the Three Crow deposit is based on textures observed in thin section, as well as SEM, EDS and EMP data. The minerals can be grouped into three formational components: detrital, authigenic, and ore-forming (Figure 4-7). Detrital minerals such as quartz, feldspar, pyrite and lithic grains were deposited during the Oligocene and cemented by authigenic clays and minor calcite. Authigenic minerals such as pyrite and clays developed during diagenesis of detrital minerals. Coffinite precipitated from the late to early Pliocene, and was likely preceded by and also continuously co-precipitated with biogenically-mediated pyrite.

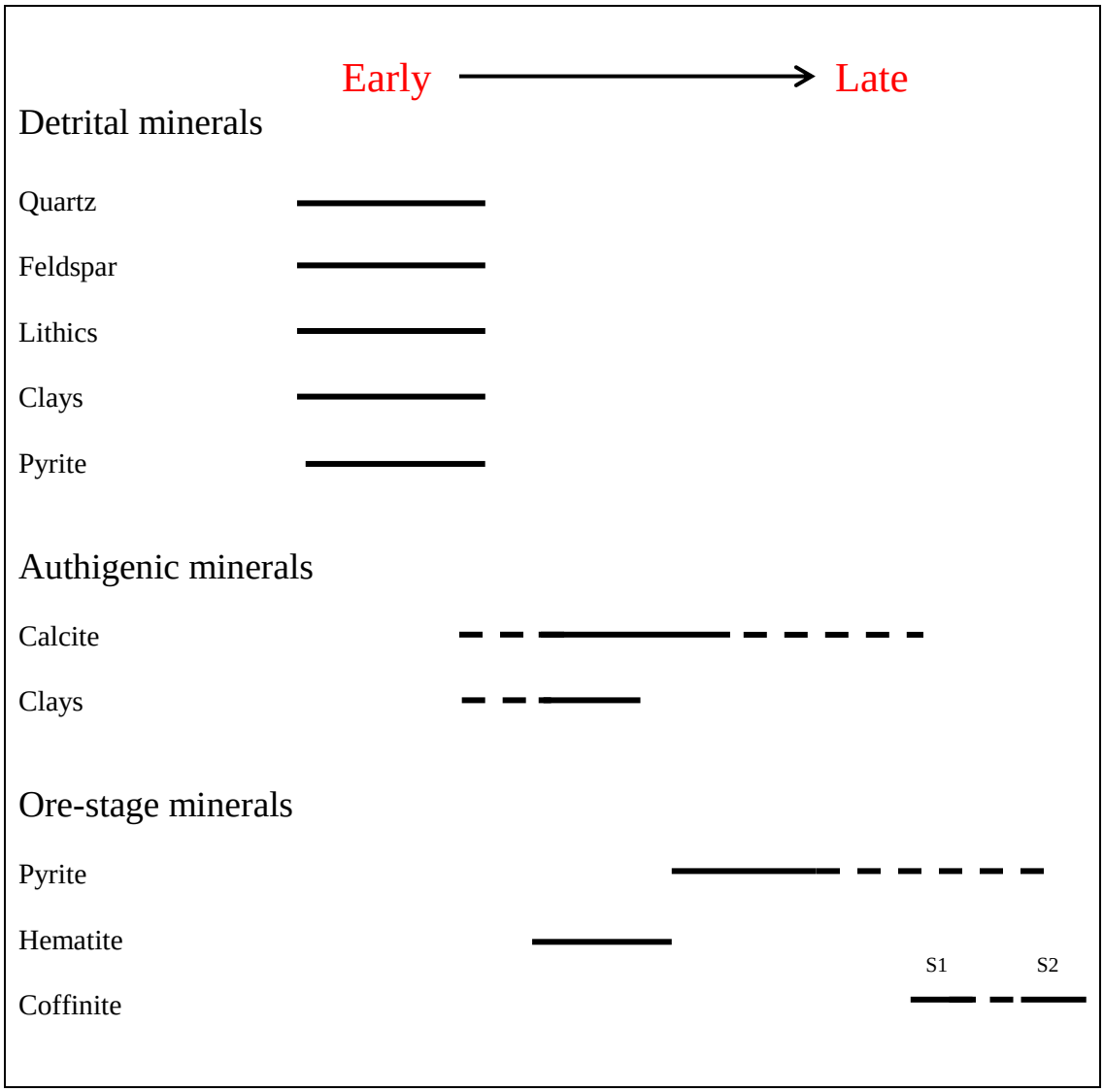

Figure 4-7: Paragenetic scheme illustrating the genetic sequence of minerals associated with the Three Crow roll-front deposit, Nebraska.

4.2.2.2 Uranium mineralization

Two types of uranium mineralization (designated as S1 and S2 in Figure 4-7) were identified in one thin section of sample H161C-04 from the mineralized zone. Type 1 U mineralization consists of coffinite that occurs within dissolution cavities of a detrital quartz grain with an average crystal size <1 μm. Type 2 U mineralization also consists of

coffinite and is associated with pyrite within a micro-fracture in a detrital quartz grain, with an average crystal size of <2 μm.

The type 1 U mineralization was characterized by EMP and identified as coffinite. Dissolution cavities have irregular, angular to rounded outlines that collectively impart a vague sub-parallel fabric across the host quartz grain. Coffinite occurs within these cavities as fine grained (<2 μm) clusters (Figures 4-8 A,B). The main chemical components of coffinite are 54.26 to 62.69 wt % UO_2 and 17.80 to 24.80 wt % SiO_2. Element distribution maps were created using EMP and show the distribution of Si, U, Fe and Pb (Figure 4-9). Locally, rare pyrite grains <1μm in size are intergrown with coffinite within these cavities.

Type 2 coffinite mineralization is spatially associated with pyrite, and occurs within a micro-fracture in detrital quartz. Coffinite crystals are less than 2μm, and occur with anhedral to subhedral pyrite along a fracture of a single quartz grain (Figures 4-10A-C). Coffinite mineralization is characterized by 50.21 to 63.39 wt % UO_2 and 11.92 to 24.52 wt% SiO_2 and possesses a similar U/Si molar ratio as type 1 coffinite. A gradational contact between pyrite and coffinite is visible in reflected light and BSE images (Figure 4-10C), but in order to investigate the textural relations between coffinite and pyrite, element distribution maps were created using EMPA analysis (Figure 4-11).

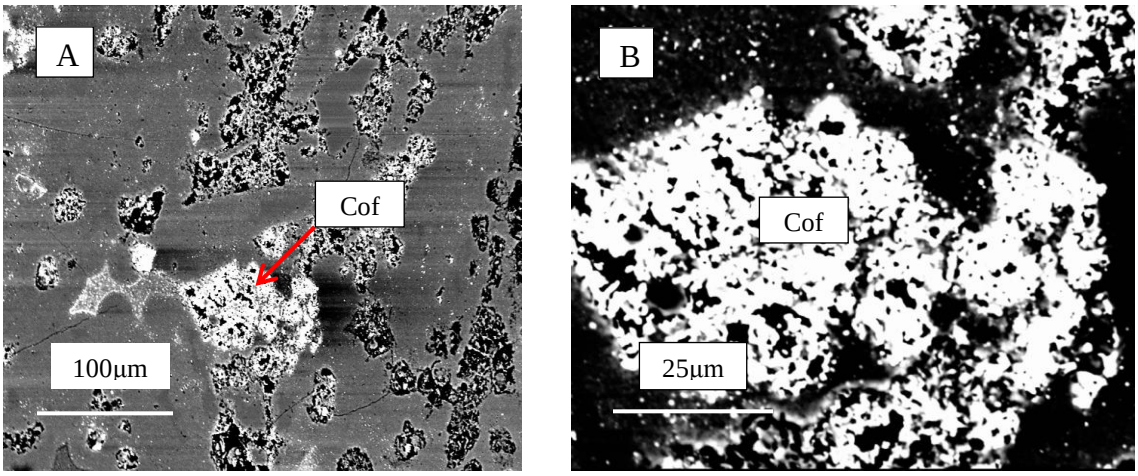

Figure 4-8: (A): BSE image of coffinite (Cof) within dissolution cavities of detrital quartz grain. Sample H161C-04. (B) High magnification BSE image of coffinite mineralization within dissolution cavity. Sample H161C-04.

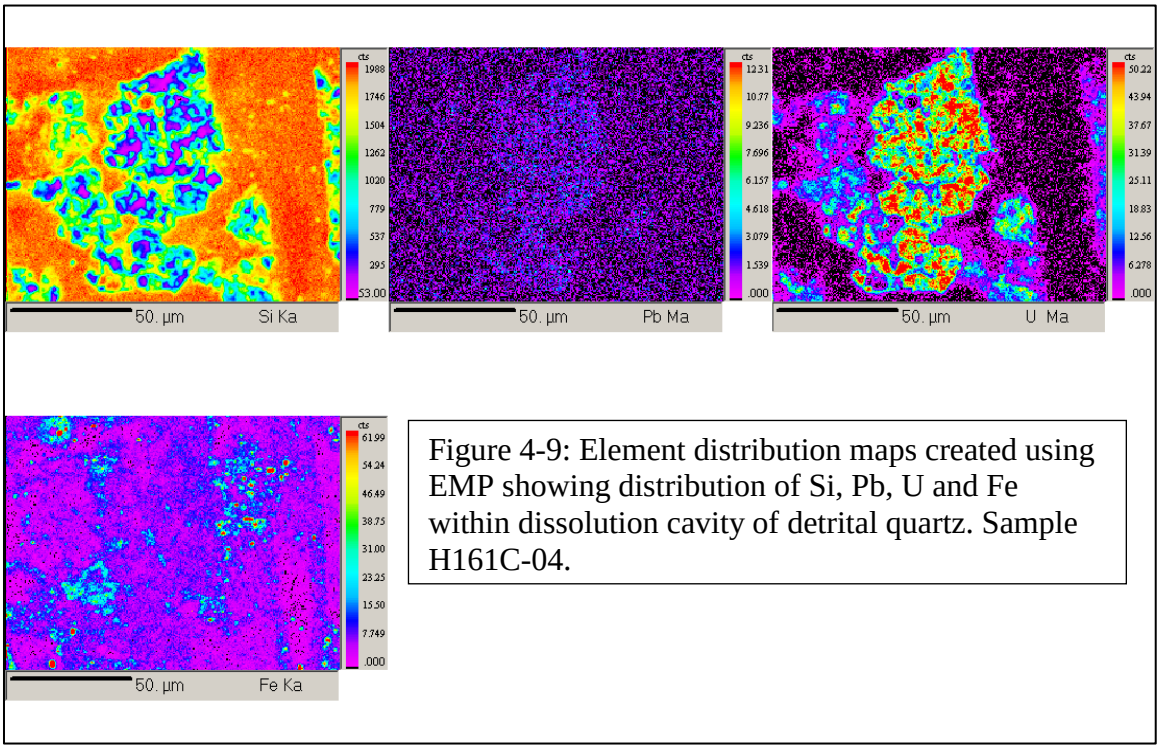

Figure 4-9: Element distribution maps created using EMP showing distribution of Si, Pb, U and Fe within dissolution cavity of detrital quartz. Sample H161C-04.

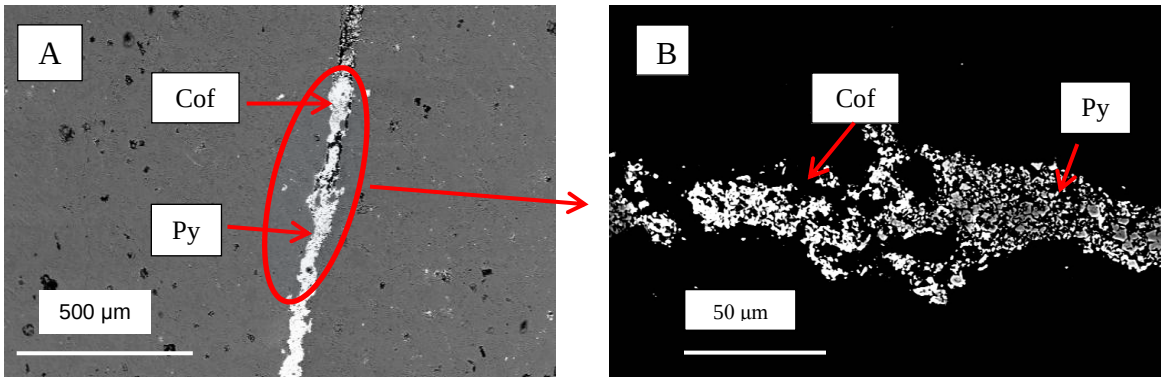

Figure 4-10: (A) BSE image of coffinite and pyrite mineralization within a microfracture of detrital quartz. Sample H161C-04. (B) High magnification BSE image of coffinite and pyrite mineralization within microfracture of detrital quartz. Sample H161C-04. (C) High magnification BSE image showing textural relations between coffinite and pyrite. Sample H161C-04.

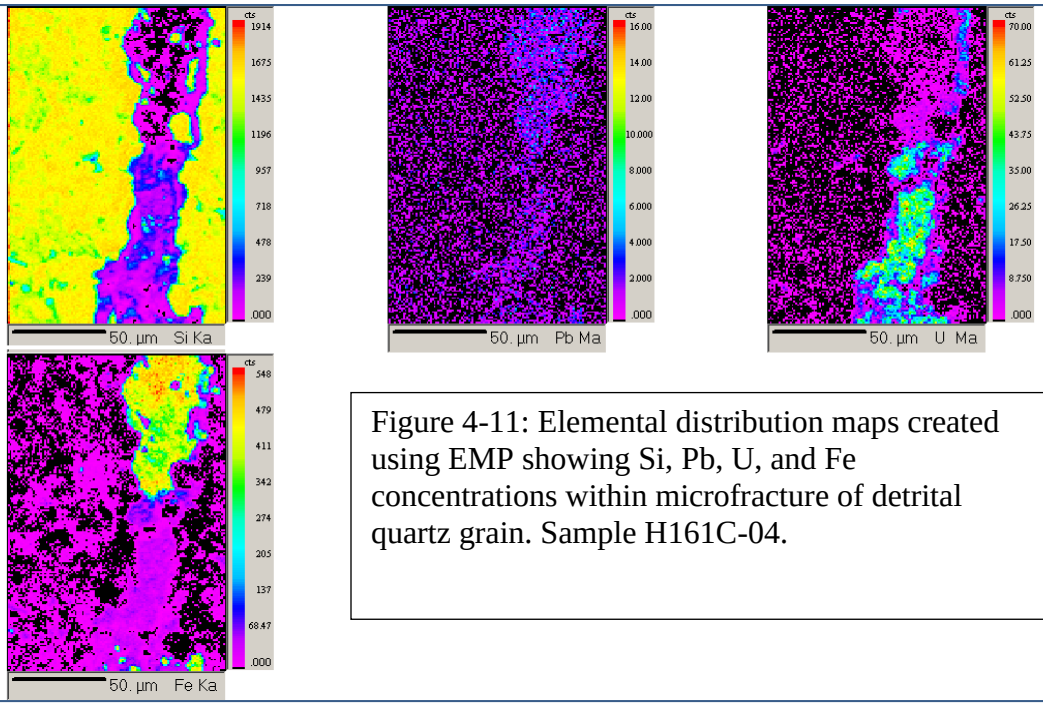

Figure 4-11: Elemental distribution maps created using EMP showing Si, Pb, U, and Fe concentrations within microfracture of detrital quartz grain. Sample H161C-04.

4.2.2.3 Sulphide and iron oxide minerals

The sulphide minerals in the Three Crow deposit consist of pyrite with trace marcasite and compose <1% of samples. Iron oxide minerals consist of hematite and compose < 2% of samples in the altered and mineralized zones. The sulphides and hematite are too fine-grained to be identified in hand sample; therefore, sulphide minerals were identified and characterized using reflected and transmitted light microscopy. In the distal altered zone (T797), finely crystalline hematite was identified using BSE imaging and EDS analysis, and occurs in trace amounts commonly with fine-grained pyrite inclusions. Disseminated, very fine-grained hematite also occurs within matrix clay minerals throughout samples from the distal altered to proximal altered zone. Laminated pyrite was identified in thin section T797-02 from the distal altered zone, where laminae are folded; <1mm thick and pyrite grains are highly fractured. The pyrite laminations are proximal, and are likely lithologically related to the underlying Pierre Shale Formation as noted in the preliminary drill logs (Hanly et al., 2009). In the proximal altered zone (H150C), hematite is disseminated within matrix clay minerals, whereas pyrite composes <1% of samples and is predominantly very fine- to medium-grained, subhedral to anhedral and interstitial to framework grains. In the mineralized zone (H161C), pyrite composes <2% of samples and occurs as three types: 1) fine-grained, subhedral pyrite (predominant); 2) clusters of very fine- to fine-grained framboids and 3) micron-sized blebs spatially associated with U mineralization. Sulphides in the proximal reduced zone (T792C) consist predominantly of fine- to very fine-grained pyrite framboids with minor fine- to medium-grained, subhedral pyrite and compose <2% of thin sections (Figure 4-12).

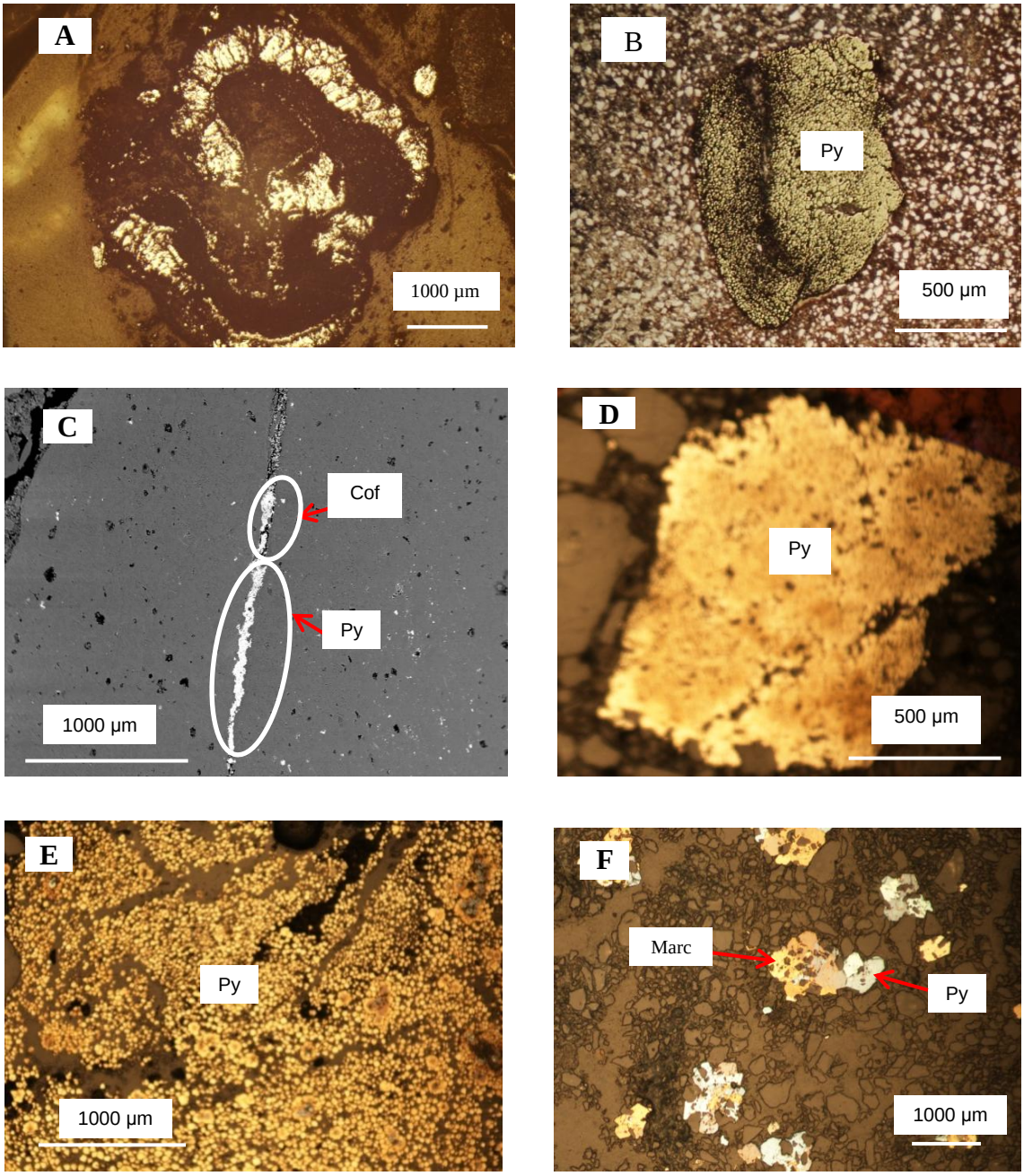

Figure 4-12: Reflected light and BSE images of different morphological types of pyrite from each zone of roll-front. A: pyrite laminae from distal altered zone T797; B: framboidal pyrite from proximal reduced zone H150C; C: pyrite associated with coffinite from mineralized zone H161C; D: framboidal pyrite from mineralized zone H161C; E: framboidal pyrite from proximal reduced zone T292C; F: pyrite and marcasite (Marc) from distal reduced zone T810C.

4.2.3 Chemical Pb ages and U-Th-Pb geochronology

Results from the electron microprobe analyses of type 1 coffinite from sample H161C-04 give chemical ages ranging from 2.1 to 13.0 Ma whereas type 2 coffinite is Pb deficient and therefore chemical ages could not be calculated (Appendix C).

The U-Th-Pb isotopic composition of type 1 and 2 coffinite from the Three Crow roll-front was determined using SIMS in order to calculate the ages of U mineralization. Because both types of coffinite mineralization are geologically young, the isotopic U-Pb method could not be used. The U-Th method of dating, which uses the activity ratios of $^{234}U/^{238}U$ and $^{230}Th/^{234}U$, was used to calculate the ages of coffinite. Type 1 coffinite gives ages that range from 23 Ka to 27 Ka ±3 Ka, whereas type 2 coffinite gives ages ranging from 194 to 205 Ka ± 30 Ka (Table 4, Appendix D).

Figure 4-13 shows the $^{234}U/^{238}U$ and $^{230}Th/^{234}U$ activity ratios (Table 5, Appendix D) using a model adapted from Scott et al. (1992). The data indicate that: 1) neither type 1 nor type 2 coffinite is in secular equilibrium, 2) both types are consistent with U accumulation and 3) some data plot within the forbidden zone, which indicates that U mineralization experienced U accumulation due to discontinuous processes (removal and addition). The increase in ^{234}U activity in nearly all of the samples may be due to the incorporation of dissolved ^{234}U in circulating groundwater that has been leached from nearby U sources (Faure, 1986).

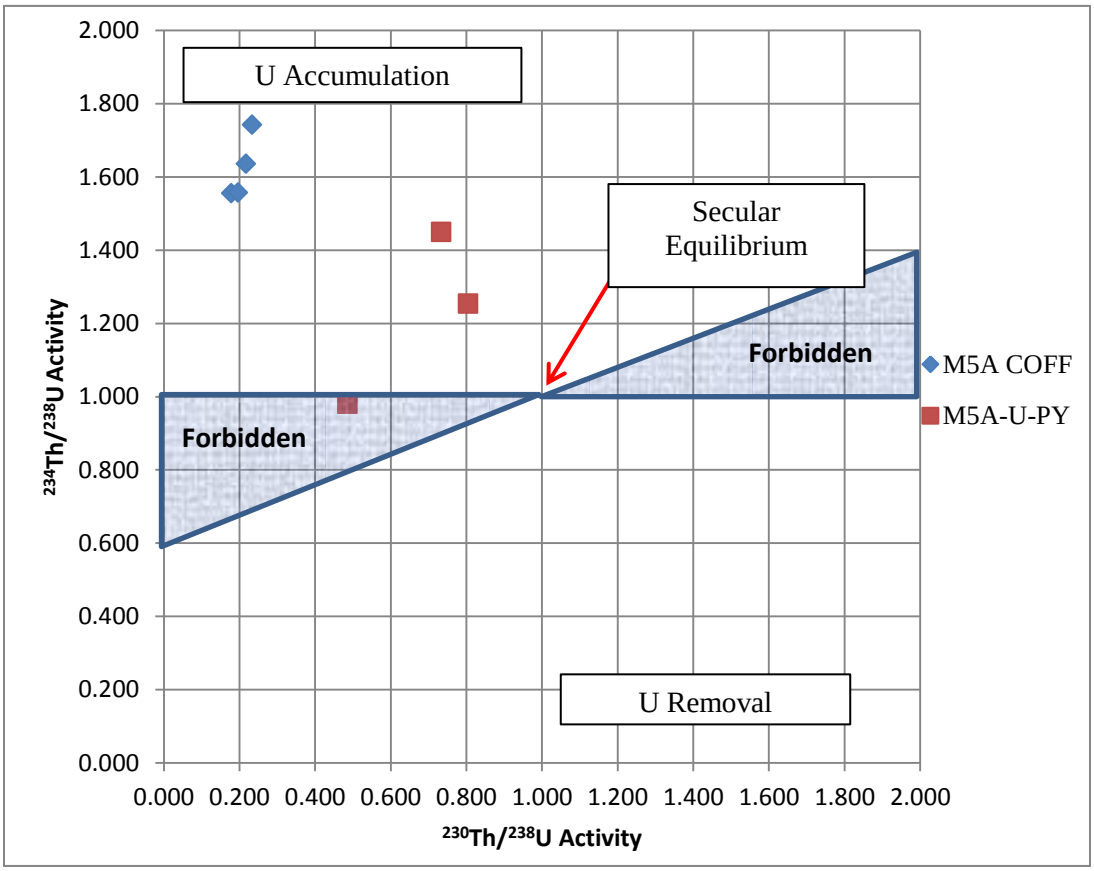

Figure 4-13: Disequilibrium plot showing the evolution of coffinite minerals from initial equilibrium during rock/water interactions in Three Crow deposit, Nebraska. Adapted from Scott et al. (1992).

4.2.4 Stable isotopes

A total of 55 analyses from the different zones of the Three Crow roll-front deposit (distal altered, proximal altered, mineralized, proximal reduced and reduced) were measured using SIMS (Table 5, Appendix D). The sample from the distal altered zone T797 (Figure 4-13A) consists of a pair of folded laminae composed of subhedral, fractured pyrite and yielded two sets of $\delta^{34}S$ values (-53 to -54‰ and -32 to -35‰), suggesting that there are two distinct generations of pyrite. A large, intensely fractured pyrite grain from the proximal altered zone (H150C; Figure 4-13B) produced variable

δ^{34}S values ranging from -12 and -50‰. Two different pyrite morphologies were analysed from the mineralized zone; the first comprises very fine-grained pyrite that is spatially associated with fine-grained coffinite crystals. This type has a wide range of δ^{34}S values, from -16 to -43‰, and pyrite becomes increasingly enriched in ^{32}S away from uranium (coffinite) mineralization (from top to bottom in Figure 4-13C). The second type of pyrite is a single pyrite grain composed of densely packed, very fine-grained framboids (Figure 4-13D) that have consistent δ^{34}S values ranging from -53 to -55‰. An aggregate of very fine- to fine-grained pyrite framboids from the proximal reduced zone T292C (Figure 4-13E) has δ^{34}S values between -27‰ and -62‰. Sulphide mineralization from the distal reduced zone (T810C; Figure 4-13F) consists of subhedral pyrite and marcasite; pyrite and marcasite were differentiated using reflected light microscopy. Spot analysis of pyrite yielded δ^{34}S values between -12‰ and -27‰, while the δ^{34}S values of marcasite range between -35‰ and -44‰.

Chapter 5. Discussion

5.1 Colorado tabular uranium-vanadium deposits

Until the mid-1950's, most workers considered the large, economic tabular deposits of Colorado and Utah as primary deposits although they were composed primarily of oxidized minerals. Today, however, after further exploration and large discoveries of "black ores", the primary, reduced U and V minerals are widely recognized as the precursors to these deposits. In this study, the petrographic evidence, EMP analyses and SIMS stable isotope data illustrate the relationship between primary and secondary U and V minerals, the evolution of which ultimately supports the widely accepted saline-brine model (Goldhaber et al., 1990; Northrop et al., 1990a; Sanford, 1990;). The crystallization of V-clays during the initial stages of deposit formation decreased the pH of the saline brine. Subsequently, dissolved uranyl compounds carried by late meteoric waters became unstable, leading to U adsorption onto quartz or clay minerals. The precipitation of primary U minerals is the result of biogenic reduction, and is either simultaneously reduced with sulphate by bacteria (Lovley et al., 1992), or reduced by biogenic H_2S generated by the metabolic processes of bacteria (Northrop et al., 1990b).

5.1.2 Primary and secondary ore minerals

The primary minerals are classified as reduced minerals and in the study area consist of the coffinite and montroseite. The source of V in V-clays has been speculated to be from the breakdown of Fe-Ti oxides (Northrop et al., 1990a; Wanty et al., 1990; Spirakis, 1996). Previous studies of Fe-Ti oxides in the San Juan Basin have shown that

they are an important reductant for the precipitation of U minerals and their alteration textures can provide insight on the formation of sandstone U deposits (Force et al., 2001). In this study, however, V-clays locally replace Fe-Ti oxides along fracture planes and along grain boundaries (Figure 4-3D). The breakdown of detrital Fe-Ti oxides resulted in the liberation of Fe and V, and subsequent incorporation of V into matrix clays and the formation of pyrite. The V-clays in the study area exhibit similar textures to those described by Breit (1995) as authigenic and locally contain significant concentrations of U. The direct precipitation of primary minerals such as montroseite from V-clays, as well as the adsorption of U onto V-clay minerals reflect the reducing nature of the V-clays. In samples from the JD-6 and JD-8 mines, U mineralization (coffinite) forms after V-clays as an alteration product in association with large aggregates (or "clasts") composed of very fine montroseite crystals and remnant quartz fragments. The source of silica during the formation of coffinite was likely detrital quartz grains or silica cement.

Although not petrographically observed in samples from this study, it has been previously established that montroseite and coffinite can oxidize to rauvite and finally to the more stable carnotite (Thamm et al., 1981). Secondary carnotite from the SM-18 mine appears texturally continuous with the ribbony, matrix V-clay laminations (Figures 4-2I), which is consistent with *in situ* alteration of the primary montroseite and coffinite. The evolution of the mineral parageneses can therefore be established from the petrographic evidence described in the preceding paragraphs: 1) the alteration of Fe-Ti oxides liberating V and Fe; 2) the incorporation of V into matrix clays and formation of sulphides; 3) the formation of V minerals (e.g., montroseite) and adsorption of U onto V-

clay minerals; 4) the formation of coffinite; 5) the oxidation of primary ore minerals montroseite and coffinite; and 6) the formation of secondary carnotite.

5.1.3 Ages of uranium mineralization

Chemical Pb ages were determined for primary and secondary minerals using EMPA. These data, however, cannot be used to discriminate between radiogenic and common lead, which is a primary factor affecting the accuracy of chemical Pb ages for all types of U mineralization. Chemical Pb ages calculated for type 1 U mineralization from the JD-6 mine range from 1.1 to 56.6 Ma. This variability is likely due to heterogeneous replacement textures and small crystal sizes, where spot analyses invariably include a mixture of montroseite and coffinite. Chemical Pb ages for type 2 carnotite mineralization from the SM-18 mine are relatively constrained, ranging from 0.3 to 5.7 Ma and represent secondary mineralization with preferential Pb loss, whereas the outlier chemical age of 71.1 Ma indicates a localized accumulation of lead. Type 3 coffinite mineralization associated with pyrite from the JD-9 mine has Pb levels below the detection limit and therefore chemical Pb ages could not be calculated. Chemical Pb ages for type 4 U minerals from the JD- 8 and SM-18 mines both represent complex intergrowth and textures between U and V-clay minerals in early stages of U mineral growth. Uranium minerals from the JD-9 mine are disseminated within V-clay cement and range from 0.6 to 5.3 Ma in age. The relatively constrained range of ages may be the result of localized Pb mobilization. The U minerals from the SM-18 mine are intergrown with V-clay within dense, ribbony laminations that are texturally continuous with altered

montroseite. The much older chemical Pb ages of 93.3 to 132.2 Ma are likely the result of Pb accumulation.

U-Pb isotopic ages were determined for primary and secondary minerals in order to constrain the approximate timing of mineralization. Previous studies have reported ages of U mineralization from the Plateau ranging from 22 to 215 Ma (Miller and Kulp, 1963). The only published $^{206}Pb/^{238}U$ ages of primary uraninite and coffinite in the Uravan district range between 65 to 90 Ma (Miller and Kulp, 1963), while previously reported Ra^{226}/U^{238} ages of carnotite and metatyuyamunite (sampled from joints and fractures) from Salt Wash ore in Colorado and Utah range from 10 to 120 Ka (Stern and Stieff, 1956). These ages suggest multiple mineralization events, which is consistent with the complex alteration textures of the ore zones in the Uravan area. In the present study, four stages of U mineralization were characterized and dated. Stage 1 coffinite and carnotite give ages of 34± 5 Ma and are associated with non-biogenic pyrite that has $\delta^{34}S$ values between -5 to -13‰. The much older ages of carnotite from this study, compared to the very young ages reported by Stern and Stieff (1956), may suggest that there is more than one generation of carnotite associated with the Colorado tabular U deposits. The samples analyzed in this study were from underground mineralized seams, having formed *in situ* from the alteration of primary minerals, whereas the carnotite analyzed by Stern and Stieff (1956) occurs along fractures and joints and likely represents late remobilization of U and V. Stage 2 U mineralization consists of coffinite texturally associated with pyrite, with an age of 22±3 Ma. The coffinite is associated with framboidal pyrite that has $\delta^{34}S$ values between -21 to -26‰. The textures and $\delta^{34}S$ values clearly suggest a biogenic origin for this pyrite. Stage 3 and 4 carnotite and coffinite give

ages of 11±3 Ma and 3±1 Ma, respectively. No sulphides appear to be associated with the stage 3 or 4 U minerals. The age range of U minerals suggests that mineralization was a continuous process that persisted during periods of optimal geological conditions. Only stage 2 U minerals are associated with biogenic pyrite and may have precipitated from biogenic reduction-oxidation reactions. Stage 1, 3 and 4 U minerals may have precipitated from localized, non-biogenic redox reactions.

The mathematical model shown in Figure 4-4 adapted from Scott et al. (1992) shows the activity ratios of the ^{238}U decay series along an alteration pathway during low-temperature rock-water interactions. The disequilibrium plot indicates that type 1 coffinite, type 2 carnotite and type 4 U minerals disseminated within V-clays are in secular equilibrium, whereas some type 4 U minerals associated with matrix V-clays plot in the second quadrant, indicating a net accumulation of U.

5.1.4 Sulphur isotopic analysis

The average $\delta^{34}S$ isotopic composition of subhedral and framboidal pyrite in mineralized samples from the study area is -40.9 ‰ and -29.7 ‰ respectively. These values are consistent with biological sulphate reduction and reflect a limited sulphate supply. In sample JD-6-2, pyrite spatially associated with coffinite mineralization gives considerably higher values with an average of -9.9‰ which represents either limited fractionation of sulphate from early, diagenetic pyrite, or chemical sulphate reduction The values are only slightly higher (i.e. isotopically heavier) than those that we would expect from a biologically formed sulphide deposit.

5.2 Three Crow roll-front, Nebraska

The geological setting of the Three Crow roll-front deposit is similar to those of the Crow Butte deposit in Nebraska and the Wyoming-type roll-fronts in that U mineralization occurs in the Tertiary host rocks at an oxidation-reduction boundary. In the Crow Butte deposit, coffinite occurs within the matrix as poorly developed, fine-grained (<2 mm) crystals (Hansley et al., 1984). Gjelsteen and Collings (1988) suggested that U mineralization in the Crow Butte deposit occurred soon after deposition of the Chadron Formation during maximum transmissivity of the host sediments and due to high permeability of overlying ash-rich beds and a change in groundwater flow direction during the Pliocene. The paragenesis of U minerals in the Three Crow deposit, however, cannot be determined from petrographic analysis alone as only trace amounts of very fine-grained coffinite (<2 μm) were identified in one sample from the mineralized zone. Coffinite occurs exclusively within dissolution cavities and microfractures in detrital quartz. The general scarcity of mineralization may simply reflect a poorly mineralized locale within a zone of U mineralization, a feature that has been noted in the Crow Butte deposit (Gjlesteen and Collings, 1988). Both the intimate textural relationship between pyrite and coffinite, and the isotopic composition of pyrite across the roll-front deposit suggest that pyrite is the principal reductant in the Three Crow roll-front. The sulphur isotopic composition of pyrite is consistent with biological reduction. Organic matter was not identified in samples examined in this study,; however, this lack of organic material has been noted in several economic deposits in Wyoming and may have been destroyed by oxidized groundwater fluids or consumed by sulphate-reducing bacteria (Hansley and Spirakis, 1992; Spirakis, 1996).

5.2.1 Ages of coffinite mineralization

The chemical Pb dating method is based on the assumption that all of the Pb in a U mineral is of radiogenic origin, and thus is generally considered an unreliable age dating method because of the possibility of the accumulation of either radiogenic or common Pb within the crystal structure of the mineral. Accordingly, the chemical Pb ages calculated for type 1 coffinite are highly variable, ranging from 1.1 to 56.6 Ma. In contrast, U-Pb-Th isotopic dating methods provide the most reliable ages by measuring the U decay series ratios directly. However, interpretation of isotopic dating results remains a difficult task due to the dynamics of natural systems, such as daughter gain or loss due to weathering and rock-water interactions (Faure, 1986). In previous studies of Wyoming-type roll-front deposits, U-Pb isotopic ages reported for uraninite range from 18 to 24 Ma (Dooley et al., 1974). Apparent radiogenic ages of 15.8 and 17.6 Ma from the nearby Crow Butte deposit (Gjelsteen, 1988) are the only published ages of U mineralization for Nebraska roll-front deposits to date. In this study, only one sample in the mineralized zone contains detectable U mineralization, which occurs as two distinct morphological types that are both associated with detrital quartz grains (described as type 1 and 2 coffinite in section 4.2.2.2). Using $^{230}Th/^{234}U$ disequilibrium dating methods, the isotopic ages of four very fine-grained coffinite crystals occurring within dissolution cavities of the detrital quartz grain were calculated and ranged from 23 to 27 Ka ±3 Ka. The dissolution cavities in the detrital quartz grain likely served as an effective "trap" for U adsorption and subsequent reduction. Two spot analyses of fine-grained coffinite crystals spatially associated with pyrite mineralization within a fracture in a detrital quartz grain (type 2 coffinite) each have variable $^{230}Th/^{234}U$ isotopic ratios, and give

much older ages of 193 and 205 Ka ±30 Ka. The differences in calculated ages between type 1 and 2 coffinite are likely the result of two separate episodes of mineralization.

5.2.3 Sulphur isotopic analysis

It is well established that roll-front U deposits have a definite relationship to sulphide minerals (IAEA, 2009). Previous sulphur isotopic studies describe distinct isotopic trends, and interpret the mechanism of reduction as either chemical or biological, across roll-front deposits in Wyoming (Austin, 1970; Warren, 1972; Reynolds and Goldhaber, 1983). The isotopic sulphur composition of pyrite generally reflects the shift from an open, oxygenated environment to a system depleted of dissolved oxygen with an increasingly limited sulphur supply. In this study, the isotopic sulphur composition of sulphides reflects the structure of the roll-front. Although the formation and distribution of sulphides occur independently from U mineralization, their existence is essential to the formation of U deposits, and sulphur isotopes may serve as a potential exploration tool to delineate and map roll-front deposits.

5.2.3.1 Biogenic sulphur reduction

Dissimilatory sulphate-reducing bacteria couple the reduction of U^{6+} with the oxidation of carbon or H_2S, and it has been shown experimentally that not only are sulphate and U^{6+} reduced simultaneously, but enzymatic (i.e. biogenic) reduction of U^{6+} is more efficient than non-enzymatic (i.e. chemical) reduction by sulphides. The fact that ore-stage pyrite and pre-ore pyrite are undistinguishable in hand specimen is problematic. The most reliable method in identifying different sulphide generations is to measure the $\delta^{34}S$ values. *In situ* micro-analytical techniques, such as that used in this study, provide

the most accurate results. Sulphur isotopic data from previous studies of Wyoming-type roll-front deposits, however, are based on the bulk chemical analysis of sulphides. In general, if the pyrite is of biogenic origin, and thus considered to have precipitated during ore formation stages, the $\delta^{34}S$ values of pyrite will be below -10‰ (isotopically light), and theoretically, could reach values as low as -75‰ following disproportionation during multiple oxidation-reduction cycles (Farquhar et al., 2003). Sulphur isotopic compositions of sulphide minerals from a Shirley Basin roll-front deposit in Wyoming range from -32.7 to +18.8‰ and represent increasing ^{34}S enrichment across the deposit relative to the assumed $\delta^{34}S$ value of pre-ore pyrite of ~ -17 to -20 ‰ (Warren, 1972). The two biogenic models proposed by Warren (1972) consider the sulphur isotopic trend across the roll-fronts, where ^{34}S is enriched downstream in the deposit and the isotopic composition of pyrite across the deposit is controlled by ore stage pyrite. Outside the deposit, the isotopic composition of pyrite is controlled by pre-ore stage pyrite. The sulphide deposits form as groundwater moves through the roll-front deposit and sulphate is reduced and the precipitating sulphide incorporates the lighter isotope, leaving the remaining dissolved sulphate enriched in ^{34}S to form pyrite increasingly enriched in heavy S. The two biogenic models for the formation of sulphide deposits described by Warren (1972) are: (1) the quantitative reconstitution model, which requires complete conversion of dissolved sulphate to pyrite, and (2) the steady-state model, which requires only partial re-precipitation of sulphur as pyrite. The conditions necessary for the complete conversion of dissolved sulphate to pyrite described in the quantitative reconstitution model are relatively rare in nature as some sulphur will be lost due to precipitation inefficiency of the precipitation process (eg., low dissolved oxygen and

sulphur concentrations of migrating ore fluids). The sulphur isotopic trends across a theoretical roll-front deposit for the quantitative reconstitution model and steady-state model are shown in Figures 5-1 and 5-2, respectively. The trends are not readily applicable to every sulphide deposit; Austin (1970) completed systematic sampling and isotopic analysis of sulphides across four Wyoming roll-fronts, where only one of three deposits produced an ideal fractionation pattern. The distribution of sulphides is strongly dependent on both amount of dissolved oxygen in groundwater and pre-ore content of host sediments (eg., amount of reduced or oxidized minerals); other variables include a flow-rate of groundwater, buffering capacity of host sediments, and Se content (Granger and Warren, 1972; 1978). The sulphur isotopic composition of pyrite from the mineralized zone to the distal reduced zone of the Three Crow deposit ranges from -54.2 to -20.2‰. This isotopic trend (Figure 5-3), is not similar to either the quantitative (Figure 5-1) or steady-state models (Figure 5-2) and may be attributed in part to the limited data set. However, the isotopic composition of pyrite downstream from the oxidation front reflects the basic principle described in the steady-state model of gradual ^{34}S enrichment approaching pre-ore isotopic values of pyrite, in contrast to a more abrupt enrichment and subsequent depletion of ^{34}S shown by the isotopic trend in the quantitative reconstitution model.

The isotopic values reported in previous studies (Austin, 1970; Warren, 1972) are based on whole-rock analyses; the $\delta^{34}S$ values of sulphides from the Three Crow deposit are reported as the average of each data set from the mineralized, proximal reduced and distal reduced zones of the deposit. The ranges and average $\delta^{34}S$ values of sulphides from the five zones of the Three Crow roll-front deposit are shown in Figure 5-4. Multiple

sulphide generations of pyrite within the study area suggest a migrating front. The $\delta^{34}S$ values of two superimposed pyrite laminae from the distal, altered zone (T797C) indicate two distinct generations of pyrite with consistent values averaging -53‰ and -34‰ respectively. The $\delta^{34}S$ values of pyrite from the proximal, altered zone (H150C) are also within the range from -12 to -50‰, with an average of -26‰; variability is most likely due to localized and incomplete reactions during precipitation. Two morphological types of pyrite from the mineralized zone (H161C) were analyzed: 1) a single, intensely fractured pyrite grain with consistent $\delta^{34}S$ values averaging -55‰, and 2) pyrite spatially associated with coffinite within a micro-fracture in a detrital quartz grain. This pyrite gives $\delta^{34}S$ values that become increasingly heavier away from coffinite mineralization, the lowest value being -46‰ near the contact between pyrite and coffinite, and the highest -16‰ near the outer edge of the fracture and far from coffinite. The shift in $\delta^{34}S$ values is most likely due to a gradual depletion in sulphur within a localized closed system (i.e. the fracture). The textural relationship between coffinite and pyrite suggests that two minerals were contemporaneous. The $\delta^{34}S$ values measured for samples from the proximal reduced zone (T792C) are variable with an average of -52‰; these values are slightly higher than those predicted using the steady-state model and may represent a migrating front with re-oxidation accompanied by further fractionation, disproportionation and re-precipitation of ^{34}S-depleted sulphides. The $\delta^{34}S$ values for samples from the distal reduced zone, consisting of spatially associated pyrite and marcasite average -37.8 ‰ for marcasite and -20.2 ‰ for pyrite. The two minerals represent separate sulphide generations and also a shift in geochemical conditions. Because the precipitation of marcasite occurs at lower pH values than pyrite, it is likely

that these minerals precipitated from chemically distinct ore fluids. Geochemical studies by Stanton and Goldhaber (1991) and Reynolds and Goldhaber (1983) concluded that the formation of marcasite is largely a function of pH. Jensen (1958) concluded that there is no covariant relationship between sulphide species and $\delta^{34}S$, which is consistent with the results from the present study.

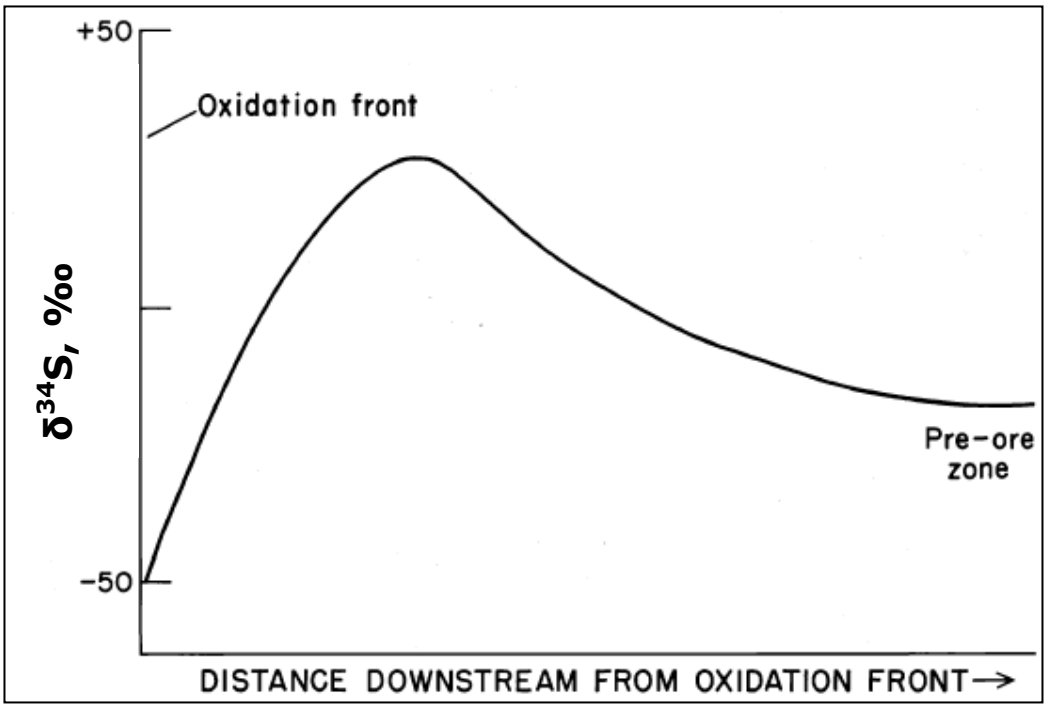

Figure 5-1: Isotopic sulphur trend described in the quantitative reconstitution model showing the sulphur isotopic composition of pyrite versus distance downstream. After Warren (1972).

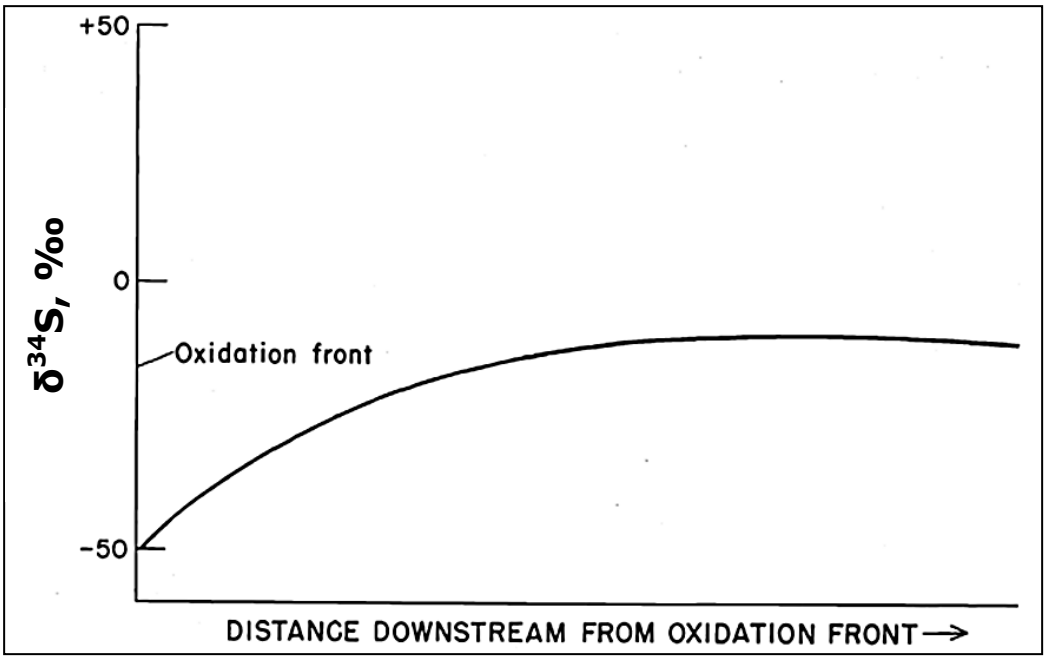

Figure 5-2: ideal isotopic sulphur trend predicted for the steady-state model showing the sulphur isotopic composition of pyrite versus distance downstream. After Warren (1972).

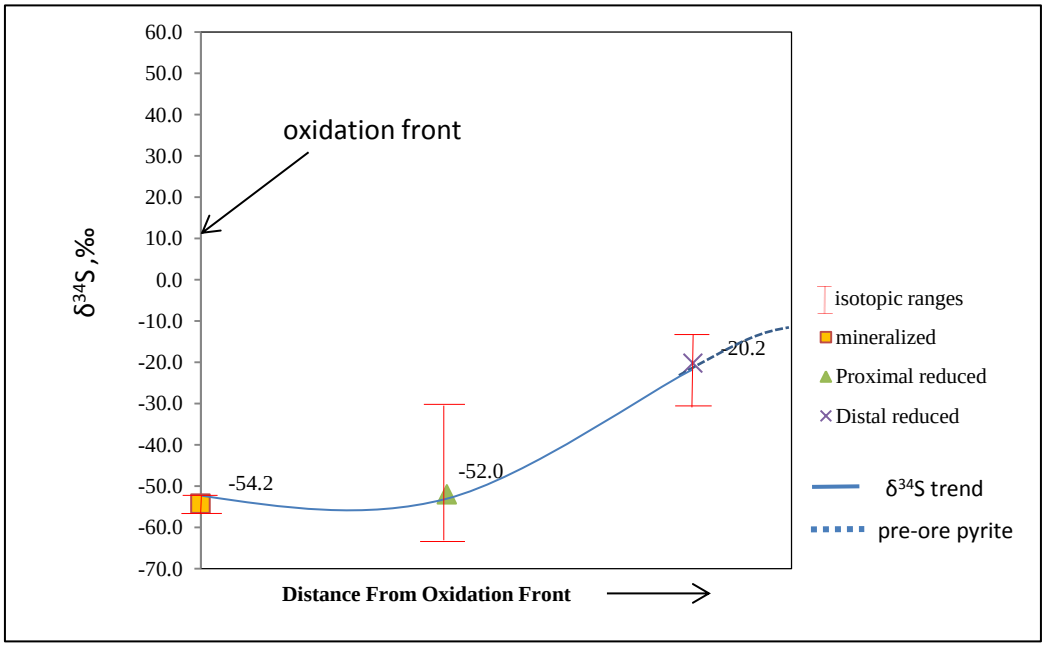

Figure 5-3: Average isotopic sulphur trend of pyrite from Three Crow deposit. Mineralized zone to distal altered zone overall trend shows the enrichment of ^{34}S in pyrite approaching pre-ore values with increasing distance from oxidation front. (Actual distances of the drill holes are approximate because they were not reported in Hanly et al, 2009 and are most likely proprietary).

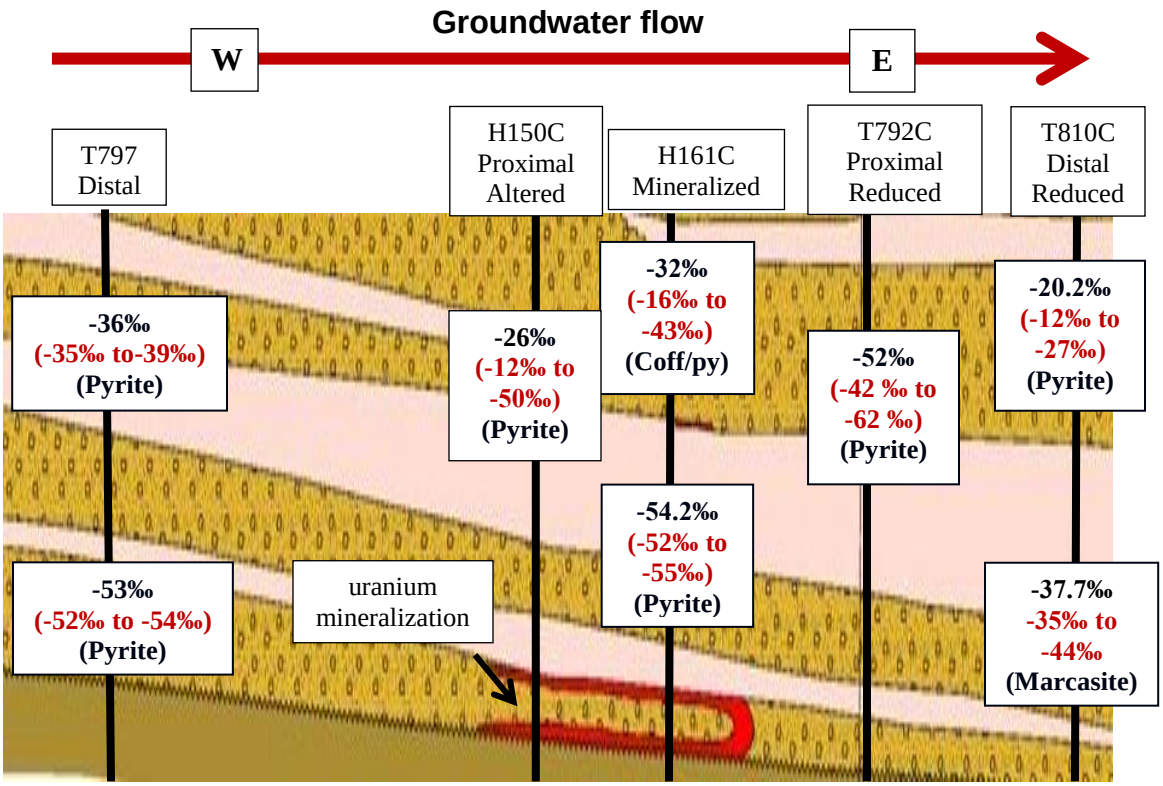

Figure 5-4: $\delta^{34}S$ composition of sulphides across five drill holes intersecting the Three Crow roll-front. Modified after Hanly et al. (2009).

Chapter 6: Conclusions

The Wyoming-type roll-front and Colorado Plateau tabular deposits are the principal resources for uranium in the U.S. Both types occur within continental sediments, have similar element and mineral associations and are formed as the result of the same basic mechanism of reduction from soluble U^{6+} to insoluble U^{4+}. The differences between the two types of deposits, however, greatly outnumber the similarities with respect to ore mineralogy, distribution and morphology of ore-bodies, alteration, and nature of ore deposition.

The tabular deposits in the Uravan region occur within the sediments of the Jurassic Morrison Formation and are characterized by anomalous concentrations of V with accessory U; intense alteration of primary deposits led to localization of U and V into the more stable, oxidized deposits. In the study area, primary U and V minerals such as coffinite and montroseite are localized in sedimentary packages composed of black, mineralized laminae and barren sandstone intervals that are concordant to bedding, and occur entirely within reduced sediments. The secondary carnotite deposits occur as disseminated grains in mineralized seams from in situ alteration of primary minerals, and also as massive, remobilized mineralization confined to fractures and joints. The formation of primary deposits is the result of a series of sequential geochemical reactions at an interface between lower dense, saline brines and upper, permeating meteoric waters, the latter having interacted with the overlying altered ash beds and having high pH values. The V-clay minerals of the tabular Colorado deposits are considered to be the primary vanadium source; in this study V-clays were identified as vanadium-rich illite and vanadium-rich chlorite. The V-clays that occur within cell lumens of organic matter

were likely deposited before compaction and support an authigenic origin. Evidence from this study showing montroseite, with local coffinite alteration, precipitating from within matrix V-clays suggests the reducing nature of V-clays; early formation of V-clays plays a crucial role in lowering the pH of the brine, causing dissolved U in groundwater to become unstable and adsorb onto clay minerals or quartz. Once adsorbed, coffinite was precipitated in the presence of biogenically precipitated aqueous sulphides within the saline brine; *in situ* isotopic sulphur values of pyrite from this study are consistent with biological sulphate reduction.

Four stages of uranium mineralization were identified in the Colorado deposits: 1) coffinite and carnotite, 2) coffinite texturally associated with pyrite, 3) matrix-replacing carnotite and 4) coffinite precipitating from V-clay cement. The isotopic sulphur composition of pyrite from mineralized samples from the study area is consistent with biological sulphate reduction, with the exception of one occurrence of pyrite associated with stage 1 coffinite and montroseite, which likely precipitated by inorganic chemical processes. Carnotite is considered to have developed at the expense of primary coffinite and montroseite *in situ* and occurs very proximal to, and continuous with, the primary ore minerals and V-clays. Stage 1 coffinite and carnotite give ages of 34± 5 Ma, stage 2 coffinite gives an age of 22±3 Ma, whereas stage 3 and 4 carnotite and coffinite give an age of 11±3 Ma and 3±1 Ma, respectively. The variation of ages and types of U mineralization associated with the tabular-type deposits in Colorado suggests that these deposits have had a complex and protracted fluid history.

.

The large roll-type U ore deposits of Nebraska and Wyoming were deposited from the early to mid-Miocene, and occur in highly arkosic and unconsolidated sediments within intracratonic basins. Typical Wyoming-type roll-fronts are characterized by a relatively sharp, crescent-shaped interface between oxidized and reduced sediments along which U minerals are precipitated and are consistently associated with supergene sulphide deposits. An abrupt change in Eh causes dissolved uranium (U^{6+}) in percolating ore fluids to become unstable, adsorb onto quartz (or other surfaces) and finally precipitate. Bacterial sulphate reduction in sandstones that contain vegetal matter, which acts as an energy source for bacteria, serves as an efficient catalyst and extends the reducing environment over larger areas, compared to inorganic chemical sulphate reduction, due to the migration of H_2S; iron oxides are readily transformed to pyrite, thereby adding to the reducing capacity of the rocks. Sulphur isotope values of sulphides across the Three Crow deposit follow the biogenic isotopic model first described by Austin (1970) and Warren (1972), where pyrite along the oxidation front shows the maximum ^{32}S enrichment, and values become progressively heavier, approaching pre-ore sulphide values with increasing distance downstream. Shifts within the geochemical system are reflected by the occurrence of marcasite with pyrite, and evolved oxidation fronts are implied by multiple sulphide generations as indicated by their $\delta^{34}S$ compositions.

Petrographic and stable isotope data from the Three Crow study area suggest that the deposit was formed by similar processes as those described for Wyoming-type roll-fronts. The $^{230}Th/^{234}U$ isotopic ages of coffinite from the Three Crow roll-front deposit range from 23 to 27 ± 3 Ka, representing mineralization that occurs within dissolution

cavities in quartz, and 193 to 205 ±30 Ka for coffinite associated with pyrite within a fracture in a single detrital quartz grain. The two sets of ages for coffinite mineralization suggest two distinct generations of U mineralization. The mineralized samples for this study were obtained from the limbs of the roll-front (rather than the nose) and the U-Th activity ratios plot within the U accumulation quadrant, which suggests that the limbs are gaining U. Therefore, *in situ* U-Th micro-analysis of U minerals by SIMS can be used to determine whether a roll-front U deposit is moving (i.e. U-Th activity ratios plot in the U removal quadrant) or being formed (i.e. U-Th activity ratios plot in the U accumulation quadrant).

References

Austin, S.R. (1970): Some patterns of sulfur isotope distribution in uranium deposits. Earth Science Bulletin, **3**, no. 2., pages 5-22.

Barthelmy, D. (2014): *http://webmineral.com*

Berman, A., Poleschook, D. and Dimelow, T. (1980): Jurassic and Cretaceous systems, H.C. Kent and W. Porter, eds. Colorado Geology: RMAG, 258 pages.

Bopp IV, C.J., Lundstrom, C.C., Johnson, Glessner, J. (2009): Variations in $^{238}U/^{235}U$ in uranium ore deposits: isotopic signatures of the U reduction process? Geology, **37**, pages 611-614.

Bowles, J. (1990): Age dating of individual grains of uraninite in rocks from electron microprobe analyses. Chemical Geology, **83**, pages 47-53.

Blakey, R. (2011): Geology of the Colorado Plateau and Global and Regional Paleogeography, http://jan.ucc.nau.edu/rcb7/index.html.

Bradshaw, R.W. and Kowallis, B.J (2010): U-Pb dating of zircons from the Salt Wash Member of the Morrison Formation from near Capitol Reef National Park, Utah in Rocky Mountain 62nd Annual Meeting, April 2010, Paper no. 11-6.

Breit, G.N. (1995): Origin of clay minerals associated with V-U deposits in the Entrada Sandstone, Placerville Mining District, southwestern Colorado. Economic Geology, **90**, pages 407-419.

Brunner, B. and Bernasconi, S.M. (2005): A revised isotope fractionation model for dissmilatory sulfate reduction in sulfate reducing bacteria. Geochimica et Cosmochimica Acta, **69**, no. 20, pages 4759-4771.

Carlson, M.P. (1999): Transcontinental Arch — a pattern formed by rejuvenation of local features across central North America. Tectonophysics, **305**, pages 225–233.

Chenoweth, W.L., Epis, R.C., Callender, J.F. (1981): The uranium-vanadium deposits of the Uravan mineral belt and adjacent areas, Colorado and Utah. Guidebook - New Mexico Geological Society, **32**, pages 165-170.

Collings, S.P. and Knode, R. H. (1984): Geology and discovery of the Crow Butte uranium deposit, Dawes County, Nebraska. Annual Symposium on Uranium and Precious Metals, **7**, pages 5-14.

Cuney, M. (2009): The extreme diversity of uranium deposits. Minera Deposita, **44**, pages 3-9.

Currie, B.S. (1998): Upper Jurassic-lower Cretaceous Morrison and Cedar Mountain formations, NE Utah-NW Colorado; relationships between non-marine deposition and early cordilleran foreland-basin development. Journal of Sedimentary Research, **68** (4), pages 632-652.

Dahlkamp, F.J. (1993): Uranium ore deposits. Berlin, Federal Republic of Germany: Springer-Verlag, Berlin, 460 pages.

Dickinson, K.A. (1991): Uranium and diagenesis in evaporitic lacustrine mudstone of the Oligocene White River Group, Dawes County, Nebraska. U.S. Geological Survey Bulletin 1956, 25 pages.

Doelling, H.H. (1985): Geology of Arches National Park. Utah Geological and Mineral Survey Map 74, scale 1:50000.

Dooley, J.R., Harshman, E.N. and Rosholt, J.N. (1974): Uranium-lead ages of the uranium deposits of the Gas Hills and Shirley Basin, Wyoming. Economic Geology, **69**, pages 527-531.

Dunham, R.J. (1961): Geology of uranium in the Chadron area, Nebraska and South Dakota. U.S Geological Survey Open File Report, pages 61-42.

Farquhar, J., Johnston, D.T., Wing, B.A., Habicht, K.S., Canfield, D.E., Airieau, S., Thiemens, M.H. (2003): Multiple sulphur isotopic interpretations of biosynthetic pathways: implications for biological signatures in the sulphur isotope record. Geobiology, **1**, pages 27-36.

Faure, G. (1986): Principles of isotope geology. 2nd Edition, 589 pages.

Fayek, M., Harrison, T.M., Grove, M., Coath, C.D. (2000): A rapid in situ method for determining the ages of uranium oxide minerals: evolution of the Cigar Lake deposit, Athabasca Basin. International Geology Review, **42**, pages 163-171.

Fayek, M. and Kyser, K. (1999): Stable isotope geochemistry of uranium deposits. Reviews in Mineralogy, **38**, pages 181-220.

Finch, W.I. (1996): Uranium provinces of North America-Their definition, distribution, and models. U.S. Geological Survey Bulletin 2141, p. 24.

Fischer, R.P. (1970): Similarities, differences, and some genetic problems of the Wyoming and Colorado Plateau types of uranium deposits in sandstone. Economic Geology, **65**, pages 778-784.

Fischer, R.P. and Hilpert, L.S. (1952): Geology of the Uravan Mineral Belt. Geological Survey Bulletin 988-A, 13 pages.

Fischer, R.P. and Stewart, J.H. (1961): Copper, vanadium, and uranium deposits in sandstone-their distribution and geochemical cycles. Economic Geology, **56**, pages 509-520.

Force, E.R., Butler, R.F., Reynolds, R.L., Houston, R.S. (2001): Magnetite ilmenite-hematite detritus in Mesozoic-Tertiary placer sandstone-hosted uranium deposits of the Rocky Mountains. Economic Geology, **96**, pages 1445-1453.

Gjelsteen, T.W. (1988): Origin and timing of uranium mineralization in the Chadron Formation, Northwest Nebraska. Unpublished MSc thesis, University of Wyoming, 92 pages

Gjelsteen, T.W. and Collings, S.P. (1988): Relationship between groundwater flow and uranium mineralization in the Chadron Formation, Northwest Nebraska. Wyoming Geological Association Guidebook, 39th Field Conference, pages 271-284.

Goldhaber, M.B., Hemingway, B.S., Mohagheghi, A., Reynolds, R.L., Northrop, H.R. (1987): Origin of coffinite in sedimentary rocks by a sequential adsorption-reduction mechanism. Bulletin Mineralogie, **110**, pages 131-144.

Goldhaber, M.B. Reynolds, R.L. Campbell, J.A, Wanty, R.B., Grauch, R.I., Northrop, R (1990): Part II. Mechanisms of ore and gangue mineral formation at the interface between brine and meteoric water minerals. Northrop, H.R., Goldhaber, M.B., Editors, Genesis of the tabular-type vanadium-uranium deposits of the Henry Basin, Utah. Economic Geology, **85**, no. 2, pages 236-250.

Granger, H.C. and Warren, C.G. (1969): Unstable sulphur compounds and the origin of roll-type uranium deposits. Economic Geology, 64, pages 160-171.

Granger, H.C. and Warren, C.G (1974): Zoning in the altered tongue associated with roll-type uranium deposits. Formation of uranium ore deposits. IAEA, 1974, pages 185-200.

Granger, H.C. and Warren, C.G. (1978): Some speculations on the genetic geochemistry and hydrology of roll-type uranium deposits. Wyoming Geological Association Guidebook, 30th Annual Field Conference, pages 349-361.

Granger, H.C. and Warren, C.G. (1979): The importance of dissolved free oxygen during formation of sandstone-type uranium deposits. U.S. Geological Survey Open-File Report. 79-1603, pages 1-22.

Gruner, J.W. (1956): Concentration of uranium in sediments by multiple migration-accretion. Economic Geology, **51**, no. 6, pages 495-517.

Hanly, A, Fiolleau, K., Adams, D. (2009): Sandstone-hosted uranium study at Three Crow, Nebraska; unpublished company report, Cameco Resources Inc, 23 pages.

Hansley, P.L, Collings, S.P., Skipp, G.L. (1984): Mineralogy of uranium ore from the Crow Butte uranium deposit, Oligocene Chadron Formation, Northwestern Nebraska. U.S. Geological Survey Open-File Report, 89-225.

Hansley, P.L. and Spirakis, C.S. (1992): Organic matter diagenesis as the key to a unifying theory for the genesis of tabular uranium-vanadium deposits in the Morrison Formation, Colorado Plateau. Economic Geology, **87**, pages 352-365.

Harshman, E.N. (1966): Genetic implications of some elements associated with uranium deposits, Shirley Basin, Wyoming. U.S. Geological Survey Professional Paper 550-C, pages 167-173.

Harshman, E.N. (1972): Geology and uranium deposits, Shirley Basin area, Wyoming. U.S. Geological Survey Professional Paper 745, **82**, pages 1-75.

Harshman, E. N. (1974). Distribution of elements in some roll-type uranium deposits. Proceedings Series - International Atomic Energy Agency. STI/PUB/374, pages 169-183.

Hess, F.L. (1923): New and known minerals from the Utah-Colorado carnotite region. U.S.G.S. Bulletin 750. Contributions to Economic Geology, 1923-1924, Part 1, 16 pages. Hobday, D.K. and Galloway, W.E. (1999): Groundwater processes and sedimentary uranium deposits. Hydrogeology Journal, **7**, pages 127-138.

Holliger, P., and Cathelineau, M. (1988): In situ U-Pb age determination by secondary ion mass spectrometry. Chemical Geology, **70**, 173 pages.

IAEA (2009): World distribution of uranium deposits (UDEPO) with uranium deposit classification. IAEA-Tecdoc 1629, 117 pages

Jensen, M.L. (1958): Sulfur isotopes and the origin of sandstone-type uranium deposits. Economic Geology, **53**, pages 598-616.

Johnston, D.T., Farquhar, J., Canfield, D.E. (2007): Sulfur isotope insights into microbial sulfate reduction: When microbes meet models. Geochimica et Cosmochimica Acta, **71**, pages 3929-3947.

Kyser, K., and Cuney, M., 2009, Sandstone-hosted uranium deposits. Recent and not-so-recent developments in uranium deposits and implications for exploration, M. Cuney and K. Kyser, Editors. Mineralogical Association of Canada, Short Course Series **39**, pages 161-220.

Leventhal, J.S., Santos, E.S. (1981): Relative importance of organic carbon and sulfide sulfur in a Wyoming roll-type uranium deposit. U.S. Geological Survey Open File Report 81-580, 14 pages

Lovley, D.R. and Phillips, E.P. (1992): Reduction of uranium by Desulfovibrio desulfuricans. Applied and Environmental Microbiology, **58**, no. 3, pages 850-856.

Ludwig, K. (1993): Isoplot: Excel based program for plotting radiogenic isotopes. U.S. Geological Survey, Open File Report 91-445, pages 1-42

Ludwig, K.R. (1978): Uranium-daughter migration and U/Pb isotope apparent ages of uranium ores, Shirley Basin, Wyoming. Economic Geology, **73**, pages 20-49.

Meunier, J.D. (1994): The composition and origin of V-rich clay minerals in Colorado plateau Jurassic sandstones. Clays and Clay Minerals, **42**, no. 4, pages 391-401.

Miller, D.S. and Kulp, L.J. (1963): Isotopic evidence on the origin of the Colorado Plateau uranium ores. Geological Society of America Bulletin, **74**, pages 609-630.

Mohagheghi, A., Updegraff, D.M., Goldhaber, M.B. (1984): The role of sulfate-reducing bacteria in the deposition of sedimentary uranium ores. Geomicrobiology Journal, **4**, no.2, pages 153-173.

Nash, J.T., Granger, H.C., Adams, S.S. (1981): Geology and concepts of genesis of important types of uranium deposits. Economic Geology, 75th Anniversary Volume, pages 63-116.

Northrop, H.R., Goldhaber, M.B., Landis, G.P., Unruh, J.W. (1990a): Part I: Geochemical and mineralogical evidence for the sources of the ore-forming fluids minerals in Northrop, H.R., Goldhaber, M.B., Editors. Genesis of the tabular-type vanadium-uranium deposits of the Henry Basin, Utah. Economic Geology, **85**, no. 2, pages 215-236.

Northrop, H.R., Goldhaber, M.B., Whitney, G., Landis. G.P. Rye, R.O. (1990b): Part III: Evidence from the mineralogy and geochemistry of clay minerals in Northrop, H.R., Goldhaber, M.B., Editors. Genesis of the tabular-type vanadium-uranium deposits of the Henry Basin, Utah. Economic Geology, **85**, no. 2, pages 250-269.

Reynolds, R.L. and Goldhaber, M.B. (1978): Iron-titanium oxide minerals and associated alteration phases in some uranium-bearing sandstones. Journal of Research, U.S. Geological Survey, pages 707-714.

Reynolds, R.L. and Goldhaber, M.B. (1983): Iron disulfide minerals and the genesis of roll-type uranium deposits. Economic Geology, **78**, pages 105-120.

Riciputi, L.R., Peterson, B.A., and Ripperdan, R.L. (1998): Measurement of light stable isotope ratios by SIMS: Matrix effects for oxygen, carbon, and sulfur isotopes in minerals: International Journal of Mass Spectrometry and Ion Processes, **178**, pages 81-112.

Sanford, R.F. (1992): A new model for tabular-type uranium deposits. Economic Geology, **87**, pages 2041-2055.

Sanford, R.F. (1994): A quantitative model of ground-water flow during formation of tabular sandstone uranium deposits. Economic Geology, **89**, pages 341-360.

Scott, R.D., MacKenzie, A.B., Alexander, W.R. (1992): The interpretation of ^{238}U-^{234}U-^{230}Th-^{226}Ra disequilibria produced by rock-water interactions. Journal of Geochemical Exploration, **45**, pages 323-343.

Shawe, D.R. (1976): Sedimentary rock alteration in the Slick Rock district, San Miguel and Dolores Counties, Colorado. U.S. Geological Survey Professional Paper 576-D, 51 pages.

Sibray, S.S. (2010): Revised White River Group stratigraphy and uranium mineralization in the Nebraska Panhandle, abs. Rocky Mountain Section Meeting, AAPG, June 2010.

Singler, C.R. and Picard, D.M. (1979): Petrography of White River Group (Oligocene) in northwest Nebraska and adjacent Wyoming. Contributions to Geology, **18**, no.1, pages 51-67.

Southam, G. (2012): Minerals as substrates for life: the Prokaryotic view. Elements, **8**, no. 2, pages 101-106.

Spirakis, C.S. (1996): The roles of organic matter in the formation of uranium deposits in sedimentary rocks. Ore Geology Reviews, **11**, pages 53-69.

Spirakis, Ch.S., Pierson, C.T., Santos, E.S. (1984): Chemical characteristics of roll-type uranium deposits in Wyoming and Texas. U.S. Geological Survey Open File Report, 84-366, pages 1-18.

Stanton, M.R. and Goldhaber, M.B. (1991): Experimental studies of the synthesis of pyrite and marcasite (FeS_2) from 0º to 200º C and summary of results. USGS Open-File Report 91-310, 26 pages.

Stern, T.W. and Stieff, L.R. (1956): Radium-uranium equilibrium and radium-uranium ages of some Colorado Plateau secondary minerals. USGS Trace Elements Investigations Report 482, 21 pages.

Stieff, L.R., Stern, T.W. and Milkey, R.G. (1953): A preliminary determination of the age of some uranium ores of the Colorado plateaus by the lead-uranium method. USGS Survey Circular 271, 26 pages.

Terry, D.O. (1998): Lithostratigraphic revision and correlation of the lower part of the White River Group: South Dakota to Nebraska. Geological Society of America Special Paper 325, pages 15-37.

Thamm, J.K., Kovschak, A.A., Adams, S.S. (1981): Geology and recognition criteria for sandstone uranium deposits of the Salt Wash Type, Colorado Plateau Province. U.S. Dept. Energy Final Report, GJBX-6 (81), 111 pages.

Trimble, D. E. (1980): Cenozoic tectonic history of the great plains contrasted with that of the southern rocky mountains; a synthesis. The Mountain Geologist, **17** (3), pages 59-69.

Tweto, O. (1980): Precambrian geology of Colorado. Colorado Geology: Rocky Mountain Association of Geologists, pages 37-46.

Tyler, N. and Ethridge, F. (1983): Depositional setting of the Salt Wash Member of the Morrison Formation, Southwest Colorado. Journal of Sedimentary Petrology, **53**, no. 1, pages 67-82.

Wanty, R.B., Goldhaber, M.B., Northrop, H.R. (1990): Geochemistry of vanadium in an epigenetic, sandstone-hosted vanadium-uranium deposit, Henry Basin, Utah. Economic Geology, **85**, pages 270-284.

Warren, C.G. (1972): Sulfur isotopes as a clue to the genetic geochemistry of a roll-type uranium deposit. Economic Geology, **67**, pages 759-767.

Warren, C.G. and Granger, H.C (1969): Unstable sulfur compounds and the origin of roll-type uranium deposits. Economic Geology, **64**, pages 160-171.

Warren, C.G., Granger, H.C., Schock, J.H. (1980): Shape of roll-type uranium deposits. U.S. Geological Survey Open File Report. 80-100, pages 1-31.

Wright, R.J. (1955): Ore controls in sandstone uranium deposits of the Colorado Plateau. Economic Geology, **50**, pages 135-155.

Zerkle, A.L., Farquhar, J., Johnston, D.T., Cox, R.P., Canfield, D.E. (2009): Fractionation of multiple sulfur isotopes during phototrophic oxidation of sulfide and elemental sulfur by a green sulfur bacterium. Geochimica et Cosmochimica Acta, **73**, pages 291-306.

Zielinski, R.A. (1980): Uranium in secondary silica: a possible exploration guide. Economic Geology, **75**, pages 592-602.

Appendix A: Hand Sample Descriptions

Table 1: Hand sample descriptions, Colorado deposits

JD-6 1-1	Mottled grey/black, medium grained sandstone with minor clay lenses. Exposed surface shows approximately millimetre thick orange, crystalline crust (extensive oxidation; secondary mineralization). Moderately indurated, brittle.	
JD-6 1-2	Mottled dark grey clay-rich, fine grained sandstone (oxidized); massive, brittle. Exposed surface shows < 1mm yellow/orange crystalline crust. Very fine grained yellow and green alteration on fracture surfaces, spatially associated with clay. Clay has blocky fracture pattern, with conchoidal surfaces.	
JD-6 1-3	Pale green, fine to medium-grained sandstone (oxidized), massive. Discontinuous and diffuse dark grey clay laminae, 1-5 mm thick, somewhat mottled texture. Patchy yellow and white clayey alteration as specks and blebs (<2%).	

JD-6 1-4	Dark grey, fine to medium-grained sandstone, massive. Predominantly quartz with minor lithic grains in >15% clay matrix. Very diffuse (<10%) yellow alteration specks and blebs (composed of clay size particles). Minor, sporadic white, irregular 1-5 mm clay blebs. Minor dark grey clay galls (1-5 mm).	
SM-18 1-1	Light brown, fine to medium grained, massive sandstone with fine grained, brown specks (iron oxide). Well cemented, well consolidated. Common green clay clasts, <1 mm, slightly elongated parallel to bedding.	
SM-18 1-2	Medium grained, light brown, massive sandstone, well cemented and consolidated. Dark reddish-brown staining form 1-5 mm thick laminae. Minor dark grey clay galls, 1-3 mm. Fine grained, brown (iron oxide) specks, ~ 1 mm.	

SM-18 1-3	Top (oxidized): fine to medium grained sandstone, dark grey/green. Centimetre sized, irregular clay lenses. Greenish staining throughout with minor yellow, clayey alteration specks. Sharply diffuse contact between underlying light brown, reduced fine grained sandstone. Orange, millimetre thick iron oxide stained laminae.	
SM-18 1-4	Top (oxidized): 0.5-1.5 cm thick, shaley, dark grey, fine grained sandstone. Possible medium sized coal fragments (black, conchoidal fracture). Sharply diffuse transition to light grey, bleached, fine to medium-grained sandstone. Pale orange (iron oxide) stained laminae crosscut by upper layers, 1-3 cm thick.	
SM-18 1-5	Pale brown, medium-grained sandstone with minor (<10%), lithic grains (1-2 mm). Porous, well indurated, massive. Spotty brown (limonite) staining, as blebs <1 mm.	

JD8 1-1	Laminated (oxidized) sandstone: medium grained, light grey with discontinuous mudstone laminae and abundant mud clasts, 1-2 cm. Pale red staining, patchy, also minor limonite alteration. White siliceous alteration and yellow clay alteration on fracture planes and exposed surfaces.	
JD8 1-2	Shale, massive, dark grey. Yellow clay alteration on fracture and bedding planes.	

Table 2: Hand sample descriptions, Three Crow, Nebraska

08 T810C 001	Grey/brown fine-grained sand with minor silty clay mottling. Unconsolidated.	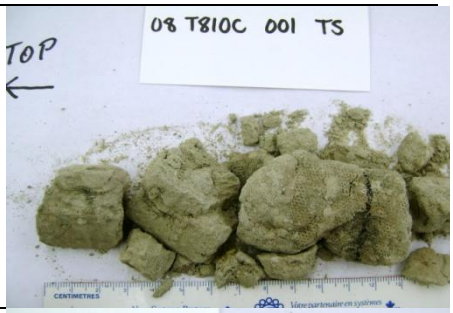
08 T810C 002	Green/dark grey, fine-grained sand. Minor local, centimetre-sized orange/yellow silty lenses. Unconsolidated.	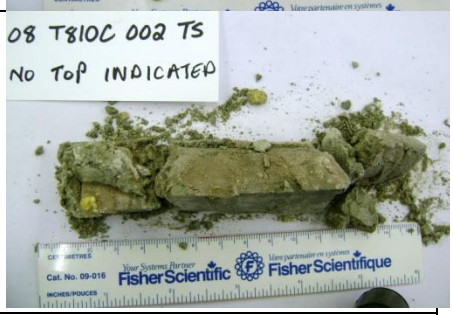
08 T810C 003	Light brown, fine grained, massive sand. Unconsolidated.	
8 T810C 004	Medium grey/brown, fine to medium-grained sand. Unconsolidated.	
08 T810C 005	Light grey and brown mottled, fine-grained sand. Weakly indurated.	

08 T797 001	Medium grey, fine-grained sand. Local minor red staining. Weakly indurated.	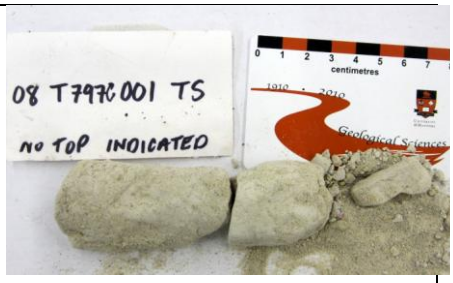
08 T797 002	Light brown/yellow fine to very fine-grained, clay-rich sand with red/brown stained mottling. <2% fine to medium-grained black lithics, and are locally stained bright red. Unconsolidated.	
08 T797 003	Medium brown, fine to medium-grained, clay-rich sand. Minor orange to brown, silty clay mottling. Unconsolidated.	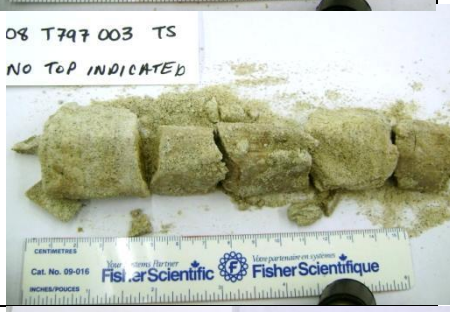
08 T797 004	Predominantly yellow/white, very fine to very coarse- grained conglomerate. Very poorly sorted with common coarse grained, rounded, light grey quartz and minor medium to coarse lithic grains. Common medium to coarse grained, angular black lithic grains. Porous, poorly indurated.	
08 T797 005	Mottled yellow and light brown, medium-grained, conglomerate with common grey clay mottling. Common black to grey, angular, medium to very coarse lithic grains. Poorly indurated, porous.	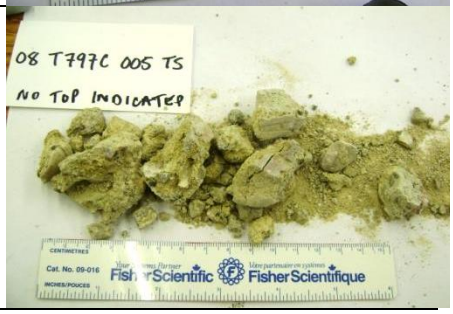

08 T797C 006	Dark grey, silty clay. Common orange, discontinuous clay laminae and centimetre-sized clay lenses. Moderately indurated.	
T792C-08-01	Mottled light grey, fine grained sand with common pink clay lenses and pink-stained laminae. Unconsolidated.	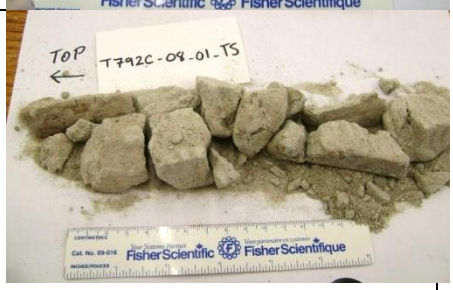
T792C-08-02	Light grey, fine grained sand. Local brown iron-oxide stained, discontinuous laminae. Unconsolidated.	
T792C-08-03	Top: light grey/brown, fine-grained sand grading to dark grey/ brown silty clay grading into fine grained sand. Minor yellow/brown mottling. Unconsolidated.	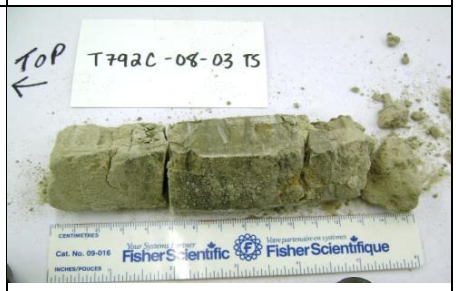
T792C-08-04	Grey/brown fine to medium grained sand with silty clay interbeds. Abundant massive, centimetre-sized lenses and laminae composed of silty black grains. Local red/brown iron-oxide coatings on bedding planes. Weakly indurated, crumbly, porous.	

T792-08-05	Mottled mint green clay and dark grey clay with light grey, fine to coarse-grained, poorly sorted sand. Minor coarse, rounded dark grey/black pebbles. Unconsolidated.	
T792-08-06	Predominantly light brown/grey, fine to medium-grained sand with green clay mottling towards bottom of interval. Trace thin, black laminae and irregular, centimetre-sized black, silty lenses. Minor coarse to very coarse grey quartz and dark pebbles. Unconsolidated.	
T792-08-07	Medium grey, silty clay mottled with minor fine grained, light grey sand and local thin, black laminae. Medium-grained white feldspars and medium to coarse lithic grains impart a “salt and pepper” texture. Unconsolidated.	
T792-08-08	Medium to light brown, clay-rich, silty to fine-grained sand with red stained laminae and grey clay galls. Medium to coarse-grained white feldspars and black lithic grains impart a “salt and pepper” texture. Unconsolidated.	
T792-08-09	Fine to medium grained, brown clay-rich sand mottled with minor dark grey clay. Common black, centimetre-thick laminae. Local red/orange staining near top of interval. Weakly indurated.	

T792-08-10	Fine grained, light brown sand, moderately sorted, poorly consolidated (first 10 centimetres). Becoming increasingly argillic towards bottom of interval (no top indicated) with white and grey clay galls, grading into white, yellow, and grey clay laminae interbedded with minor fine-grained sand. Unconsolidated.	
H161C-01	Predominantly fine to medium-grained sand with common pebbles and cobbles. Crumbly.	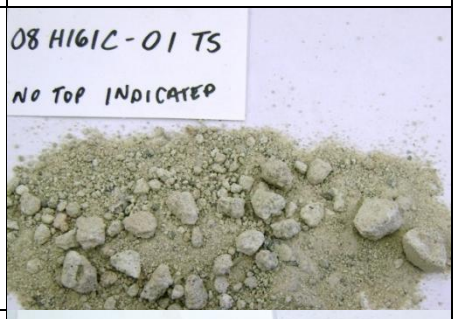
H161C-02	Predominantly fine to medium grained conglomerate. Minor medium to very coarse quartz pebbles and medium-grained lithics. Poorly indurated. Crumbly and porous fragments.	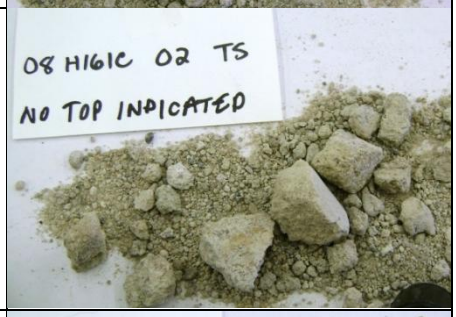
H161C-03	Predominantly fine to medium grained conglomerate. Minor medium to very coarse quartz pebbles and medium-grained lithics. Poorly indurated. Crumbly and porous fragments.	
H161C-04	Predominantly fine to medium-grained, light brown and grey, weakly cemented sandstone mottled with red and grey clay galls. Common pebbles and cobbles. Poorly indurated. Porous fragments.	

H161C-05	Fine to medium-grained grey and pink sand fragments mottled with minor grey clay. Crumbly and porous.	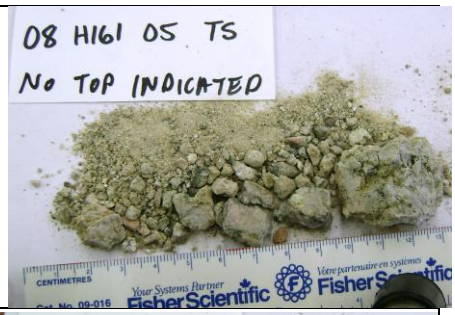
H161C-06	Brown, clay-rich fine to medium-grained sand with green, yellow and red clay mottling. <5% medium-grained white feldspars and black lithics. Unconsolidated.	
H161C-07	Brownish grey, fine to medium-grained sand with minor clay mottling. Unconsolidated.	
H161C-08	Dark grey/brown, fine to medium grained sand with common coarse to very coarse rounded pebbles and cobbles. Porous, weakly consolidated.	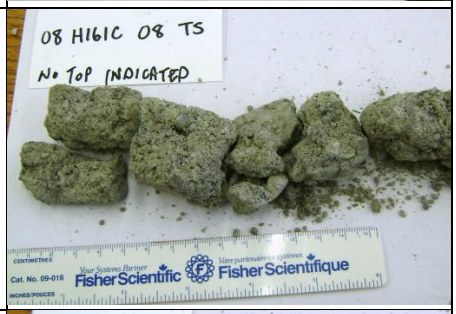
H161C-09	Medium grey/brown, medium to coarse grained sand. Local yellow clay mottling with minor coarse to very coarse, rounded, pebbles and cobbles. Unconsolidated.	

H161C-10	Light grey/brown, silty to fine-grained sand, weakly cemented. Porous. Weakly consolidated.	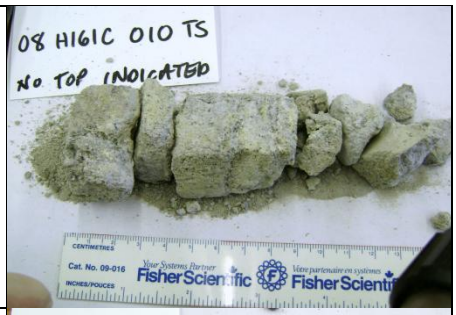
H161C-11	Dark grey, silty clay.	
H150C-02	Medium brown, clay-rich fine-grained sands. Some local red/brown staining. Unconsolidated.	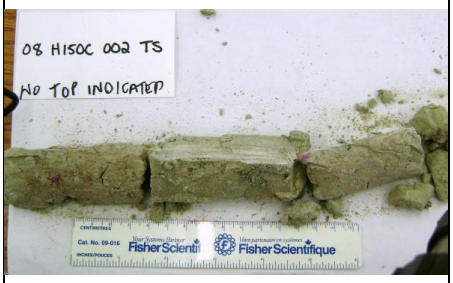
H150C-03	Light brown, fine to very fine-grained sand. Unconsolidated.	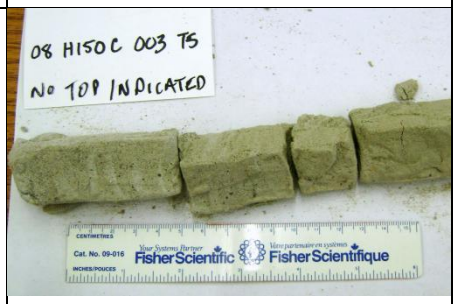
H150C-04	Light brown, very fine to fine-grained sand. Local iron stained mottling. Unconsolidated.	

H150C-05	Light brown, very fine to fine-grained sand. Local iron-stained mottling. Unconsolidated.	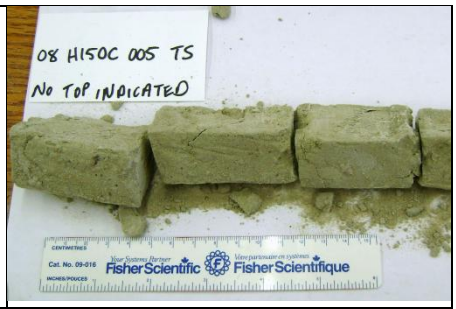
H150C-06	Light brown, very fine to fine-grained sand. Unconsolidated.	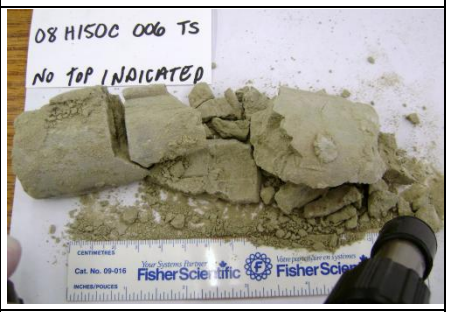
H150C-07	Light grey and brown, very fine to fine grained sand mottled with dark greyish brown, silty clay. Local orange/pink/white-staining. Unconsolidated.	
H150C-08	Light brown, very fine-grained sand. Local orange/pink/white and brown-clay mottling. Unconsolidated.	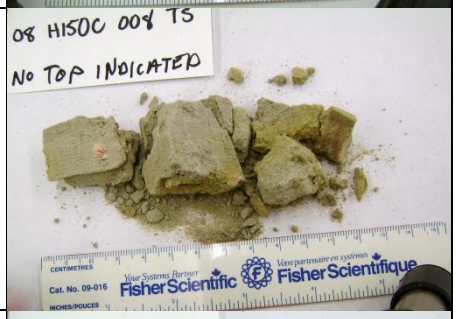
H150C-09	Brown/yellow fine-grained sand with <1 cm thick outer surface stained red/brown (drilling muds?). Unconsolidated.	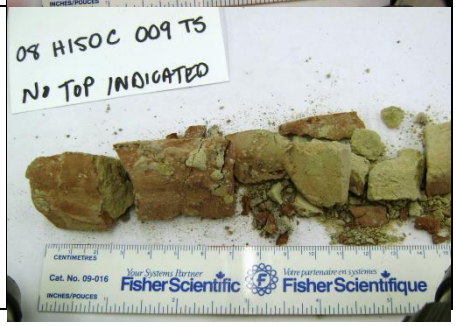

H150C-10	Yellow/brown, fine-grained sand. Local red-stained mottling. Unconsolidated.	
H150C-11	Yellowish brown, fine-grained silty sand. Unconsolidated.	
H150C-12	Yellowish brown, fine-grained silty sand. Local red-stained mottling. Unconsolidated.	
H150C-13	Yellowish brown, fine-grained silty sand. Unconsolidated.	
H150C-14	Yellowish brown, silty to fine-grained sand. Poorly consolidated.	

Appendix B: Thin Section Descriptions

Table 1: Sample thin descriptions, Colorado deposits

Sample	**Quartz**	**Lithics**	**Feldspar**	**Matrix**	**Cement**	**Organics/ opaques**	**Sulphides**	**Comments**
SM18-1-1	50-60% fine to medium-grained quartz, subangular and embayed.	<2% lithic clasts composed of clay minerals and silty quartz inclusions.	<1% fine-grained, sub-rounded feldspars.	5-10% dark brown, clay-rich matrix.	Well-cemented with quartz overgrowths and minor calcite.	Strong iron-oxide staining of matrix.	N/A	Moderately sorted, matrix-supported sandstone. Well-cemented by quartz overgrowths and calcite cement.
SM18-1-2	50-60% fine to medium-grained quartz, subangular to subrounded, embayed.	<2% lithic clasts composed of clay minerals and silty quartz inclusions with trace mica.	<1% fine-grained, sub-rounded feldspars.	5-10% dark brown, clay-rich matrix.	Well-cemented with quartz overgrowths and minor calcite.	<2% fine to medium-grained, laminated opaque minerals, subangular. Strong iron-oxide staining of matrix.	N/A	Moderately sorted, matrix-supported sandstone. Well-cemented by quartz overgrowths and calcite cement.

Sample	Quartz	Lithics	Feldspar	Matrix	Cement	Organics/ opaques	Sulphides	Comments
SM18-1-3	50-60% fine to medium-grained quartz, subangular, embayed. Locally micro-quartz rimming grains.	<2%fine to medium-grained lithic clasts composed of clay. Local mica laminae.	<1% fine-grained, sub-rounded feldspars.	5-10% dark brown, clay-rich matrix.	Well-cemented with quartz overgrowths and minor calcite. Clay minerals rimming detrital minerals.	<2% fine to medium-grained, laminated opaque minerals, subangular. Strong iron-oxide staining of matrix minerals. <1% cellular OM, coarse.	N/A	Moderately sorted, matrix-supported sandstone. Well-cemented by quartz overgrowths, clay minerals and minor calcite cement.

Sample	Quartz	Lithics	Feldspar	Matrix	Cement	Organics/ opaques	Sulphides	Comments
JD-6-1	60-70% fine to medium-grained quartz.	<5% lithic clasts composed of clay minerals with minor quartz and feldspar.	<1% fine-grained feldspar, sub-rounded.	<5% dark brown, clay minerals with minor silty quartz. <1% silty to fine-grained, black montroseite needles rimming detrital minerals.	Well-cemented with quartz overgrowths and poikilitic calcite.	Minor silt to fine-grained, angular opaques.	N/A	Moderately sorted, matrix supported sandstone. Well-cemented by quartz overgrowths and calcite cement.
JD-6-2	10-15% fine to medium-grained quartz, subrounded to subangular. Trace silt to fine-grained polycrystalline quartz.	<1% lithic clasts composed of clay minerals.	<1% fine-grained feldspar, sub-rounded	40-50% clay-rich laminae with fan-shaped aggregates of montroseite.	N/A	Minor silt to fine-grained, angular opaques Cellular OM.	<1% fine to medium-grained pyrite, locally associated with ore minerals	Clay and sand laminations.
JD-6-3	50-60% fine to medium-grained quartz.	<5% lithic clasts composed of clay minerals with minor quartz and feldspar.	<5% lithic clasts composed of clay minerals with minor quartz and feldspar.	<5% dark brown, clay minerals with minor silty quartz. <3% silty to fine-grained, black montroseite needles rimming detrital minerals.	Well-cemented with quartz overgrowths and poikilitic calcite.	N/A	N/A	Moderately sorted, matrix supported sandstone. Well-cemented by quartz overgrowths and calcite cement.

Sample	Quartz	Lithics	Feldspar	Matrix	Cement	Organics/ opaques	Sulphides	Comments
JD-6-4	50-60% fine to medium-grained quartz. <5% fine to medium-grained polycrystalline quartz. Sub-rounded and locally embayed boundaries.	<5% lithic clasts composed of clay minerals with minor quartz and feldspar.	<5% lithic clasts composed of clay minerals with minor quartz and feldspar.	<5% dark brown, clay minerals with minor silty quartz. <3% silty to fine-grained, black montroseite needles rimming detrital minerals.	Well-cemented with minor poikilitic and silty to fine-grained calcite. Locally clay minerals rimming detrital minerals and minor quartz overgrowths.	N/A	N/A	Moderately to poorly sorted, matrix supported sandstone. Well-cemented by quartz overgrowths and calcite cement.

Sample	Quartz	Lithics	Feldspar	Matrix	Cement	Organics/ opaques	Sulphides	Comments
JD8-1	60-70% fine to medium-grained quartz. Local sutured boundaries. Trace fine to medium-grained polycrystalline quartz, sub-rounded.	<2% elongated lithic clasts composed of clay minerals and silty quartz inclusions.	<1% fine-grained, sub-rounded feldspars.	10-15% dark brown clay-rich matrix, laminated. <2% silt to fine-grained montroseite needles interstitial to framework grains.	Well-cemented locally by quartz overgrowths and minor calcite.	N/A	N/A	Well-sorted, matrix and locally grain-supported sandstone.
JD8-2	40-50% fine to medium-grained quartz, subangular.	5-10% lithic clasts composed of clay minerals and silty quartz inclusions	<1% fine-grained, sub-rounded feldspars	5-10% dark brown clay-rich matrix. Trace silt to fine-grained montroseite needles interstitial to framework grains	Local calcite and quartz overgrowths.	Abundant cellular OM, locally compacted and interlaminated with clay.	N/A	Moderately sorted, matrix-supported sandstone.
JD8-3	60-70% medium to coarse-grained quartz, subrounded to subangular. Trace fine-grained chert, irregular boundaries.	<2% lithic clasts composed of clay minerals and silty quartz inclusions.	<1% fine-grained, sub-rounded feldspars.	<5% dark brown clay-rich matrix. Trace silt to fine-grained montroseite needles interstitial to framework grains.	Well-cemented locally by quartz overgrowths and minor calcite.	N/A	N/A	Well-sorted, grain-supported sandstone.

Table 1: Sample thin descriptions, Three Crow, Nebraska

Sample	Quartz	Accessory minerals	Lithics	Feldspar	Matrix	Organics/ opaques	Sulphides	Comments
T810C-02	Predominantly (40-50%) silt to fine-grained quartz within clay-rich, moderately foliated laminae. 5-10% coarse silt to medium-grained subangular quartz in clay-rich matrix comprising mm-thick laminae.	<5% silt to fine-grained muscovite, moderately foliated.	<1% fine to medium-grained clasts, slightly elongated and composed of clay to very fine-grained silicates.	<5% subangular plagioclase and kspar within coarser laminae.	15-20% matrix minerals and comprise <5% of matrix in coarser laminae. Predominantly clay to silt sized silicate minerals.	<5% silt-sized opaque specks.	<2% pyrite, very fine to medium-grained, skeletal. Trace silt to fine-grained subhedral pyrite.	Clay-rich laminations with minor silt to fine-grained silicates. Local mm-thick laminae comprised of fine to medium-grained, matrix-supported sand.
T810C-03	50-60% coarse silt to fine-grained framework quartz. Subangular to subrounded with embayed boundaries and pitted surfaces.	N/A	<1% fine to medium-grained clasts composed of clay to very fine-grained silicates.	<5% silt to medium-grained plagioclase and kspar, subangular with common embayed crystal boundaries.	15-20% clay-rich matrix. <2% fine to medium-crystalline calcite.	<2% silt-sized opaque specks.	N/A	Moderately to poorly-sorted matrix-supported sand.

Sample	Quartz	Accessory minerals	Lithics	Feldspar	Matrix	Organics/ opaques	Sulphides	Comments
T810C-04	50-60% silty to medium-grained framework quartz. Subangular to subrounded with very fine grained mica inclusions. <1% fine to medium-grained polycrystalline quartz with rounded irregular boundaries.	Trace silt to fine-grained muscovite.	<5% silt to medium-grained composed of clay to fine-grained silicates.	<2% silt to medium-grained plagioclase and kspar subrounded to subangular.	15-20% matrix minerals comprised predominantly of clay with minor silt and trace very fine-grained silicates. Trace local aggregates of very fine to fine-grained calcite.	<5% opaque specks within matrix.	<1% coarse-grained subangular pyrite intergrown with marcasite in diffuse clusters.	Poorly-sorted, matrix-supported sand.
T810C-05	Predominantly 50-60% fine to medium-grained framework quartz. Subangular. <10% silty to fine-grained quartz. Subangular to subrounded.	Trace silt to fine-grained muscovite.	<1% fine to medium-grained clasts composed of clay to very fine-grained silicates.	<5% silt to medium-grained plagioclase and kspar, subangular with common embayed crystal boundaries.	5-10% matrix minerals comprised predominantly of clay minerals.	<2% opaque specks with trace fine to medium-grained angular opaques within matrix.	N/A.	Poorly-sorted, matrix-supported sand.

Sample	Quartz	Accessory minerals	Lithics	Feldspar	Matrix	Organics/ opaques	Sulphides	Comments
T792C-01	50-60% fine to medium-grained framework quartz, subangular to subrounded. Boundaries commonly embayed.	Trace fine-grained muscovite.	<10% silty to fine-grained clasts composed of clay minerals.	<1% fine-grained, subangular plagioclase and kspar. Boundaries commonly embayed and rimmed with clay minerals.	10-15% clay-rich matrix with minor silt-sized quartz, feldspar, chert and opaques.	Trace opaque specks	Trace fine-grained subangular pyrite.	Poorly-sorted, matrix-supported sand.
T792C-02	50-60% fine to medium-grained, framework quartz, subangular to subrounded. Boundaries commonly embayed. Minor polycrystalline quartz.	Trace fine-grained muscovite.	<10% silty to fine-grained clasts composed of clay minerals.	<1% fine-grained, subangular plagioclase and kspar. Boundaries commonly embayed and rimmed with clay minerals.	10-15% clay-rich matrix with minor silt to fine-grained quartz, feldspar, chert and opaques.	Trace opaque specks	N/A	Poorly-sorted, matrix-supported sand.

Sample	Quartz	Accessory minerals	Lithics	Feldspar	Matrix	Organics/ opaques	Sulphides	Comments
T792C-03	10-15% fine to medium-grained quartz within massive clay. Subangular to subrounded. Local centimetre-wide laminations composed mainly of fine to medium-grained, subangular to subrounded quartz show weak mineral alignment.	N/A	<1% medium-grained clasts composed of clay minerals.	<2% silty to medium-grained subangular feldspar. <5% fine to medium-grained laths within coarser laminae show weak mineral alignment.	50-60% brown, clay-rich matrix with minor silty to fine-grained quartz and feldspar.	<2% silt to fine-grained opaques.	Trace fine-grained subangular pyrite.	Predominantly dark brown clay with fine to medium-grained laminae showing weak mineral alignment. Shrinkage cracks common in clay.
T792C-04	15-20% fine to medium-grained quartz, subrounded to subangular. <1% fine to coarse-grained polycrystalline quartz.	<1% lithic clasts composed of clay minerals.	Trace fine-grained muscovite.	<2% silty to medium-grained subangular feldspar	50-60% brown, clay-rich matrix with minor silty to fine-grained quartz and feldspar	<2% silt to fine-grained opaques.	<1% dense clusters of silt to fine-grained pyrite, subangular.to subrounded.	Predominantly dark brown clay with fine to medium-grained laminae

Sample	Quartz	Accessory minerals	Lithics	Feldspar	Matrix	Organics/ opaques	Sulphides	Comments
T792C-05	40-50% fine to medium-grained, subangular framework quartz. <10% coarse-grained poikilitic quartz, commonly embayed. Trace fine to medium-grained polycrystalline quartz.	N/A	Trace fine to medium-grained clasts composed of clay minerals. Trace fine-grained sandstone fragments, subrounded.	<5% very fine to fine-grained plagioclase and kspar, subangular.	10-15% brown, clay-rich matrix with minor silty to fine-grained quartz.	Trace opaque specks in matrix	N/A	Very poorly sorted matrix-supported sand.
T792C-06	40-50% fine to medium-grained, framework quartz, subangular to subrounded. Commonly poikilitic with mica inclusions and embayed boundaries. <5% medium to coarse-grained quartz, subrounded.	Trace very fine to fine grained muscovite as inclusions in framework quartz.	<2% very fine to fine-grained clasts composed of clay minerals, sub-angular and embayed.	5-10% fine to medium-grained plagioclase and feldspar, subangular to subrounded.	15-20% clay-rich matrix with minor silt to fine-grained quartz. Trace opaque specks.	Trace opaque specks in matrix.	N/A	Very poorly sorted matrix-supported sand.

Sample	Quartz	Accessory minerals	Lithics	Feldspar	Matrix	Organics/ opaques	Sulphides	Comments
T792C-07	40-50% fine to medium-grained quartz. Subrounded and commonly embayed. Minor fine to medium-grained polycrystalline quartz, irregular boundaries. <1% coarse-grained chalcedonic quartz, irregular boundaries.	Trace fine-grained muscovite.	<2% fine to medium-grained sandstone clasts composed of silt to fine-grained quartz and opaque specks.	5-10% silt to medium-grained plagioclase and kspar. Subangular and coarser grains are commonly embayed where clay minerals are rimming/replacing crystal boundaries.	15-20% brown, clay-rich and poorly sorted, with minor silt to fine-grained quartz, chert and feldspar.	Brown iron staining of matrix minerals.	<3% framboidal pyrite framboids <1 µm). Trace fine-grained subangular pyrite. Locally framboid aggregates are cemented by subangular pyrite.	Poorly sorted, matrix-supported sand.
T792C-08	40-50% silt to fine-grained framework quartz. <2% medium-grained quartz, subrounded to subangular, embayed boundaries and pitted surfaces of coarser grains. Minor medium-grained polycrystalline quartz with subrounded and irregular boundaries.	Trace fine-grained muscovite.	<5% very fine to medium-grained clasts composed of clay minerals, sub-angular. Trace fine to medium-grained sandstone clasts.	<5% fine to medium-grained plagioclase and kspar. Common embayed boundaries of coarser grains. Trace coarse feldspar pseudomorphs where clay and minor silt to fine-grained silicate minerals replace laths.	5-10% clay-rich matrix.	Strong brown iron staining of matrix minerals and locally framework grains imparting a mottled texture.	N/A	Fragments from fractured brown clay-rich laminae intermingled with very poorly sorted matrix-supported sand.

Sample	Quartz	Accessory minerals	Lithics	Feldspar	Matrix	Organics/ opaques	Sulphides	Comments
T792C-09	30-40% coarse silt to medium-grained framework quartz. Subangular to subrounded. <2% medium-grained radial-fibrous quartz. <1% fine to medium-grained polycrystalline quartz with irregular boundaries.	<5% very fine to fine-grained muscovite.	<2% fine to medium-grained sandstone clasts, irregular boundaries.	5-10% fine to medium-grained plagioclase and kspar. Coarser grains are commonly embayed.	15-20% dark brown, clay-rich matrix with silt to fine-grained quartz, feldspar and lithic clasts.	<1% opaques, subangular to specks.	N/A	Poorly sorted, matrix-supported sand.

Sample	Quartz	Accessory minerals	Lithics	Feldspar	Matrix	Organics/ opaques	Sulphides	Comments
H161C-01	40-50% medium to coarse-grained quartz. <1% very coarse-grained rounded and polycrystalline quartz.	N/A	Trace silt to medium-grained chert, irregular, embayed boundaries.	<5% silt to medium-grained feldspar. Locally pitted.	20-30% dark brown, clay-rich matrix and minor fine grained, subangular to angular silicates.	Trace silty black specks.	N/A	Very poorly sorted, clay-rich sand.
H161C-02	40-50% fine grained quartz, subangular to subrounded. <2% medium to very coarse-grained, sub-rounded quartz and polycrystalline quartz with embayed boundaries. Trace medium to coarse-grained aggregates of radial fibrous quartz.	Trace fine-grained muscovite.	<3% fine-grained lithic clasts composed of 1) sandstone fragments and 2) of clay minerals with minor muscovite and opaque specks.	<5% coarse silt to fine-grained feldspar. Subangular laths.	15-20% clay-rich matrix and minor fine grained, subangular to angular silicates.	Minor opaque specks within lithic sandstone fragments.	N/A	Poorly sorted, matrix-supported sand.

Sample	Quartz	Accessory minerals	Lithics	Feldspar	Matrix	Organics/ opaques	Sulphides	Comments
H161C-03	50-60% medium to coarse-grained quartz. <1% very coarse-grained polycrystalline quartz, subrounded .	N/A	Trace silt to medium-grained chert, irregular, embayed boundaries.	<5% coarse silt to fine-grained feldspar. Subangular laths.	15-20% clay-rich matrix and minor silty to fine grained, subangular to angular silicates.	Minor opaque specks within lithic sandstone fragments and trace silty black specks in matrix.	<1% fine to medium-grained fractured pyrite clusters.	Poorly sorted, matrix-supported sand.
H161C-04	10-20% fine to medium-grained quartz, subangular with embayed boundaries. Trace medium-grained polycrystalline quartz. Locally medium to coarse-grained quartz are pitted and coated with fine-grained iron oxides. Coffinite occurs within elongated, sub-parallel (dissolution) pits	N/A	<2% medium to coarse-grained rock fragments, subangular and composed of silt to fine-grained sandstone.	<2% coarse silt to fine-grained feldspar.	<10% clay-rich matrix with minor coarse silt to very fine grained, subangular to angular silicates.	Trace silty black specks.	<2% massive fracture-filling (quartz) pyrite. Trace very fine-grained framboidal pyrite. Trace silt-sized pyrite inclusions in quartz (SEM).	Trace coffinite mineralization (SEM, EMP). Poorly sorted, matrix-supported sand.

Sample	Quartz	Accessory minerals	Lithics	Feldspar	Matrix	Organics/ opaques	Sulphides	Comments
H161C-06	30-40% very fine to fine-grained quartz, subangular.	N/A	<2% silt to fine-grained rock fragments, subangular and composed of silt to fine-grained sandstone. Trace fine-grained chert, subrounded.	<2% coarse silt to fine-grained feldspar.	10-15% clay-rich matrix with minor silt subangular to angular silicates.	Trace silty black specks.	N/A	Moderately sorted, matrix-supported sand.
H161C-07	30-40% very fine to fine-grained quartz, subangular.	N/A	<2% silt to fine-grained rock fragments, subangular and composed of silt to fine-grained sandstone. Trace fine-grained chert, subrounded.	<2% coarse silt to fine-grained feldspar.	10-15% clay-rich matrix with minor silt-sized silicates.	Trace silty black specks.	N/A	Moderately sorted, matrix-supported sand.
H161C-08	30-40% very fine to fine-grained quartz, subangular. Trace coarse, pitted, subrounded quartz.	N/A	<2% silt to fine-grained rock fragments, subangular. Trace fine-grained chert, subrounded.	<2% coarse silt to fine-grained feldspar.	10-15% clay-rich matrix with minor silt subangular to angular silicates.	Trace silty black specks.	N/A	Moderately sorted, matrix-supported sand.

Sample	Quartz	Accessory minerals	Lithics	Feldspar	Matrix	Organics/ opaques	Sulphides	Comments
H161C-11	60-70% very fine to fine-grained quartz, subangular.	N/A	Trace lithic clasts composed of clay minerals, subangular.	<2% coarse silt to fine-grained feldspar.	15-20% medium brown, clay-rich matrix with minor silt-sized silicate phenocrysts.	N/A	N/A	Well sorted, matrix-supported sand.
H161C-12	60-70% very fine to fine-grained quartz, subangular.	N/A	Trace lithic clasts composed of clay minerals, subangular.	<2% coarse silt to fine-grained feldspar.	15-20% medium brown, clay-rich matrix with minor silt-sized silicate phenocrysts..	Local iron-stained lenses	N/A	Well sorted, matrix-supported sand.
H161C-13	60-70% very fine to fine-grained quartz, subangular.	N/A	Trace lithic clasts composed of clay minerals, subangular.	<2% coarse silt to fine-grained feldspar.	15-20% medium brown, clay-rich matrix with minor silt-sized silicate phenocrysts.	N/A	N/A	Well sorted, matrix-supported sand.
H161C-14	60-70% very fine to fine-grained quartz, subangular.	N/A	Trace lithic clasts composed of clay minerals, subangular.	<2% coarse silt to fine-grained feldspar.	15-20% medium brown, clay-rich matrix with minor silt-sized silicate phenocrysts.	N/A	N/A	Well sorted, matrix-supported sand.

Sample	Quartz	Accessory minerals	Lithics	Feldspar	Matrix	Organics/ opaques	Sulphides	Comments
H150C-002	50-60% fine to medium-grained quartz, sub-rounded to sub-angular. Trace medium-grained polycrystalline quartz, subrounded.	Trace fine-grained muscovite.	<5% fine to medium-grained clasts composed of clay-sized particles and trace fine to medium-grained quartz and feldspar. Trace fine-grained chert.	<5% fine to medium grained plagioclase and kspar, sub-angular to sub-rounded	5-10% clay-rich matrix with minor silt-sized quartz and chert. Trace poikilitic calcite cement.	<5% fine-grained black specks, diffuse	Trace pyrite as: 1) amorphous cement; 2) Sub-angular, medium-grained, poikilitic pyrite with quartz and calcite inclusions; 3) poikilitic, coarse-grained skeletal pyrite with calcite/dolomite (?) inclusions.	Poorly sorted, matrix-supported sand; small-scale graded bedding.
H150C-003	50-60% quartz, fine to medium-grained, sub-rounded to sub-angular.	Trace fine-grained muscovite.	10-15% fine-grained clasts composed of clay-sized components and minor silty quartz.	<5% fine to medium-grained plagioclase and kspar, subangular to subrounded.	10-15% clay-rich matrix.	<5% silt to medium-grained black specks and angular grains.	Trace pyrite: 1) fine to coarse-grained subangular and skeletal pyrite; 2) very fine-grained pyrite fragments	Poorly sorted, matrix-supported sand.
H150C-004	50-60% framework quartz, fine to medium-grained, sub-rounded to sub-angular.	Trace fine-grained muscovite.	10-15% fine-grained clasts composed of clay-sized components and trace very fine quartz.	<5% fine to medium-grained plagioclase and kspar, subangular to subrounded.	10-15% dark brown, clay-rich matrix.		Fine to medium-grained pyrite, sub-angular to skeletal with fine grained quartz inclusions	Poorly sorted, matrix-supported sand.

Sample	Quartz	Accessory minerals	Lithics	Feldspar	Matrix	Organics/ opaques	Sulphides	Comments
H150C-06	50-60% very fine to fine-grained quartz, subrounded to subangular, commonly showing embayed boundaries and pitted surfaces.	<2% very fine to fine-grained muscovite.	<2% coarse silt to fine-grained clasts composed of clay-sized components with trace very fine-grained quartz, muscovite and feldspar inclusions.	<5% coarse silt to very fine-grained plagioclase and kspar, sub-angular to sub-rounded.	10-20% brown, clay-rich matrix with minor silt-sized silicates. Trace finely-crystalline calcite rimming detrital grains.	Common very finely disseminated to fine-grained, sub-angular opaques.	1) fine to grained, subangular, fractured pyrite. 2) fine to coarse-grained aggregates of framboidal pyrite .	Very poorly sorted, matrix-supported sand
H150C-07	5-10% silt-sized quartz within very coarse, rounded clay fragments 30-40% silt to fine-grained quartz within matrix surrounding fragments.	N/A	<2% fine grained lithic grains composed of clay minerals and minor silty quartz grains .	5-10% fine-grained plagioclase and kspar, subangular.	Predominantly silty clay matrix.	Strong iron-oxide staining of matrix.	N/A	Heterogeneous textures. Predominantly coarse, rounded fragments of dark brown, silty clay laminae. Wavy laminations of dark brown silty clay interbedded with laminae composed of poorly sorted sand.

Sample	Quartz	Accessory minerals	Lithics	Feldspar	Matrix	Organics/ opaques	Sulphides	Comments
H150C-09	70-80% fine to medium - grained quartz, subangular to subrounded.	N/A	Trace fine-grained chert, subrounded.	<1% plagioclase and kspar, subangular.	10-15% brown/red clay-rich matrix with minor silt-sized silicates.	Trace silty to fine-grained black angular grains.	N/A	Heterogeneous textures. fragments of dark brown, silty clay interbedded with minor lenses of poorly sorted sand.
H150C-10	50-60% fine-grained quartz, subangular to subrounded. Trace fine-grained polycrystalline quartz, subrounded.	N/A	Trace fine-grained chert, subrounded. Trace lithic clasts composed of clay and minor silty silicates.	<1% fine-grained plagioclase and kspar, subangular.	10-15% clay-rich matrix with minor silt-sized silicates.	Trace black specks.	N/A	Very poorly sorted, matrix-supported sand
H150C-14	50-60% fine to medium-grained, subangular quartz. <5%coarse-grained quartz with embayed boundaries	Trace very fine-grained muscovite.	<3% very fine to fine-grained chert. <2% fine to medium-grained rock fragments composed mainly of clay minerals with phenocrysts.	5-10% fine-grained plagioclase and kspar, subangular. <1% medium to coarse-grained, sub-angular grains.	5-10% clay-rich matrix with silt sized quartz, feldspar, chert and lithic clasts.	Trace black specks	Trace silt to fine-grained, subangular pyrite.	Very poorly sorted, matrix-supported sand

Sample	Quartz	Accessory minerals	Lithics	Feldspar	Matrix	Organics/ opaques	Sulphides	Comments
T797C-01	50-60% fine-grained framework quartz. Subrounded to subangular with common embayed boundaries.	Trace fine-grained green chlorite (?).	<2% fine to medium-grained clasts composed of clay minerals. Subrounded, local embayed boundaries.	<3% silt to fine-grained plagioclase and kspar, subrounded. Trace medium-grained subangular feldspar. Common twinning.	<10% clay-rich matrix with minor silt-sized silicates..	<1% silt to fine-grained, subangular opaques. Dark brown iron-staining throughout.	N/A.	Moderately sorted, matrix-supported sand.
T797C-02	5-10% fine to medium-grained quartz. Subrounded.	N/A	N/A	<1% fine to medium-grained plagioclase and kspar, subrounded. Twinned.	Predominantly massive dark brown, clay-rich matrix comprising bulk of thin section.	N/A	N/A.	Massive dark brown clay with minor silt to medium-grained quartz and feldspar. Common fractures (shrinkage cracks?) throughout.
T797C-03	30-40% fine to medium-grained framework quartz. Subangular. Trace polycrystalline quartz.	Trace fine-grained biotite and muscovite.	<1% fine to medium-grained clasts composed of micro-quartz.	<5% silt to fine-grained kspar laths. Twinned. Trace fine-grained plagioclase laths.	10-15% yellow to dark brown clay-rich matrix.	<3% silt to fine-grained, subangular opaque grains. Iron-staining imparts laminated texture.	N/A.	Very poorly sorted, matrix-supported sand.

Sample	Quartz	Accessory minerals	Lithics	Feldspar	Matrix	Organics/ opaques	Sulphides	Comments
T797C-4	40-50% silt to fine-grained quartz, subangular to subrounded within matrix. <2% medium to coarse-grained framework quartz, subangular, fractured, embayed boundaries. <1% medium to coarse-grained polycrystalline quartz, irregular boundaries.	Trace silt to fine-grained muscovite.	<1% clasts composed of clay minerals with common embayed boundaries. <1% medium to coarse-grained clasts composed of microcrystalline quartz.	10-20% silt to medium-grained plagioclase and kspar. Locally coarser kspar has fine-grained muscovite inclusions.	15-20% matrix minerals composed predominantly of clay minerals with minor quartz and feldspar.	Poorly sorted, matrix-supported sand.	N/A.	Very poorly sorted, matrix-supported sand.
T797C-05B	80-90% medium to coarse-grained, circular to elliptical areas of radial-fibrous quartz (chalcedonic quartz), rimmed with microquartz.	N/A	N/A	N/A	5-10% micro-quartz.	Trace fine black specks. <10% brown, fine to medium-grained iron-stained and laths interstitial to chalcedonic quartz ellipses.	N/A.	Predominantly composed of chalcedonic quartz as replacement texture with pore-filling microquartz.

Sample	Quartz	Accessory minerals	Lithics	Feldspar	Matrix	Organics/ opaques	Sulphides	Comments
T797C-06	10-15% silt to fine-grained, locally poikilitic quartz. Subangular to slightly elongated.	<1% silt to fine-grained muscovite within matrix. <1% silt to fine-grained muscovite as inclusions within framework quartz.	<5% fine-grained clasts composed of clay minerals with irregular boundaries.	<5% silt to fine-grained kspar laths. Trace fine-grained plagioclase laths.	50-60% matrix composed predominantly of clay minerals with moderate foliated texture and minor alignment of phenocrysts.	Sharp contacts between brown iron-staining laminations throughout (without lithological change).	Local, fractured and folded pyrite laminae.	Dark-brown, clay-rich laminations with minor silt to fine-grained quartz and feldspars.

Appendix C: Electron Microprobe Analyses

Table 1: EMP results of principal elements forming uranium and vanadium minerals from JD-8 mine, Colorado

SiO_2	UO_2	CaO	V_2O_3	Al_2O_3	FeO	Na_2O	MgO	K_2O	Mineral
19.09	BDL	0.73	62.90	1.74	9.50	0.26	0.14	0.22	Mont
0.121	BDL	0.70	77.94	1.78	8.49	0.23	0.19	0.34	Mont
0.098	BDL	0.60	77.36	1.90	9.81	0.25	0.17	0.24	Mont
0.057	BDL	0.72	78.86	1.62	11.10	0.30	0.32	0.22	Mont
0.077	BDL	0.48	79.22	1.94	11.78	BDL	0.16	0.10	Mont
0.099	BDL	0.69	78.76	1.77	10.79	0.17	0.27	0.21	Mont
32.04	BDL	0.94	47.18	9.62	1.44	0.13	1.85	5.02	V-clay
47.24	BDL	0.36	22.20	15.76	1.73	0.09	5.16	4.52	V-clay
46.60	BDL	0.31	24.50	13.67	1.06	0.09	2.82	5.74	V-clay
43.75	BDL	0.30	29.02	13.05	0.86	0.08	2.62	5.98	V-clay
34.02	BDL	0.35	21.87	19.92	2.77	0.11	11.81	0.27	V-clay
43.50	BDL	0.35	24.12	14.90	1.84	0.07	4.79	5.36	V-clay
37.01	BDL	0.81	33.99	12.75	1.76	0.22	3.97	4.85	V-clay
38.86	BDL	0.44	27.76	12.89	1.94	0.14	3.80	5.46	V-clay
31.39	BDL	0.56	40.74	13.87	3.01	0.23	6.40	3.01	V-clay
14.99	40.96	2.40	24.31	3.83	0.60	0.18	1.29	2.76	U+V-clay
20.10	24.59	1.50	20.91	6.60	1.31	0.09	1.80	3.54	U+V-clay
BDL	63.10	1.03	25.23	0.11	0.06	0.10	0.09	0.97	U+V-clay
15.34	12.34	2.04	50.85	5.05	1.64	0.33	1.42	2.34	U+V-clay
37.98	8.58	0.78	27.15	10.36	0.78	0.12	2.52	6.33	U+V-clay

Mont: montroseite; Cof: coffinite; U+V-clay: uranium-rich vanadium clay; Car: carnotite

Table 2: EMP partial analysis in (weight %) of principal elements forming uranium and vanadium minerals from JD-6 mine, Colorado

SiO_2	UO_2	CaO	V_2O_3	P_2O_5	Al_2O_3	FeO	Mineral
0.18	BDL	0.60	72.83	0.03	0.46	17.34	Mont
0.37	BDL	1.57	75.03	0.05	0.60	11.66	Mont
0.18	BDL	0.58	74.12	0.02	0.47	15.81	Mont
0.20	2.19	1.35	75.23	0.05	0.53	10.85	Mont
0.33	BDL	2.18	77.68	BDL	0.50	6.65	Mont
0.12	BDL	0.99	71.08	0.03	0.55	15.35	Mont
0.24	BDL	1.45	73.86	0.12	0.82	8.97	Mont
0.28	4.74	1.44	70.88	0.13	0.72	11.44	Mont
2.45	1.20	1.08	73.24	0.06	1.98	8.02	Mont
0.12	1.17	1.02	72.04	0.04	0.53	15.76	Mont
0.24	1.50	1.64	72.32	0.11	0.58	11.64	Mont
15.08	66.09	3.28	2.23	2.72	0.32	0.11	Cof
14.02	66.47	3.57	3.74	2.56	0.58	0.21	Cof
13.72	65.66	3.28	3.43	2.53	0.41	0.18	Cof
14.46	70.78	3.03	3.80	2.72	0.46	0.21	Cof
14.41	67.00	3.10	4.62	2.19	0.4	0.21	Cof
10.23	78.53	2.25	0.93	1.62	0.25	0.16	Cof
8.98	68.40	2.87	2.93	1.89	0.20	0.06	Cof
10.32	76.94	1.75	0.71	1.54	0.25	0.08	Cof

Table 3: EMP partial analysis (in weight %) of principal elements forming uranium and vanadium minerals from JD-6 mine, Colorado

SiO_2	UO_2	CaO	V_2O_3	Al_2O_3	FeO	K_2O	Mineral
1.69	10.36	3.38	60.57	0.80	2.55	0.51	Cof/Mont
8.23	15.88	2.33	49.50	0.90	6.89	0.31	Cof/Mont
12.36	73.51	2.22	1.20	0.34	0.13	0.44	Cof
15.54	63.31	3.13	7.58	0.45	0.78	0.32	Cof
13.94	70.35	2.78	1.52	0.33	0.20	0.30	Cof
13.79	66.27	3.73	3.41	0.41	0.33	0.33	Cof

Table 4: EMP partial analysis (in weight %) of principal elements forming uranium and vanadium minerals from SM-18 mine, Colorado

SiO_2	UO_3	CaO	V_2O_5	Al_2O_3	FeO	Na_2O	MgO	K_2O	Mineral
10.46	40.03	2.77	18.46	1.72	6.89	0.92	0.47	5.73	U+ V-clay
11.57	34.71	3.03	19.55	4.50	7.81	1.01	0.83	6.48	U+ V-clay
27.15	20.70	2.77	18.58	4.98	8.87	0.96	1.61	4.02	U+ V-clay
15.47	26.63	2.29	21.36	6.12	9.25	0.87	1.84	5.26	U+ V-clay
21.12	29.70	0.29	17.89	12.11	1.56	0.17	4.67	5.85	U+ V-clay
1.85	63.02	0.81	23.42	0.84	0.20	0.20	0.21	7.26	Car
0.05	65.25	0.80	23.74	BDL	0.07	0.12	0.08	5.22	Car
0.95	63.13	0.81	22.70	0.34	0.05	0.33	0.06	5.95	Car
0.58	62.70	1.20	24.33	0.14	0.10	0.13	0.13	4.56	Car
0.65	64.82	1.05	24.61	0.23	0.02	0.09	0.09	3.89	Car
0.100	64.60	0.88	24.25	0.05	0.06	0.16	0.05	5.67	Car

Table 5: EMP partial analysis (in weight %) of principal elements forming uranium and vanadium minerals from SM-18 mine, Colorado

SiO_2	UO_3	CaO	V_2O_5	Al_2O_3	FeO	Na_2O	MgO	K_2O	Mineral
8.15	52.30	0.61	18.95	7.87	0.03	0.28	0.09	7.33	Car/V-clay
12.18	47.70	0.62	19.07	11.05	0.02	0.26	0.11	6.00	Car/V-clay
7.06	50.14	0.48	19.69	4.42	0.27	0.20	0.27	6.81	Car/V-clay
5.21	56.27	0.67	21.03	5.29	0.09	0.18	0.05	7.35	Car/V-clay
26.14	30.46	0.35	11.87	19.33	0.04	0.11	0.05	4.22	Car/V-clay
9.35	48.20	0.55	18.45	7.22	0.14	0.20	0.18	6.81	Car/V-clay

Table 6: EMP partial analysis (in weight %) of principal elements forming uranium and vanadium minerals from SM-18 mine, Colorado

SiO_2	UO_3	CaO	V_2O_5	Al_2O_3	Fe_2O_3	K_2O	Mineral
BDL	64.74	0.63	30.40	0.06	0.14	3.13	Car
BDL	65.08	0.10	30.00	0.12	0.15	3.95	Car
1.10	63.71	1.24	30.84	0.44	0.17	2.17	Car
0.53	60.59	1.32	28.73	0.26	0.04	4.45	Car
BDL	61.85	1.20	29.56	0.06	0.17	3.98	Car
BDL	61.72	1.35	29.43	0.12	0.15	3.85	Car
0.09	64.10	0.65	29.90	0.08	0.05	2.39	Car
0.03	63.59	0.42	30.94	0.21	0.11	1.87	Car

Table 7: EMP partial analysis (in weight %) of principal elements forming uranium and vanadium minerals from JD-9 mine, Colorado

SiO_2	UO_2	CaO	V_2O_5	Al_2O3	MgO	K_2O	Mineral
33.49	9.37	0.97	17.55	16.18	5.44	3.43	U+V-clay
46.27	2.13	0.60	14.77	16.57	2.46	1.58	U+V-clay
35.60	4.92	0.61	14.04	18.91	3.62	6.47	U+V-clay
36.67	3.84	0.79	17.19	15.76	5.81	4.16	U+V-clay
32.81	2.11	0.48	15.72	19.78	4.00	2.00	U+V-clay
43.64	5.63	1.33	24.31	9.07	1.49	4.43	U+V-clay

Table 8: EMP partial analysis (in weight %) of principal elements forming uranium and vanadium minerals from JD-9 mine

SiO_2	UO_2	CaO	V_2O_5	Al_2O_3	Mineral
17.10	46.22	2.02	10.28	5.17	Cof/V-clay
18.37	47.36	1.34	8.30	5.57	Cof/V-clay
15.03	51.65	1.89	9.13	4.16	Cof/V-clay
9.42	65.17	1.74	4.64	1.40	Cof
10.52	62.35	1.84	5.52	1.56	Cof

Table 9: EMP partial analysis (in weight %) of principal elements forming type 1 coffinite from the Three Crow deposit, Nebraska.

SiO_2	UO_2	CaO	V_2O_3	P_2O_5	Na_2O	K_2O
24.73	54.26	2.11	2.17	2.24	0.67	0.47
24.80	56.20	1.79	1.70	2.02	0.77	0.45
20.70	60.60	2.55	2.41	2.99	0.09	0.07
24.35	57.99	1.97	1.93	2.03	0.37	0.80
17.80	62.69	0.78	1.19	0.93	0.51	1.96

Table 10: EMP partial analysis (in weight %) of principal elements forming type 2 coffinite from the Three Crow deposit, Nebraska.

SiO_2	UO_2	CaO	V_2O_3	Al_2O_3	FeO	K_2O
14.66	62.32	2.36	2.11	1.48	1.44	0.67
11.92	60.40	2.08	1.89	0.86	1.43	1.08
13.67	63.39	1.54	2.14	1.70	1.34	1.99
24.52	50.21	1.89	1.10	0.38	0.41	0.72
20.86	56.48	0.94	0.70	0.19	0.32	1.25

APPENDIX D:

SECONDARY ION MASS SPECTROMETER (SIMS) ANALYSES

Table 1: SIMS U-Pb isotope data for total ores (Colorado deposits**)**

Samples	Mineral	Mineral	$^{206}Pb/^{238}$	**t (Ma)**	$^{207}Pb/^{235}$	t
4-15U-Cof-Mont-1	Coffinite	Type 1	0.0052	**33**	0.0393	39.
4-15U-Cof-Mont-2	Coffinite	Type 1	0.0037	**23**	0.0293	29.
4-15U-Cof-Mont-3	Coffinite	Type 1	0.0021	**13**	0.0186	19
4-15U-Cof-Mont-4	Coffinite	Type 1	0.0053	**33**	0.0490	49
4-13U-SM18-cryst-1	Carnotite	Type 2	0.0056	**36**	0.0788	77.
4-13U-SM18-cryst-2	Carnotite	Type 2	0.0054	**35**	0.0607	60
4-13U-SM18-cryst-3	Carnotite	Type 2	0.0079	**49**	0.0788	77
4-14U-CB10-U-py-1	Coffinite	Type3	0.0034	**21**	0.0375	37
4-13U-SM18-matrix	Carnotite	Type 4	0.0014	**9**	0.0155	16
4-13U-SM18--matrix	Carnotite	Type 4	0.0014	**9**	0.0145	15
4-14U-JD9-cement-1	Coffinite	Type 4	0.0004	**2**	0.0015	1
4-14U-JD9-cement-2	Coffinite	Type 4	0.0005	**3**	0.0011	1

Table 2: Activity ratios of uranium minerals (Colorado deposits)

Mineral Type	Sample	$(^{234}U/^{238}U)_A$	$(^{230}Th/^{238}U)_A$
Coff-Mont-1	4-15U-Coff-Mont-1	1.00	0.94
	4-15U-Coff-Mont-2	0.99	1.00
	4-15U-Coff-Mont-3	0.93	0.94
	4-15U-Coff-Mont-4	1.05	1.03
	4-15U-Coff-Mont-5	1.04	0.98
	4-15U-Coff-Mont-6	1.01	0.95
SM-18-Carnotite-2	4_13U_SM18_Cryst_1	1.04	0.89
	4_13U_SM18_Cryst_2	0.97	0.91
	4_13U_SM18_Cryst_3	1.08	0.84
	4_13U_SM18_Cryst_4	1.07	0.87
SM-18-Matrix-Car-4	4-13U-SM18-Matrix-1	1.04	0.29
	4-13U-SM18-Matrix-2	1.02	0.65
JD-9-Coffinite-4	4-14U-CB12-Cement-1	1.01	1.08
	4-14U-CB12-Cement-2	0.99	0.90

Table 3: SIMS sulphur isotopic data for sulphides from Colorado deposits

Sample:	**Mineral Type**	**$^{34}S/^{32}S_{meas}$**	**1σ (‰)**	**$\delta^{34}S$**	**ESD (‰)**
4-26-JD6-Cof-py-1	py/coff	4.28	0.3	-9.3	
4-26-JD6-Cof-py-2	py/coff	4.30	0.3	-5.0	
4-26-JD6-Cof-py-3	py/coff	4.27	0.3	-12.0	
4-26-JD6-Cof-py-4	py/coff	4.27	0.3	-13.3	
			Average:	**-9.9**	**3.7**
Cb11 gr1	subhedral	4.31	0.05	-23.1	
Cb11 gr2	subhedral	4.23	0.20	-41.6	
Cb11 gr3	subhedral	4.24	0.05	-38.9	
Cb11 gr4	subhedral	4.22	0.05	-43.8	
Cb11 gr5	subhedral	4.21	0.05	-46.4	
Cb11 gr7	subhedral	4.18	0.05	-51.7	
			Average:	**-40.9**	**9.8**
Cb12-3 gr8	framboidal	4.30	0.05	-26.3	
Cb12-3 gr8	framboidal	4.32	0.05	-20.7	
Cb12-3 gr8	framboidal	4.31	0.05	-25.0	
			Average:	**-24.0**	**2.9**
Cb12-2 gr9	framboidal	4.26	0.05	-34.9	
Cb12-2 gr9	framboidal	4.25	0.05	-35.9	
			Average:	**-35.4**	**0.7**

Table 4: U-Pb isotope data for total ores (Nebraska)

Mineral Type	Sample	$^{230}Th/^{234}U_A$	Fractionation	t (Ka)
Type 1 Coffinite	4-15U-M5A-COFF-1	0.1416	0.19	24
Type 1 Coffinite	4-15U-M5A-COFF-2	0.1651	0.22	28
Type 1 Coffinite	4-15U-M5A-COFF-3	0.1635	0.22	28
Type 1 Coffinite	4-15U-M5A-COFF-4	0.1551	0.21	26
Type 2 Coffinite	4-15-U-COFF-PY-1	0.7910	1.08	N/A
Type 2 Coffinite	4-15-U-COFF-PY-2	0.6107	0.83	194
Type 2 Coffinite	4-15-U-COFF-PY-3	0.6235	0.85	205

Table 5: U/Th Activity ratios for uranium minerals from the Three Crow deposit, Nebraska

Mineral Type	Sample	$(^{234}U/^{238}U)_A$	$(^{230}Th/^{238}U)_A$
Type 1 Coffinite	4-15U-M5A-COFF-1	1.56	0.22
Type 1 Coffinite	4-15U-M5A-COFF-2	1.74	0.29
Type 1 Coffinite	4-15U-M5A-COFF-3	1.64	0.27
Type 1 Coffinite	4-15U-M5A-COFF-4	1.56	0.24
Type 2 Coffinite	4-15-U-COFF-PY-1	1.23	0.99
Type 2 Coffinite	4-15-U-COFF-PY-2	0.98	0.60
Type 2 Coffinite	4-15-U-COFF-PY-3	1.45	0.90

Table 6: SIMS sulphur isotopic data for sulphide samples across the Three Crow roll-front deposit, Nebraska

Sample	Zone	Mineral type	$^{34}S/^{32}S_{meas}$	1σ (‰)	$\delta^{34}S$	ESD (‰)
5-10-T797	Distal altered	pyrite	4.16	0.3	-39.3	
5-10-T797	Distal altered	pyrite	4.10	0.3	-53.5	
5-10-T797	Distal altered	pyrite	4.10	0.3	-53.4	
5-10-T797	Distal altered	pyrite	4.09	0.3	-54.8	
5-10-T797	Distal altered	pyrite	4.10	0.3	-53.0	
5-10-T797	Distal altered	pyrite	4.18	0.3	-35.3	
5-10-T797	Distal altered	pyrite	4.17	0.3	-35.4	
5-10-T797	Distal altered	pyrite	4.18	0.3	-35.2	
5-10-T797	Distal altered	pyrite	4.09	0.3	-54.4	
5-10-T797	Distal altered	pyrite	4.09	0.3	-54.8	
				Average	**-46.9**	**9.2**
5-9-H150C	proximal altered	pyrite	4.27	0.4	-12.8	
5-9-H150C	proximal altered	pyrite	4.29	0.3	-8.8	
5-9-H150C	proximal altered	pyrite	4.19	0.3	-31.7	
5-9-H150C	proximal altered	pyrite	4.25	0.3	-17.5	
5-9-H150C	proximal altered	pyrite	4.15	0.3	-39.9	
5-9-H150C	proximal altered	pyrite	4.24	0.3	-20.2	
5-9-H150C	proximal altered	pyrite	4.22	0.3	-24.8	
5-9-H150C	proximal altered	pyrite	4.17	0.3	-36.6	
5-9-H150C	proximal altered	pyrite	4.15	0.3	-39.2	
5-9-H150C	proximal altered	pyrite	4.20	0.3	-28.6	
5-9-H150C	proximal altered	pyrite	4.21	0.3	-26.6	
5-9-H150C	proximal altered	pyrite	4.27	0.3	-12.9	
5-9-H150C	proximal altered	pyrite	4.11	0.3	-49.3	
5-9-H150C	proximal altered	pyrite	4.27	0.3	-12.5	
5-9-H150C	proximal altered	pyrite	4.24	0.3	-18.3	
5-9-H150C	proximal altered	pyrite	4.12	0.3	-47.3	
				Average	**-26.7**	**12.9**
4-26-M5A-	mineralized	py/coff	4.26	0.3	-16.0	
4-26-M5A-	mineralized	py/coff	4.22	0.3	-23.6	
4-26-M5A-	mineralized	py/coff	4.22	0.3	-25.2	
4-26-M5A-	mineralized	py/coff	4.18	0.3	-34.3	
4-26-M5A-	mineralized	py/coff	4.16	0.3	-38.0	
4-26-M5A-	mineralized	py/coff	4.14	0.3	-43.2	
4-26-M5A-	mineralized	py/coff	4.14	0.3	-42.9	
				Average	**-31.9**	**10.5**
5-9-H161C	mineralized	pyrite	4.09	0.3	-54.9	
5-9-H161C	mineralized	pyrite	4.09	0.3	-54.1	

5-9-H161C	mineralized	pyrite	4.09	0.3	-54.5	
5-9-H161C	mineralized	pyrite	4.09	0.3	-54.2	
5-9-H161C	mineralized	pyrite	4.09	0.4	-55.0	
5-9-H161C	mineralized	pyrite	4.08	0.3	-55.5	
5-9-H161C	mineralized	pyrite	4.09	0.3	-54.2	
5-9-H161C	mineralized	pyrite	4.09	0.3	-54.1	
5-9-H161C	mineralized	pyrite	4.09	0.3	-53.9	
5-9-H161C	mineralized	pyrite	4.10	0.4	-52.9	
5-9-H161C	mineralized	pyrite	4.09	0.3	-53.4	
				Average	**-54.2**	**0.6**
5-9-T292C	Proximal reduced	pyrite	4.09	0.3	-54.8	
5-9-T292C	Proximal reduced	pyrite	4.09	0.3	-54.8	
5-9-T292C	Proximal reduced	pyrite	4.07	0.3	-58.6	
5-9-T292C	Proximal reduced	pyrite	4.21	0.3	-27.1	
5-9-T292C	Proximal reduced	pyrite	4.14	0.2	-42.1	
5-9-T292C	Proximal reduced	pyrite	4.08	0.2	-57.6	
5-9-T292C	Proximal reduced	pyrite	4.07	0.2	-58.6	
5-9-T292C	Proximal reduced	pyrite	4.14	0.2	-42.7	
5-9-T292C	Proximal reduced	pyrite	4.07	0.2	-57.9	
5-9-T292C	Proximal reduced	pyrite	4.06	0.3	-62.1	
5-9-T292C	Proximal reduced	pyrite	4.07	0.2	-58.1	
				Average	**-52.0**	**11.1**
5-10-T810C	Distal reduced	marcasite	4.15	0.3	-40.8	
5-10-T810C	Distal reduced	marcasite	4.16	0.3	-39.9	
5-10-T810C	Distal reduced	marcasite	4.17	0.3	-35.7	
5-10-T810C	Distal reduced	marcasite	4.13	0.3	-45.0	
				Average	**-40.3**	**3.8**
5-10-T810C	Distal reduced	pyrite	4.27	0.3	-12.9	
5-10-T810C	Distal reduced	pyrite	4.25	0.3	-17.4	
5-10-T810C	Distal reduced	pyrite	4.21	0.3	-27.6	
5-10-T810C	Distal reduced	pyrite	4.25	0.3	-17.9	
5-10-T810C	Distal reduced	pyrite	4.22	0.3	-25.2	
				Average	**-20.2**	**6.0**